University of Trento
Department of Physics

Doctoral Thesis

QUANTIZED VORTICES AND SOUND VELOCITIES IN DIPOLAR SUPERSOLIDS

Marija Šindik

Supervisors
Dr. Alessio Recati
Prof. Gabriele Ferrari

April 2025

Supervisors:	Dr. Alessio Recati, University of Trento
	Prof. Gabriele Ferrari, University of Trento
Referees:	Prof. Stephanie Reimann, Lund University
	Prof. Giovanni Modugno, University of Florence
	Prof. Stefano Giorgini, University of Trento

Contents

Abstract

Supersolids are an intriguing phase of matter that simultaneously exhibit crystalline order and superfluidity. They have recently been realized experimentally in dipolar Bose-Einstein condensates. This thesis investigates two fundamental features of dipolar supersolids: quantized vortices and the propagation of sound modes.

Although quantized vortices constitute a key probe of superfluidity, their observability in dipolar supersolids is largely inhibited by the strong density depletion caused by droplet formation. We propose a protocol for vortex nucleation and detection, based on a ramp of the s-wave scattering length across the superfluid-supersolid phase transition. Starting from a slowly rotating, vortex-free configuration in the superfluid phase, a vortex is nucleated as the system enters the supersolid phase, due to the strong reduction of the critical angular velocity. Once created, the vortex is robustly preserved as the condensate is brought back into the superfluid phase, where it can be readily observed. This protocol was recently implemented in experiments, confirming its feasibility.

The second part explores sound propagation in a dipolar supersolid confined in a tubular potential with periodic boundary conditions, corresponding to a ring geometry. We propose a method for exciting Goldstone modes, arising from the spontaneous breaking of phase and translational symmetries. By abruptly removing a weak periodic perturbation, the resulting oscillations are studied by numerically solving the extended Gross-Pitaevskii equation. The values of the two longitudinal sound velocities exhibited in the supersolid phase are then analyzed using the hydrodynamic theory of supersolids at zero temperature. This approach allows for the determination of key hydrodynamic parameters, such as the layer compressibility modulus and the superfluid fraction, the latter found to be consistent with the Leggett upper bound.

1

Introduction

Supersolid is a novel and exotic phase of matter that simultaneously exhibits both the superfluid and crystalline properties, arising from the spontaneous breaking of both phase and translational symmetry. The first notion of such state comes from the theoretical predictions of Gross in 1957 [1, 2], followed by a series of papers by Yang [3], Andreev and Lifshitz [4], as well as Thouless [5], Chester [6] and Leggett [7], proposing various theoretical scenarios for its possible existence. It is also important to note the work of Penrose and Onsager [8], who argued that the localization of particles characterizing a crystalline phase is inherently incompatible with the delocalization required for condensation, making the supersolid state impossible.

The search for the supersolid state attracted the attention of both theoretical and experimental physicists across various fields, due to its counterintuitive nature. Despite their efforts, conclusive detection was lacking for decades [9]. Finally, an important discovery came from the ultracold atom community in 2017, with the first experimental observation of supersolid properties in Bose-Einstein condensates with spin-orbit-coupling [10] and inside optical resonators [11]. This was followed in 2019 by three independent groups reporting the observation of supersolid properties in dipolar ultracold gases [12–14].

These discoveries opened an exciting new platform for research. In recent years, supersolids have become one of the most actively studied topics in the field of ultracold atoms (see the recent perspective [15] and references therein). The study of supersolidity has also extended to other systems, such as neutron stars [16, 17]. While the practical applications of supersolids are still under exploration, their unique features offer new possibilities in fields such as quantum simulation, quantum sensing, and atomtronics [18, 19].

1.1. What is a supersolid

The concept of a supersolid seems paradoxical, as it combines characteristics of two fundamentally different phases of matter – the frictionless flow of a superfluid and the rigid crystalline structure of a solid. This unique state emerges due to interactions that, under specific conditions, enable the coexistence of these seemingly incompatible properties (see, for example, [9]).

In a solid, atoms or molecules are localized, maintaining fixed relative positions with only vibrational motion. This results in structural rigidity and resistance to shear. In crystalline solids, these particles are additionally arranged in an ordered pattern, each occupying a specific site within a three-dimensional periodic lattice. This arrangement breaks continuous translational symmetry in favor of discrete one, leading to density long-range order (LRO). It's important to note that this symmetry breaking occurs spontaneously due to particle interactions, rather than being externally imposed.

Superfluidity is a macroscopic quantum phenomenon in which a fluid exhibits zero viscosity, sustaining frictionless, dissipationless flow. It was first observed in 1938 in liquid ^{4}He when cooled below the so-called lambda point (2.17K) [20, 21]. Superfluidity is strongly related to Bose-Einstein condensation – a many-body quantum effect that is characterized by a macroscopic occupation of the single-particle ground state (the condensate state) [22, 23]. Bose-Einstein condensation occurs when a system of identical particles following Bose statistic[1]is cooled below a critical temperature. At this point, a finite fraction of particles occupy a condensate state that can be fully described by a classical field $\Psi(\mathbf{r})$, rather than by a quantum field operator. The phase of the condensate wavefunction is spontaneously chosen during the phase transition, thereby spontaneously breaking gauge symmetry. The condensate particles are localized in momentum space but delocalized in position space, resulting in coherence effects that extend over large distances, a property known as off-diagonal long-range order (ODLRO).

A supersolid can thus be defined as a quantum state of matter resulting from the simultaneous and spontaneous breaking of both gauge and translational symmetries, exhibiting both diagonal and off-diagonal long-range order [9]. The term "spontaneous" is important to distinguish supersolids from phases where density modulation is externally imposed. For example, this can be accomplished by adsorbing layers of superfluid ^{4}He on a periodic substrate, or by trapping a BEC in

[1]In a system of identical particles obeying Fermi statistics, Bose-Einstein condensation can occur through the formation of Cooper pairs – composite entities consisting of two fermions that effectively behave as bosons, and as such can undergo BEC.

an external periodic potential. In these cases, since translational symmetry is not spontaneously broken, they cannot be considered true supersolids.

1.2. Supersolidity in ^{4}He

Early approaches to supersolidity focused on whether a crystal of a substance that exhibits superfluidity (i.e., composed of bosonic particles) could incorporate a superfluid phase, allowing them to merge and coexist as a unified supersolid state (see reviews [9, 24], and references therein). One theoretical scenario considered a quantum crystal with point defects, such as vacancies or interstitials, which are typically thermally activated but could possibly also exist in the ground state at zero temperature (which is not an obvious assumption) [4]. These point defects can move through the system; for example, a vacancy can exchange position with neighboring atoms through quantum tunneling (see Fig. 1.1(a)). Therefore, they can be considered as a gas of quantum particles with negative mass that obey Bose statistics, and as such, can undergo Bose-Einstein condensation and become superfluid at low temperatures. The delocalized, coherently coupled gas of point defects can then enable the exchange of crystal atoms at distant sites, allowing for frictionless mass flow to coexist with crystal properties.

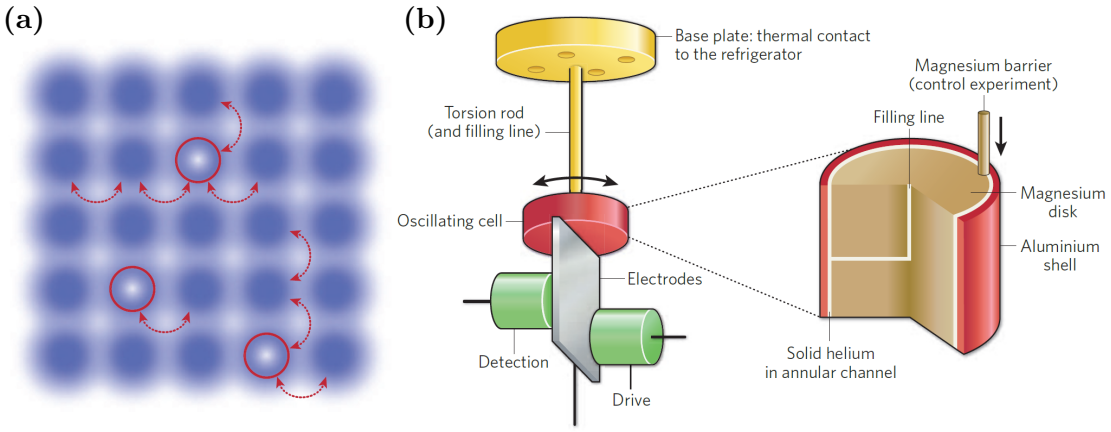

FIG. 1.1.: (a) A crystal lattice with vacancies (empty sites circled in red), which can exchange positions with neighboring atoms (blue dots). (b) Schematic representation of the torsional oscillator experiment by Kim and Chan. The oscillating cell, attached to a torsional rod, contains an annular channel filled with helium. A vertical barrier can be inserted to block the superfluid flow. Adapted from [24].

A crystal of ^{4}He has long been considered the most promising candidate for exhibiting supersolidity. After years of unsuccessful experimental attempts, the first indication of supersolidity appeared in 2004 in a torsional oscillator experiment by Kim and Chan [25, 26]. They followed Leggett's proposal [7], which involved measuring a reduction in the moment of inertia of a sample relative to its classical value, an effect known as non-classical rotational inertia (NCRI). This phenomenon arises from the unique behavior of superfluids under rotation. Unlike ordinary fluids, a superfluid remains at rest when set into slow rotation. It only exhibits rotating motion once the rotation speed exceeds a certain critical value, through the introduction of quantized vortices (more about quantized vortices in Chapter 5).

The experimental setup consisted of a cylindrical container with an annular space filled with solid helium, suspended from a torsion rod, allowing for small oscillations around its axis, as illustrated in Fig 1.1(b). The authors observed an abrupt drop in the oscillation period below 200mK, which decreased monotonically with further temperature reduction. This period drop was interpreted as evidence of NCRI, that is, a reduction in the moment of inertia due to the decoupling of superfluid mass within the rotating solid helium. Several research groups replicated the experiment by Kim and Chan, consistently confirming the period drop, although with varying magnitudes. Control experiments with a cell filled with solid ^{3}He (a fermion) showed no such period drop. Similarly, no period drop was observed when a barrier was inserted in the annulus containing the sample, blocking the macroscopic mass flow. These results were interpreted as a strong indication of supersolidity in ^{4}He.

However, in subsequent years, there have been several indications that the observed period drop may not necessarily involve a supersolid phase transition [9]. Theoretical Monte Carlo simulations showed that vacancies in the ground state of a perfect ^{4}He crystal are energetically unfavorable, making the description based on highly mobile vacancies unlikely as the mechanism of supersolidity. This raised the question of whether supersolidity is an inherent property of ^{4}He crystals, or if it arises solely due to defects in the samples, such as dislocation cores and grain boundaries.

Experimentally, it was found that the shear modulus of bulk solid ^{4}He increases at the same temperature as the observed period drop. Furthermore, the temperature dependence of the shear modulus resembled that of NCRI, including the same transition temperature dependence on ^{3}He impurity concentration. This unusual correlation suggested that the stiffening of the torsional oscillator might be responsible for the observed period drop. In contrast, solid ^{3}He, with its bcc

crystal structure (unlike the hcp structure of ^{4}He), does not exhibit shear modulus stiffening at low temperatures, which would explain why no period drop was observed in solid ^{3}He samples. In light of these findings, Kim and Chan repeated their experiment in 2012 using a redesigned setup that is free from any bulk solid shear modulus stiffening effect. In this case, no measurable period drop was found, leading them to retract their earlier claim of supersolidity in solid helium [27].

At present, there is no definitive understanding of whether ^{4}He crystals exhibit supersolidity, despite numerous theoretical proposals and extensive experimental efforts. Nevertheless, Kim and Chan's experiment has reignited interest in the phenomenon, extending the search beyond solid helium to other systems, with notable success in the field of cold atom physics.

1.3. Supersolidity in ultracold atomic gasses

A new experimental research platform emerged in 1995 with the groundbreaking realization of Bose-Einstein condensation [28, 29]. In the nearly 30 years since, numerous experimental advances and techniques have been developed, allowing for a remarkable level of control over these systems. In particular, atoms with diverse properties can be cooled to form a Bose-Einstein condensate, external trapping potentials can be manipulated to create configurations like optical lattices, and interparticle interactions can be tuned with remarkable precision [30–32]. This makes ultracold gases an incredibly versatile and controllable platform, ideal for investigating a wide range of quantum phenomena, novel phases of matter, and fundamental questions in many-body and condensed matter physics.

1.3.1. Soft-core interaction

The first idea about supersolidity in ultracold gases originated from Gross in 1957 (though he didn't use that term), who showed that a system of bosons described by a classical wave field, can exhibit a spatially periodic density in the ground state for a suitable attractive two-body potential [1, 2]. This idea remained largely unexplored until Pomeau and Rica revisited it in 1994 [33, 34]. They studied a Gross-Pitaevskii model with a soft-core interaction potential, which takes a positive constant value within a certain particle distance, and zero otherwise. For sufficiently high density, the system undergoes a phase transition to a periodically modulated ground state. This state can be described by a real wave function, meaning the system retains a uniform phase. Additionally, they demonstrated the

existence of quantized vortices in this phase, confirming that the system remains superfluid while simultaneously exhibiting spontaneous density modulation.

A possible approach to realizing soft-core interactions in a physical system involves the use of Rydberg atoms [35, 36]. These are atoms of typically alkali metals, with one or more electrons in highly excited electronic states. As a result, they exhibit exceptionally large electric dipole moments. The strong dipole-dipole interaction between Rydberg atoms gives rise to the Rydberg blockade, a mechanism that prevents multiple atoms from being simultaneously excited to Rydberg states within a certain distance. This creates a distinctive interaction potential: it flattens below a specific cutoff distance while exhibiting long-range dipolar repulsion. Numerical simulations suggest that by carefully tuning the interparticle potential using external fields, it is possible to form a supersolid state. However, experimental realization of such systems is still lacking.

Although the soft-core interaction is not particularly realistic in physical systems, it enabled the numerical study of both the static and dynamic properties of the first supersolid models in ultracold gases. Importantly, as Pomeau and Rica accurately predicted, the key factor in achieving the supersolid phase is the presence of a roton minimum in the excitation spectrum, rather than the specific form of the interaction potential.

It is important to note the paradigm shift here: instead of inducing superfluidity in a solid system, this approach focuses on inducing crystalline properties in a superfluid system. This alternative approach has achieved much greater success in experimental observation. Unlike a helium crystal, where each unit cell contains a single atom, a crystal in an ultracold gas system is non-commensurate. A large fraction of particles comprises a single lattice cell, forming a cluster. That is why this phenomenon is often referred to as *cluster supersolidity*.

The possibility of observing supersolid behavior in ultracold atomic gases has attracted a lot of attention, extending this idea to a wide variety of systems. Experimental evidence of supersolidity has so far been demonstrated in several platforms, including cold atomic systems with spin-orbit coupling, light-mediated interactions in optical cavities, and gases with strong magnetic dipole-dipole interactions.

1.3.2. Spin-orbit coupled Bose-Einstein condensates

One of the first experimental platforms to provide evidence of supersolidity was the spin-orbit coupled Bose-Einstein condensate (BEC). In these systems, spin-orbit interaction (an interaction between a particle's spin and its momentum) is induced using a two-photon Raman transition between two atomic spin states, a

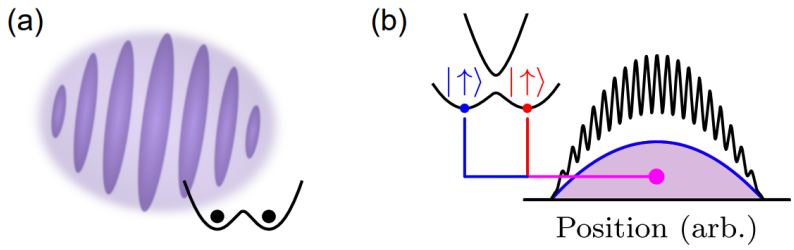

FIG. 1.2.: Supersolid stripe phase of a spin-orbit-coupled BEC. (a) Density profile illustration, adapted from [40]. (b) Spatial density distribution, where the two spin states are shown in red ($|\uparrow\rangle$) and blue ($|\downarrow\rangle$), while the total density is in black. Adapted from [41]. Both figures illustrate a dispersion relation with two equally populated minima.

method first established in the group of Spielman [37]. For small Raman coupling strengths, this interaction creates an atom-photon-dressed state with a dispersion relation featuring two degenerate minima at finite momenta. These minima correspond to two non-orthogonal dressed spin states with opposite momenta (k and $-k$). The interference between these two components in the Bose-Einstein condensate produces a periodic density modulation, forming the stripe phase [38, 39], as illustrated in Fig. 1.2.

The stripe phase exhibits features of both superfluidity and crystalline order - the two characteristics of supersolids. The relative phase between the two BEC components determines the position of the stripes. Since this phase is a continuous variable, the stripe phase spontaneously breaks continuous translational symmetry while preserving superfluidity. The excitation spectrum in the stripe phase is predicted to exhibit two gapless branches, corresponding to two spontaneously broken symmetries [42]. These Goldstone modes can be investigated by exciting the collective modes of the system [43, 44] (see also the review [45]). The spin Goldstone mode has been linked to the crystal dynamics of the stripes, demonstrating its lattice-phonon nature and the non-rigidity of the stripes[2] [46].

The first experimental observation of the supersolid properties of the stripe phase was reported by the group of Ketterle in 2017 [10]. They observed the predicted density modulation using Bragg spectroscopy, while a sharp momentum distribution confirmed the superfluid nature of the state. Recently, the stripe phase has also been imaged in situ, using matterwave lensing techniques [40]. Further experimental studies have demonstrated long-range coherence between the spin components in the stripe phase [41]. Very recently, a stripe compression mode was

[2]Initially it was believed that the stripe pattern is rigid, as the coupling is induced by Raman laser beams, and thus externally imposed.

observed, which softens as the spin-orbit coupling strength increases, marking the supersolid phase transition point [40].

1.3.3. Supersolidity in optical cavities

When a Bose-Einstein condensate is placed inside an optical cavity and transversely pumped with a laser, it undergoes a phase transition to the superradiant phase above a critical laser intensity. This phase is marked by the self-organization of atoms into a checkerboard pattern, coherently scattering photons into the cavity mode [47, 48]. The atoms can occupy either the even or odd sites of the checkerboard pattern, leading to the spontaneous breaking of parity ($\mathbb{Z}_2$) symmetry. Despite the resulting periodic density modulation and global phase coherence of the BEC, this system cannot be considered a true supersolid and is instead referred to as a *lattice supersolid*. This is because translational symmetry is explicitly broken by the underlying optical lattice, and only a discrete spatial symmetry is spontaneously broken (in addition to the phase symmetry of the BEC).

However, continuous translational symmetry breaking can be achieved by symmetrically coupling a BEC to the modes of two optical cavities (see Fig. 1.3(a)), as first realized by the group of Esslinger in 2017 [11]. Each BEC-cavity system individually exhibits parity symmetry, with photons scattered by the atoms coherently populating the two cavities. If the coupling strengths of both cavities to the BEC

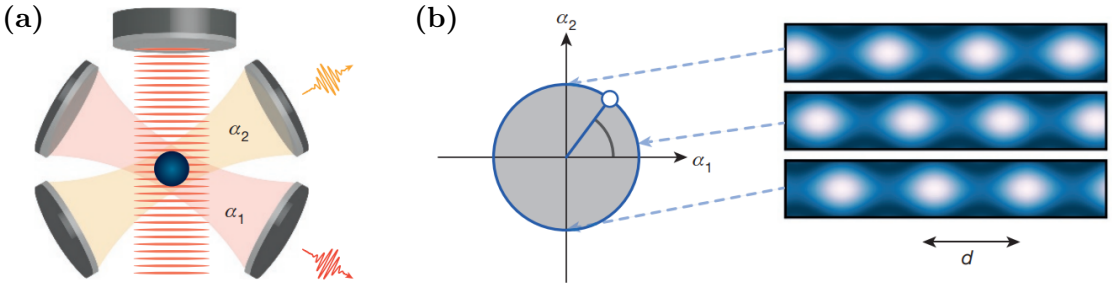

FIG. 1.3.: Supersolidity in a BEC coupled to two optical cavities. (a) Schematic representation of the experimental setup. A BEC (blue cloud) is trapped at the intersection of two optical cavities crossing at a 60°angle, and is transversely pumped with a back-reflected laser beam, forming a one-dimensional optical lattice (red stripes). The laser frequency is detuned from the atomic transition but close to the cavity resonance. The atoms scatter photons into the two cavities, generating coherent field amplitudes α_1 and α_2. (b) Changing the angle in the $\alpha_1 - \alpha_2$ plane, that is, shifting the two cavity field strengths corresponds to a continuous shift of the periodic density pattern. Adapted from [11].

are equal, there is no energy cost of moving photons from one cavity to the other. As a result, the relative field amplitudes in the two cavities can vary continuously (see Fig. 1.3(b)), reflecting the continuous U(1) symmetry emerging from the so-called *symmetry enhancement*. This shifting of the fields' intensity corresponds to a continuous shift of the interference pattern, marking the spontaneous breaking of translational symmetry and the realization of the supersolid state. The associated zero-energy Goldstone mode of this phase has been observed using Bragg spectroscopy on the pump and cavity fields [49]. However, the supersolid lattice in this system is incompressible and therefore lacks the crystal Goldstone mode.

Recently, phonon modes of a supersolid lattice were observed in a BEC coupled to a confocal optical resonator [50]. In this system, a U(1) symmetry is generated using a transverse double-pumping scheme in a multimode cavity. The authors observed a phonon dispersion relation with a sound speed dependent on the atom-photon coupling strength. Supersolidity has also been realized in BECs coupled to a ring-cavity, with longitudinal pumping by two non-interfering, counterpropagating modes of equal strength [51]. Here, a continuous translational symmetry emerges from the phase difference between forward- and backward-traveling waves. For a more comprehensive review of quantum-gas cavity QED systems, see Ref. [52].

1.3.4. Dipolar supersolids

Dipolar Bose-Einstein condensates have emerged as one of the most extensively studied platforms for supersolidity in ultracold gases. Over recent years, significant progress has been made, both in theoretical predictions and experimental realizations [15, 53–55]. These systems, composed of atoms with significant magnetic dipole moments, exhibit unique properties due to the long-range and anisotropic nature of dipolar interactions. Supersolidity in dipolar BECs emerges from two key factors: the softening of the roton mode, and the interplay between attractive mean-field interactions and the effective repulsion induced by quantum fluctuations. The details of these mechanisms will be discussed in Chapter 2.

While the groundwork for the discovery of supersolidity in dipolar condensates has been laid over for two decades, an essential theoretical work came in 2019 from Roccuzzo and Ancilotto [56]. Their numerical study in extended tubular geometry demonstrated that supersolid properties – such as non-classical rotational inertia and the emergence of two gapless modes associated with the spontaneous breaking of symmetries – exist within a narrow region of parameter space.

Experimental realization quickly followed these theoretical predictions. In 2019, three research groups independently reported the first observations of supersolid-

ity in dipolar BECs: first by the group of Modugno in Pisa [12], followed shortly after by the group of Pfau in Stuttgart [13], and finally by the group of Ferlaino in Innsbruck [14]. These experiments demonstrated the coexistence of spontaneous density modulations and global phase coherence in elongated (cigar-shaped) harmonic traps. Notably, this phase coherence is restored after a dephasing interaction quench, indicating that particle flow across a dipolar supersolid maintains its superfluidity [57].

The resulting supersolid state can be described as a structure of atomic clusters, or droplets, arranged in a lattice and connected by weak density links, as shown in Fig. 1.4. As previously mentioned, this form of supersolidity is characterized by each lattice site containing a large number of particles. The density links provide finite coupling between the clusters, ensuring global phase coherence throughout the supersolid. It is important to note that the lattice structure in these systems is not externally imposed, but emerges entirely as a result of interatomic interactions.

Following the initial realizations, experimental and theoretical efforts focused on identifying additional signatures of supersolidity. In particular, they studied the collective elementary excitations associated with spontaneous symmetry breaking, known as the Goldstone modes [59–61]. Longitudinal compression of an elongated, harmonically trapped gas excites its characteristic breathing mode. In the superfluid phase, the motion of the cloud is characterized by a single frequency. In contrast, the supersolid phase revealed two distinct frequencies: one dominated by relative motion between the droplets, and the other corresponding to amplitude oscillations without a shift in the droplet positions.

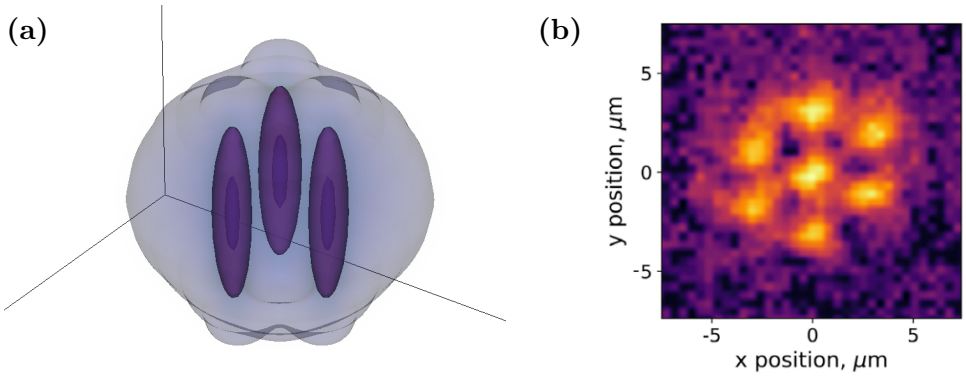

FIG. 1.4.: (a) Illustration of the density profile for a trapped dipolar supersolid in a two-dimensional configuration. (b) In situ image of the density profile from the experiment in Ref. [58].

Another unique feature of supersolidity lies in its rotational properties. Following Leggett's proposal regarding non-classical rotational inertia, numerical studies have demonstrated a reduced moment of inertia in two-dimensional supersolid configurations, confirming their partial superfluid character [62]. In elongated configurations, these effects are best probed through the scissors mode – a collective oscillation induced by a sudden rotation of an anisotropic trapping potential. This method was initially employed to demonstrate superfluidity in ordinary (non-dipolar) Bose-Einstein condensates shortly after their discovery [63, 64]. Scissors mode experiments on dipolar gases confirmed the reduced moment of inertia in the supersolid phase [65]. However, in systems with two-dimensional structures, the scissors mode frequency is not directly linked to the moment of inertia due to the presence of additional rotational oscillations of the droplets [66], making it a less robust probe in such configurations [67].

While most early studies focused on one-dimensional supersolid configurations of droplet arrays in elongated traps, recent experiments have successfully realized two-dimensional supersolid structures in pancake-shaped traps [58, 68]. This opened new avenues for investigating rotational properties, the role of dimensionality, and in particular vortex dynamics in dipolar supersolid systems.

Dipolar Bose-Einstein condensates have emerged as an exceptional platform for studying supersolidity, owing to their intrinsic long-range interactions and the ability to precisely tune and control these systems. Building upon these significant advances, this thesis aims to further deepen our understanding of the fundamental properties of dipolar supersolids.

2

Dipolar Bose-Einstein condensates

Dipolar Bose-Einstein condensate consists of bosonic particles (atoms or molecules) that possess significant magnetic or electric dipole moments. These dipole moments give rise to long-range, anisotropic dipole-dipole interactions in addition to the short-range contact interactions arising from particle scattering. The interplay of these interactions results in a wide variety of new physical phenomena, among which is the supersolid state as the central focus of this thesis.

The first dipolar Bose-Einstein condensate was realized in 2005 with magnetic atoms, specifically using chromium (Cr) atoms with a magnetic moment of 6 Bohr magnetons (μ_B) [69]. This was followed by the condensation of lanthanides, including dysprosium (Dy), which has the largest known magnetic moment of $10\mu_B$ [70], and erbium (Er) with $7\mu_B$ [71]. The large permanent magnetic dipole moments in these atoms originate from their electronic ground-state configurations characterized by large total angular momentum[1], which also results in a rich electronic transition spectrum [53].

An additional advantage of these highly magnetic atoms is the existence of several naturally abundant isotopes that exhibit diverse properties, including both bosonic and fermionic statistics, as well as distinct scattering properties and Feshbach resonance spectrum [53]. Supersolid states have been observed in ^{166}Er, ^{162}Dy, and ^{164}Dy. Trapping and cooling of these atoms have been achieved using Zeeman slowers, magneto-optical traps, and optical dipole traps [53, 72]. Remarkably, the efficiency of these techniques for lanthanides is comparable to that of alkali metals, which were used in early experiments on BECs.

In addition to magnetic systems, dipole-dipole interactions can also arise from electric dipole moments, such as in heteronuclear molecules [73] and Rydberg

[1]The total angular momentum is a combination of electronic orbital angular momentum, electronic spin, and, to a lesser extent, nuclear spin.

atoms [74]. These systems can possess electric dipole moments corresponding to dipolar interaction strengths that are significantly (an order of magnitude) larger than those of magnetic atoms [55]. This makes them highly attractive for exploring the effects of strong dipolar interactions. However, their experimental realization faces several challenges, such as short lifetimes and rapid dissipation, which limit the creation of dense, ultracold samples. Recently, a quantum degenerate gas of the fermionic polar molecule potassium-rubidium (KRb) has been achieved [75, 76], though the realization of a BEC in such systems is still lacking.

Due to these limitations, most studies of dipolar quantum phenomena have focused on magnetic atoms, including the research presented in this thesis. This chapter outlines the main properties of magnetic dipolar BECs[2], with a particular focus on the mechanism underlying the emergence of the supersolid state, precursor phenomena, and the parameter regimes in which it exists.

2.1. Interactions

We consider a dilute system of dipolar bosonic particles at zero temperature. A gas is considered dilute if the range of interparticle forces b is significantly smaller than the average distance between particles, which can be expressed as $nb^3 \ll 1$, where n is the gas density [22, 23]. This is commonly referred to as the diluteness condition. In this regime, two-body interactions dominate, while higher-order interactions involving three or more particles can be safely neglected. The diluteness condition also ensures the metastability of the gaseous phase, as three-body recombination processes, which would otherwise drive the system towards the solid ground state, are negligible.

The two-body interactions in this system consist of a contact interaction, which describes particle scattering, and a dipole-dipole interaction, arising from the particles' magnetic moments. The interplay between these two very distinct interactions gives rise to novel quantum phases, such as supersolids.

2.1.1. Contact interaction

In the ultracold dilute regime, particle scattering is well-approximated by the low-energy limit, where the scattering amplitude becomes independent on both energy and scattering angle [22, 23]. In this regime, the collisions are fully characterized

[2]Many of these principles can be translated to electric dipolar systems, with appropriate adjustments to the dipolar coupling constant, but we avoid further discussion of these systems.

by a single parameter: the s-wave scattering length. The macroscopic properties of the system are thus independent of the details of the interatomic potential at short distances. It is therefore convenient to replace it with the mathematically simpler contact interaction pseudopotential of the form

$$V(\mathbf{r}) = g\delta(\mathbf{r}), \tag{2.1}$$

where g is the contact interaction strength, and δ denotes the Dirac delta function. This effective interaction is zero-range and isotropic. For the replacement to be valid, it must reproduce the same value of the s-wave scattering length a of the microscopic potential. In the lowest-order Born approximation, this leads to the relation

$$g = \frac{4\pi\hbar^2}{m}a, \tag{2.2}$$

where m is the atomic mass and $\hbar$ is the reduced Planck constant.

The s-wave scattering length can be either positive or negative, corresponding to repulsive or attractive interactions, respectively. Its value can be controlled using external fields. The most commonly used approach relies on the existence of Feshbach resonances: by varying the strength of an externally applied magnetic field, the scattering length can be finely tuned over a wide range of values, enabling precise control of the interatomic interactions [32].

A uniform BEC is stable only for repulsive interatomic forces ($a > 0$) [22, 77]. In the presence of external trapping, however, stability can also be maintained for sufficiently small attractive interactions ($a < 0$), where the collapse of the cloud is counteracted by the zero-point kinetic energy (quantum pressure) [78]. This balance is achieved only if the number of particles remains below a critical value. In all the systems considered in this thesis, a repulsive contact interaction is assumed, which is also the case in most experimental setups.

2.1.2. Dipole-dipole interaction

The dipolar interaction potential between two identical magnetic dipoles separated by a distance r and aligned along the same direction is given by the following form [53]

$$V_{\mathrm{dd}}(\mathbf{r}) = \frac{\mu_0\mu^2}{4\pi}\frac{1-3\cos^2\theta}{r^3}. \tag{2.3}$$

Here, μ_0 is the magnetic vacuum permeability, μ is the magnetic dipole moment of the particles, and θ is the angle between the relative position vector $\mathbf{r}$ and the polarization direction, as illustrated in Fig. 2.1(a). This interaction is long-ranged,

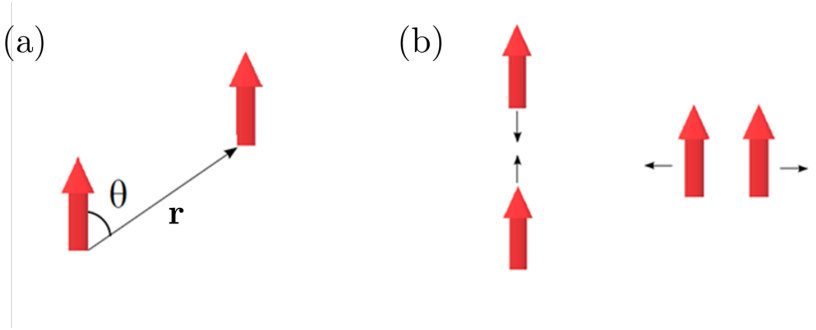

FIG. 2.1.: (a) Illustration of the relevant parameters in the dipole-dipole interaction. The arrows represent two identical dipoles oriented along the z-axis. The interaction depends on their separation distance r and the angle θ between the relative position vector $\mathbf{r}$ and the polarization direction. (b) The two aligned dipoles attract in a head-to-tail configuration, while they repel in a side-by-side configuration.

decaying as r^{-3}, in contrast to the typical interatomic van der Waals potential, which decays as r^{-6} at large distances.

The dipole-dipole interaction (DDI) is anisotropic, it strongly depends on the relative orientation of two dipoles. The potential vanishes at an angle $\theta_0 = \arccos(1/\sqrt{3}) = 54.7°$. For $\theta < \theta_0$, corresponding to a head-to-tail configuration of the dipoles (see Fig. 2.1(b)), the interaction is attractive, whereas for $\theta > \theta_0$, corresponding to side-to-side configurations, the interaction becomes repulsive. Due to the energetically favorable head-to-tail alignment, a gas of ultracold dipolar particles becomes elongated along the polarization direction, rather than precisely conforming to the geometry of the confining potential. This effect is known as magnetostriction [53].

The strength of the dipolar interaction is commonly quantified using the dipolar length, defined as

$$a_{\mathrm{dd}} = \frac{\mu_0 \mu^2 m}{12\pi\hbar^2}. \tag{2.4}$$

To compare the strength of the dipolar interaction with the contact interaction, a dimensionless parameter is introduced:

$$\epsilon_{\mathrm{dd}} = \frac{a_{\mathrm{dd}}}{a} = \frac{\mu_0 \mu^2}{3g}. \tag{2.5}$$

While the contact interaction strength can be varied using Feshbach resonances, the strength of the dipole-dipole interaction is usually inherently fixed by the

magnetic dipole moment of the atom[3]. Therefore, the value of ϵ_{dd} is tuned by manipulating the scattering length.

A uniform system of polarized particles interacting solely through dipolar forces is inherently unstable. This instability arises from the long-range and anisotropic nature of the dipole-dipole interaction, where the attractive component dominates [53]. The dipoles tend to align in a head-to-tail configuration along the polarization direction to minimize their energy. Stability can be restored by imposing a sufficiently strong trapping confinement along the polarization axis, which counteracts the collapse [81].

The two outlined features of the dipole-dipole interaction – the long-range and anisotropic nature – make it substantially different from the short-range isotropic contact interaction, and form the basis for the novel properties exhibited by dipolar gases.

2.2. Rotonic excitation spectrum

The study of the stability in ultracold dipolar gases played an important role in achieving and understanding the mechanism underlying the dipolar supersolid state. Stability in a dipolar BEC is determined by a balance between the repulsive contact interaction and the attractive component of the dipole-dipole interaction, being also strongly influenced by the trap geometry [53]. As mentioned earlier, confining the system along the polarization direction increases its stability. Remarkably, it also leads to the emergence of the roton-maxon excitation spectrum, a feature previously observed only in superfluid helium [82, 83]. This was first identified in 2003 by Santos, Shlyapnikov, and Lewenstein in an infinite pancake trap when the system is unconfined in the other two directions [84].

The excitation spectrum of a non-dipolar BEC is characterized by a linear phonon branch at low momenta, transitioning into a quadratic free-particle dispersion at higher momenta [22]. In confined dipolar BECs, this spectrum is significantly modified, featuring a local maximum (maxon) followed by a local minimum (roton), as shown in Fig. 2.2. This qualitative change in the excitation spectrum has important implications for the system's physical behavior. The low energy and large momentum or the roton mode promote the tendency of the fluid to crystallize,

[3]There are several techniques in the literature for tuning the strength of the magnetic dipolar interaction. One example involves using a rapidly rotating magnetic field, where only the projection of the dipole moment along the rotation axis contributes effectively [79, 80]. However, such methods are rarely employed in experiments with dipolar ultracold atomic gases.

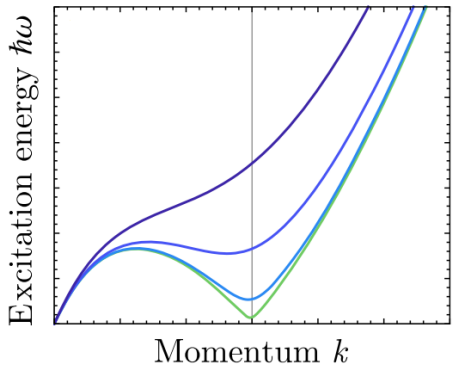

FIG. 2.2.: Schematic of the dispersion relation of an elongated dipolar superfluid. As the scattering length a decreases, a roton minimum emerges in the excitation spectrum, which deepens and eventually approaches zero. Adapted from [88].

leading to the formation of density modulations with a wavelength corresponding to the inverse roton momentum [85–87].

In contrast to helium, the rotonic spectrum in dipolar gases is highly tunable. The presence, position, and depth of the roton minimum can be controlled by varying the particle density, the strength of the confining potential, and the scattering length [84]. For large scattering lengths, corresponding to low values of ϵ_{dd}, the spectrum resembles that of contact-interacting gases, with no roton minimum present. By decreasing the scattering length, or equivalently by increasing ϵ_{dd}, the roton minimum appears and becomes deeper, eventually touching the axis at a certain critical value of ϵ_{dd}. Alternatively, the depth of the roton minimum can be increased by increasing the particle density[4]. When the roton gap fully closes, the system requires no energy to populate the finite-momentum roton state, leading to the spontaneous appearance of spatial periodicity, and hence to the supersolid state.

As previously noted by Pomeau and Rica [33], the authors of [84] also emphasized that the roton-maxon spectrum originates from the momentum dependence of the interparticle interaction. This makes it a general physical phenomenon, potentially present in other systems with momentum-dependent interactions.

Although the dipole-dipole interaction depends solely on the momentum orientation and not explicitly on the norm[5], the momentum-norm dependence of the

[4] A plot illustrating the roton gap value as a function of ϵ_{dd} and particle density for a system in an infinite tube geometry can be found in [89].

excitation spectrum arises from the interplay between the dipole-dipole interaction and the trap's natural length scales [53]. In fact, the position of the roton minimum is closely tied to the confinement strength ω_z along the polarization axis (which is assumed here and throughout to be the z-axis). Specifically, for zero roton energy it is determined by $q_{\text{rot}} = \sqrt{2}/l_z$, where $l_z = \sqrt{\hbar/m\omega}$ is the harmonic oscillator length [84].

Roton mode was experimentally observed in 2018 in a BEC of ^{166}Er atoms confined in a cigar-shaped geometry, with dipoles aligned along a tightly confined direction, by probing the instability dynamics [90]. A year later, the entire phonon-maxon-roton excitation spectrum was measured using Bragg spectroscopy [91]. More recently, rotonic excitations were observed in a ^{162}Dy BEC by studying the in-situ density fluctuations in a cigar-shaped trap [88] and an oblate trap [92].

It is worth highlighting that not all dipolar ultracold gases exhibit a rotonic dispersion relation. As pointed out in [56, 84], the range of ϵ_{dd} values between the onset of the roton mode and the closing of the roton gap is very narrow. For example, in the case of Cr atoms, the dipolar interaction is relatively weak. To access the roton region, one would need to either significantly increase the particle density or reduce the scattering length. However, under such conditions, the three-body losses become significant, and increasing the ϵ_{dd} further leads to the collapse of the system. Nonetheless, this property makes Cr atoms particularly suitable for studying the dynamics of d-wave dipolar collapse [53, 93].

2.3. Beyond-mean-field stabilization

As discussed in the previous section, increasing ϵ_{dd} causes the roton gap to close. However, this also drives the system towards mechanical instability and collapse, as the attractive dipolar interaction outweighs the repulsive contact interaction. On the mean-field level, this collapse occurs even before the roton gap fully closes, preventing the condensate from reaching the favorable conditions for supersolidity.

An important step towards understanding the mechanism of the supersolid phase was the inclusion of beyond-mean field effects, known as quantum fluctuations. These higher-order contributions arise from interactions that induce fluctuations in the vacuum of excitations, leading to a reduction in condensate density – an effect known as condensate depletion. While typically negligible, in systems with

[5]This is more evident from the Fourier transform of the dipole-dipole interaction entering the Gross-Pitaevskii equation, which will be discussed in Chapter 4.

competing attractive and repulsive interactions, quantum fluctuations become significant. The individual interaction strengths are large, but the overall mean-field terms nearly cancel out, making beyond-mean-field effects essential.

Quantum fluctuations influence the equation of state in two ways. The dominant effect is the introduction of an additional energy term that acts as an effective repulsive interaction. The secondary effect is a reduction in condensate density, which in turn weakens the mean-field attraction. Quantum fluctuations stabilize the system against collapse, allowing the roton gap to fully close. This leads to expanding the phase diagram and the emergence of novel quantum states: supersolids and quantum droplets.

The correction to the equation of state can be calculated within Bogoliubov theory, by assuming that the condensate occupation is not complete (at zero temperature), but remains macroscopic [22]. Within the mean-field theory, the field operator $\hat{\Psi}$ can simply be replaced by a complex value Ψ, representing the condensate wave function. To include beyond-mean-field effects, the field operator is instead expressed as $\hat{\Psi} = \Psi + \delta\hat{\psi}$, where $\delta\hat{\psi}$ accounts for the quantum fluctuations. The correction was first calculated for non-dipolar BECs in 1957 by Lee, Huang, and Yang [94, 95], and is therefore known as the LHY correction. For dipolar BECs, the LHY correction was derived in 2011 by Lima and Pelster[6] [96, 97].

The corrections to the energy and the condensate density are given by the following expressions:

$$\frac{\Delta E}{V} = \frac{64}{15\sqrt{\pi}}\, g n_0^2 \sqrt{n_0 a^3}\, Q_5(\epsilon_{\mathrm{dd}}), \tag{2.6}$$

$$\Delta n = \frac{8}{3\sqrt{\pi}}\, n_0 \sqrt{n_0 a^3}\, Q_3(\epsilon_{\mathrm{dd}}), \tag{2.7}$$

where $n_0 = |\Psi|^2$ is the condensate density, V is the volume, and the functions $Q_l(\epsilon_{\mathrm{dd}})$ are defined as:

$$Q_l(x) = \int_0^1 du \left[1 + x(3u^2 - 1)\right]^{l/2}. \tag{2.8}$$

Beyond-mean-field corrections are proportional to the square root of the so-called gas parameter na^3, which is a measure of the interaction strength in the system.

The functions Q_3 and Q_5 are monotonically increasing over the domain $\epsilon_{\mathrm{dd}} \in [0, 1]$. For $\epsilon_{\mathrm{dd}} = 0$, the original LHY correction for contact-interacting BECs is recovered.

[6] A similar, though less explicit, calculation was performed in 2006 [98]. The authors considered the general form of weak, finite-range two-particle interaction potentials, with a particular focus on dipole-dipole interactions.

For $\epsilon_{\rm dd} > 1$, the integrals acquire an imaginary component, which is precisely the region where quantum fluctuations become significant, as the system is mechanically stable otherwise. However, this imaginary part remains very small for $\epsilon_{\rm dd} \lesssim 3$ and is therefore typically ignored in calculations [53].

The above equations are valid for infinite homogeneous systems. In the presence of a trapping potential, the local-density approximation (LDA) must be employed. This approximation assumes that the density varies slowly enough to allow the use of the homogeneous equations locally. Another key assumption is neglecting condensate depletion, i.e. assuming the full occupation of the condensate. In current experimental setups, quantum depletion is typically of the order of a few percent, making this a reasonable approximation [53]. Under these conditions, a local energy shift can be calculated, leading to the following expression for the change in the chemical potential:

$$\Delta\mu = \frac{32}{3\sqrt{\pi}}\, gn\sqrt{na^3}\,\mathrm{Re}\left[Q_5(\epsilon_{\rm dd})\right]. \tag{2.9}$$

Incorporating this correction into the equation of motion allows for the proper treatment of dipolar supersolid [56] and droplet phases [99].

It is important to note that the stabilization mechanism driven by beyond-mean-field effects was originally proposed by Petrov in 2015 for condensed Bose-Bose mixtures [100]. In this scenario, quantum fluctuations prevent the mean-field collapse caused by interspecies attraction, resulting in the formation of a dilute droplet state. However, no supersolid state was observed in this case. This highlights the universality of the quantum stabilization mechanism across different types of interactions.

2.4. Phases of the dipolar BEC

The interplay between mean-field attractive and beyond-mean-field repulsive contributions gives rise to three distinct phases in dipolar BECs: the superfluid, supersolid, and isolated droplet phases. Transitions between these phases can be achieved by tuning the parameter $\epsilon_{\rm dd}$ (via the scattering length a) or by varying the particle density. Experimentally, tuning $\epsilon_{\rm dd}$ is more practical, as the number of particles in the condensate remains fixed for a given experimental trial.

The phase transition between the supersolid and droplet phase is continuous, whereas the transition between the supersolid and superfluid phase is discontinuous in two-dimensional configurations, and can be either continuous or discontinuous

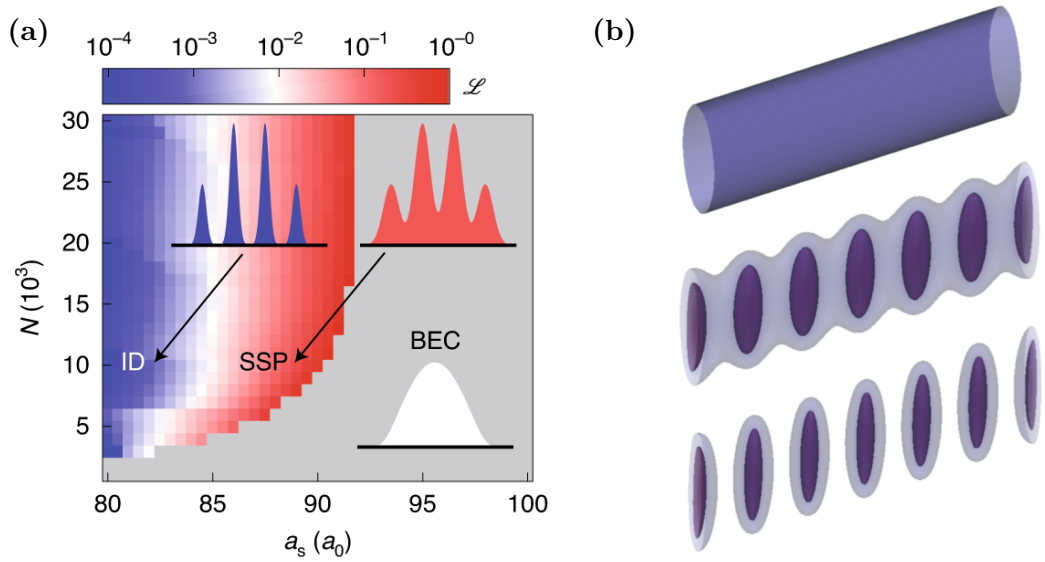

FIG. 2.3.: (a) Numerically obtained ground-state phase diagram for a cigar-shaped dipolar Bose gas with transverse dipole orientation. The diagram shows three phases: the non-modulated BEC phase (gray region), the supersolid phase (red region), and the isolated droplet phase (blue region). The insets show the corresponding integrated density profiles. The colormap represents the link strength $\mathcal{L}$, which quantifies the connectivity between droplets (for more details see the original reference). Adapted from [57]. (b) Density profiles of a dipolar Bose gas in an infinite tube geometry, where the gas is harmonically confined along the two directions and unconfined along the third.

in one-dimensional configurations, depending on the condensate density [101, 102]. An example of the phase diagram for a harmonically trapped cigar-shaped dipolar BEC with transverse dipole orientation is shown in Fig. 2.3(a). The density profiles of the three phases in an infinite tubular geometry are shown in Fig. 2.3(b).

The superfluid phase occurs at low values of ϵ_{dd}. It is characterized by a uniform density profile in homogeneous systems (or a shape conforming to the the external potential in trapped systems) and long-range phase coherence. Deep within this regime, the system behaves as a conventional Bose-Einstein condensate. Approaching the transition to the supersolid phase, the dispersion relation develops a rotonic structure (Fig. 2.4(a)), and the superfluid enters a mean-field unstable region where stabilization is provided by quantum fluctuations.

At large values of ϵ_{dd} the roton gap closes, and the frequency of the roton mode becomes imaginary [84]. This triggers a modulational instability, characterized by a collection of local collapses stabilized by quantum fluctuations, resulting in the formation of an ordered structure of quantum droplets [53, 99]. Quan-

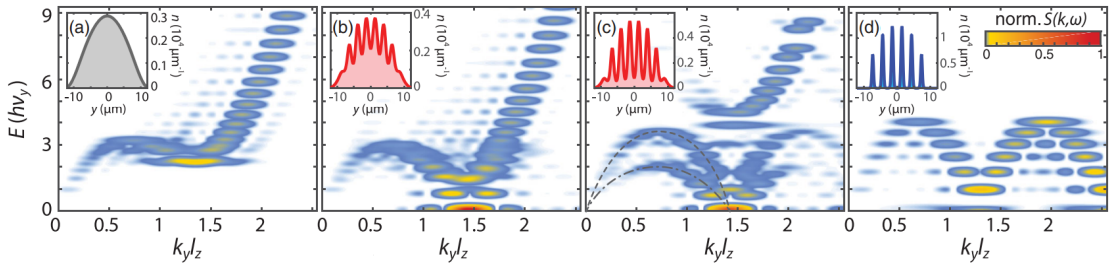

FIG. 2.4.: Numerically calculated excitation spectrum of an axially elongated, harmonically trapped dipolar quantum gas across the superfluid-supersolid-droplet phase transition. The insets show the integrated ground-state density distributions. The colormap represents the dynamic structure factor norm, while the dotted lines serve as a guide to the eye, highlighting the two excitation branches in the supersolid phase. Adapted from [61].

tum droplets in dipolar gases were first observed experimentally in 2016, both in pancake-shaped [103] and cigar-shaped traps [104, 105].

The term "quantum droplets" stems from their liquid-like properties. Although they are denser than a gaseous BEC, their density is several orders of magnitude lower than that of ordinary liquids (≈ 8). At high atom numbers, the droplet density saturates. Adding more particles increases the droplet size rather than the density, indicating the low compressibility typical of a liquid phase [54]. They have an anisotropic shape stemming from the anisotropy of the dipole-dipole interaction, and their spatial arrangement results from the repulsion between macroscopic dipoles.

Quantum droplets are remarkably stable and long-lived, with their lifetime primarily limited by atom losses caused by three-body recombination processes, which increase with higher density. They are self-bound states that can exist even in the absence of external trapping, which was described theoretically by the balance between mean-field and LHY terms [106, 107], and observed experimentally [108]. While each droplet is superfluid itself, there is no global phase coherence between them; they evolve as independent entities and do not exhibit a supersolid state. The dispersion relation for a one-dimensional droplet crystal shows a single gapless excitation, corresponding to the phonon mode of the crystal lattice (Fig. 2.4(d)). For a more comprehensive overview of quantum droplets, see recent reviews [53, 54].

The supersolid phase exists in the narrow range of scattering length values (on the order of a few a_0) between the superfluid and droplet phases, where quantum droplets overlap, creating a density link that maintains the global phase coher-

ence. The excitation spectrum of the supersolid phase is characterized by two gapless branches[7]: a crystal phonon mode and a phase (superfluid) phonon mode (Fig. 2.4(c)) [56, 109]. These correspond to the two Goldstone modes associated with the spontaneous breaking of translational symmetry and U(1) phase invariance. The phase branch, which is lower in energy, decreases further as ϵ_{dd} increases and eventually vanishes as the system transitions to the droplet phase. Due to the finite size of the system available in present experiments, the continuous dispersion relation acquires a form of series of discrete energy levels, as shown in Fig. 2.4 [61].

At low densities, the width of the supersolid phase is so narrow that the phase transition occurs directly between the superfluid and droplet phases. This is one reason why quantum droplets were discovered and studied before the supersolid state, as early experiments were limited to systems with low particle numbers. At higher densities, the phase diagram shows a richer variety of quantum phases, including the stripe supersolid phase, as well as honeycomb and labyrinth phases, characterized by structures of density holes surrounded by condensed atoms [110, 111].

[7] In the case of a one-dimensional supersolid configuration, where only one translational symmetry is broken.

3

Theoretical description

This chapter presents the theoretical framework and numerical methods used to describe dipolar Bose-Einstein condensates, and in particular supersolids. Two approaches are central to the theoretical description: the microscopic Gross-Pitaevskii theory, which describes the system through the condensate wave function, and the macroscopic hydrodynamic theory, which describes it in terms of slow-varying fields. These two frameworks are expected to be consistent in the long-wavelength phonon limit.

We introduce the extended Gross-Pitaevskii equation, which provides the evolution of the order parameter, and includes beyond-mean-field corrections essential for studying the dipolar supersolid phase. Its stationary form is used to determine the ground state of the system, while the elementary excitations are analyzed using the Bogoliubov-de Gennes formalism. The concept of the superfluid fraction is introduced as a key parameter for characterizing the supersolid phase.

A hydrodynamic description of one-dimensional supersolids is described, which is based on conservation laws and broken symmetries. Linearization of the hydrodynamic equations allows to study the collective modes of the system. In the case of supersolids, this results in two sound modes, which correspond to Goldstone modes arising from the simultaneous and spontaneous breaking of U(1) symmetry and Galilean invariance, a defining feature of supersolids.

3.1. Gross-Pitaevskii equation

A many-body system of bosonic particles of mass m, subject to an external potential $V_{\text{ext}}(\mathbf{r})$ and interacting via a two-body potential $V(\mathbf{r}-\mathbf{r}')$, is described

within the second quantization formalism by the following Hamiltonian, expressed in terms of the field operators [22]:

$$\begin{aligned}\hat{H} = &\int d\mathbf{r}\hat{\Psi}^\dagger(\mathbf{r})\left(-\frac{\hbar^2\nabla^2}{2m} + V_{\text{ext}}(\mathbf{r})\right)\hat{\Psi}(\mathbf{r}) \\ &+ \frac{1}{2}\iint d\mathbf{r}d\mathbf{r}'\hat{\Psi}^\dagger(\mathbf{r})\hat{\Psi}^\dagger(\mathbf{r}')V(\mathbf{r}-\mathbf{r}')\hat{\Psi}(\mathbf{r}')\hat{\Psi}(\mathbf{r}).\end{aligned} \tag{3.1}$$

The field operators $\hat{\Psi}^\dagger(\mathbf{r})$ and $\hat{\Psi}(\mathbf{r})$ create and annihilate a particle at position $\mathbf{r}$, respectively, and satisfy the bosonic commutation relations. In the Heisenberg picture, the time evolution of the field operator follows from its commutator with the Hamiltonian:

$$\begin{aligned}i\hbar\frac{\partial}{\partial t}\hat{\Psi}(\mathbf{r},t) =& \left[\hat{\Psi}(\mathbf{r},t), \hat{H}\right] = \\ =& \Bigg[-\frac{\hbar^2\nabla^2}{2m} + V_{\text{ext}}(\mathbf{r},t) \\ &+ \int d\mathbf{r}'\hat{\Psi}^\dagger(\mathbf{r}',t)V(\mathbf{r}-\mathbf{r}')\hat{\Psi}(\mathbf{r}',t)\Bigg]\hat{\Psi}(\mathbf{r},t).\end{aligned} \tag{3.2}$$

At zero temperature ($T = 0$K), a system of bosonic particles undergoes Bose-Einstein condensation, resulting in a macroscopic occupation of the lowest-energy state. Following the Bogoliubov theory, the presence of large number of atoms in a single quantum state allows the field operator to be expressed in terms of a classical field $\Psi(\mathbf{r},t)$, representing the condensate wave function (which is also the order parameter of the broken U(1) symmetry), and a quantum field $\delta\hat{\psi}(\mathbf{r},t)$, corresponding to quantum fluctuations:

$$\hat{\Psi}(\mathbf{r},t) = \Psi(\mathbf{r},t) + \delta\hat{\psi}(\mathbf{r},t). \tag{3.3}$$

In the dilute ($nb^3 \ll 1$) and weakly interacting ($na^3 \ll 1$) regime, the two-body interaction potential is well approximated by an effective short-range contact interaction, given by Eq. (2.1) (see section 2.1.1): $V(\mathbf{r}) = g\delta(\mathbf{r})$, with the coupling constant $g = 4\pi\hbar^2 a/m$. Within mean-field theory, which corresponds to the lowest-order approximation, quantum fluctuations are neglected, and the field operator is simply replaced by a complex function. Substituting this into the equation of motion (3.2) leads to the well-known Gross-Pitaevskii equation (GPE):

$$i\hbar\frac{\partial}{\partial t}\Psi(\mathbf{r},t) = \left[-\frac{\hbar^2\nabla^2}{2m} + V_{\text{ext}}(\mathbf{r},t) + g|\Psi(\mathbf{r},t)|^2\right]\Psi(\mathbf{r},t). \tag{3.4}$$

The GPE was derived independently by Gross [112] and Pitaevskii [113] in 1961 to describe vortex lines in weakly repelling Bose gases. It has been shown to accurately describe most properties of dilute BECs [22, 23, 114, 115].

For dipolar Bose gases, the two-body interaction potential is extended to include the dipole-dipole interaction, given by Eq. (2.3) and reprinted here for completeness:

$$V_{\mathrm{dd}}(\mathbf{r}-\mathbf{r}') = \frac{3a_{\mathrm{dd}}\hbar^2}{m}\frac{1-3\cos^2\theta}{|\mathbf{r}-\mathbf{r}'|^3}. \tag{3.5}$$

To describe beyond-mean-field stabilized states, such as supersolids, it is necessary to account for quantum fluctuations. The derivation within the local density approximation involves expressing the Hamiltonian for a homogeneous system in the momentum basis while retaining only terms up to second order in $\delta\hat{\psi}(\mathbf{r},t)$. The Hamiltonian is then diagonalized through the introduction of Bogoliubov transformations [116] for the creation and annihilation operators. Additionally, a higher-order Born approximation is required for a proper treatment of the effective contact potential. The results of this procedure are presented in Section 2.3, where the correction to the chemical potential is given by Eq. (2.9), while a detailed derivation can be found in [94–97].

By incorporating both the DDI and the LHY correction into the GPE, the so-called extended Gross-Pitaevskii equation (eGPE) for dipolar BECs is obtained:

$$\begin{aligned} i\hbar\frac{\partial}{\partial t}\Psi(\mathbf{r},t) = \Bigg[&-\frac{\hbar^2\nabla^2}{2m} + V_{\mathrm{ext}}(\mathbf{r},t) + g|\Psi(\mathbf{r},t)|^2 \\ &+ \int d\mathbf{r}' V_{\mathrm{dd}}(\mathbf{r}-\mathbf{r}')|\Psi(\mathbf{r}',t)|^2 + \gamma(\epsilon_{\mathrm{dd}})|\Psi(\mathbf{r},t)|^3\Bigg]\Psi(\mathbf{r},t), \end{aligned} \tag{3.6}$$

where we introduced

$$\gamma(\epsilon_{\mathrm{dd}}) = \frac{32}{3\sqrt{\pi}}ga^{3/2}\mathrm{Re}\left[\int_0^1 du\left[1+\epsilon_{\mathrm{dd}}(3u^2-1)\right]^{5/2}\right]. \tag{3.7}$$

Here, we neglected the correction to the particle density due to condensate depletion (Eq (2.7)), assuming that the condensate wave function is normalized to the total number of particles N:

$$\int d\mathbf{r}|\Psi(\mathbf{r},t)|^2 = N. \tag{3.8}$$

The stationary solutions of the eGPE are obtained by assuming that only the phase of the condensate wave function evolves in time, according to the law:

$$\Psi(\mathbf{r},t) = \psi_0(\mathbf{r})e^{-i\mu t/\hbar}. \tag{3.9}$$

The time evolution of the order parameter is governed by the chemical potential $\mu = \partial E/\partial N$, rather than the energy. The eGPE then reduces to the time-independent form:

$$\mu\psi_0(\mathbf{r}) = \Bigg[-\frac{\hbar^2\nabla^2}{2m} + V_{\text{ext}}(\mathbf{r}) + g|\psi_0(\mathbf{r})|^2 + \int d\mathbf{r}' V_{\text{dd}}(\mathbf{r}-\mathbf{r}')|\psi_0(\mathbf{r}')|^2 + \gamma(\epsilon_{\text{dd}})|\psi_0(\mathbf{r})|^3 \Bigg] \psi_0(\mathbf{r}). \tag{3.10}$$

The ground-state wave function corresponds to the solution of this eigenproblem associated with the lowest energy.

Alternatively, ground state wave function can be obtained by minimizing the energy functional

$$E[\Psi] = \int d\mathbf{r} \Bigg[\Psi^*(\mathbf{r}) \left(-\frac{\hbar^2\nabla^2}{2m} \right) \Psi(\mathbf{r}) + V_{\text{ext}}(\mathbf{r})|\Psi(\mathbf{r})|^2 + \frac{g}{2}|\Psi(\mathbf{r})|^4 \frac{1}{2}\int d\mathbf{r}' V_{\text{dd}}(\mathbf{r}-\mathbf{r}')|\Psi(\mathbf{r}')|^2|\Psi(\mathbf{r})|^2 + \frac{2}{5}\gamma(\epsilon_{\text{dd}})|\Psi(\mathbf{r})|^5 \Bigg] \tag{3.11}$$

with respect to variations of $\Psi^*(\mathbf{r})$, with the constraint of the normalization condition (3.8), where the chemical potential enters as a Lagrange multiplier: $\delta(E - \mu N) = 0$.

The eGPE has been extensively used in recent years to describe the equilibrium and dynamical properties of dipolar supersolids, providing good level of agreement with experimental observations [53, 54, 99].

3.2. Bogoliubov-de Gennes equations

The description of collective excitations in ultracold quantum gasses is centered around the Bogoliubov-de Gennes (BdG) formalism [22]. To study small fluctuations around the ground state of the extended GPE, we express the wave function using a Bogoliubov expansion:

$$\Psi(\mathbf{r},t) = e^{-i\mu t/\hbar}\Big(\psi_0(\mathbf{r}) + \delta\Psi(\mathbf{r},t)\Big), \tag{3.12}$$

where $\psi_0(\mathbf{r})$ is the stationary condensate wavefunction, which satisfies Eq. (3.10), and $\delta\Psi(\mathbf{r},t)$ represents small perturbations that can be expanded in the quasiparticle basis as

$$\delta\Psi(\mathbf{r},t) = \sum_n \Big[u_n(\mathbf{r})e^{-i\omega_n t} + v_n^*(\mathbf{r})e^{i\omega_n t} \Big]. \tag{3.13}$$

Here, $u_n(\mathbf{r})$ and $v_n(\mathbf{r})$ describe quasiparticle excitations with frequency ω_n. Both forward and backward propagating terms are needed, since eGPE couples Ψ and Ψ^*. These functions satisfy the following orthogonality relations:

$$\int d\mathbf{r}\,[u_n u_m^* - v_n v_m^*] = \delta_{nm} \tag{3.14}$$

$$\int d\mathbf{r}\,[u_n v_m - v_n u_m] = 0. \tag{3.15}$$

In the absence of stationary currents, the condensate wavefunction $\psi_0(\mathbf{r})$ can be chosen to be real. Substituting the Bogoliubov expansion into the eGPE (3.6) and retaining only linear terms in u_n and v_n, the following BdG equations for a dipolar BEC are obtained:

$$\begin{bmatrix} \hat{H} - \mu + \hat{X} & \hat{X} \\ -\hat{X} & -(\hat{H} - \mu + \hat{X}) \end{bmatrix} \begin{bmatrix} u_n \\ v_n \end{bmatrix} = \hbar\omega_n \begin{bmatrix} u_n \\ v_n \end{bmatrix} \tag{3.16}$$

Here, $\hat{H}$ denotes the Hamiltonian of the stationary eGPE (3.10), given by

$$\hat{H} = -\frac{\hbar^2\nabla^2}{2m} + V_{\text{ext}}(\mathbf{r}) + g\psi_0^2(\mathbf{r}) + \gamma\psi_0^3(\mathbf{r}) + \int d\mathbf{r}' V_{\text{dd}}(\mathbf{r}-\mathbf{r}')\psi_0^2(\mathbf{r}'), \tag{3.17}$$

and the operator $\hat{X}$ is defined through its action on a general function $f(\mathbf{r})$ as:

$$\hat{X}f(\mathbf{r}) = \left[g\psi_0^2(\mathbf{r}) + \frac{3}{2}\gamma\psi_0^3(\mathbf{r})\right] f(\mathbf{r}) + \psi_0(\mathbf{r}) \int d\mathbf{r}' V_{\text{dd}}(\mathbf{r}-\mathbf{r}')\psi_0(\mathbf{r}')f(\mathbf{r}'). \tag{3.18}$$

Solving this eigenvalue problem determines the eigenfrequencies ω_n and eigenfunctions u_n and v_n which characterize the elementary excitations of a dipolar BEC.

3.3. Superfluid fraction

The superfluid fraction f_s is a measure of the proportion of a system that exhibits superfluidity. Leggett introduced a definition of the superfluid fraction based on the concept of non-classical rotational inertia [7, 117]. When a partially superfluid system is placed under slow rotation, the superfluid component remains stationary, leading to a reduction in the system's moment of inertia. The fraction of this decrease directly corresponds to the superfluid fraction. Leggett originally formulated this definition for a system confined in a cylindrical (or toroidal) container with circumference R significantly larger than its transverse size, rotating with angular velocity Ω:

$$f_s \equiv 1 - \lim_{\Omega\to 0} \frac{\langle J\rangle}{\Omega I_{\text{rig}}} = 1 - \frac{I}{I_{\text{rig}}}. \tag{3.19}$$

Here, $\langle J \rangle$ is the expectation value of the angular momentum, I is the moment of inertia of the system, and $I_{\text{rig}} = NmR^2$ is its classical rigid-body value, with m the mass of the particles. An equivalent definition can be derived for a system confined in a long tube with periodic boundary conditions. In this case, the superfluid fraction is given by:

$$f_s = 1 - \lim_{v \to 0} \frac{\langle P \rangle}{Nmv}, \tag{3.20}$$

with $\langle P \rangle$ the expectation value of the total linear momentum in the reference frame moving with velocity v.

In the context of superfluid helium, the superfluid fraction is given by

$$f_s = \frac{\rho_s}{\rho}. \tag{3.21}$$

Here, ρ_s comes from the Tisza-Landau two-fluid model [118, 119], in which the system consists of a superfluid component with zero viscosity (ρ_s), and a normal component (ρ_n), with the total density being the sum of the two:

$$\rho = \rho_s + \rho_n. \tag{3.22}$$

Similarly, the total current is given by:

$$j = \rho_s v_s + \rho_n v_n, \tag{3.23}$$

where v_s and v_n are the velocities of the superfluid and normal components, respectively.

The superfluid fraction depends on temperature. In helium, superfluidity vanishes above the lambda transition, and the superfluid fraction is equal to zero. As the temperature decreases, the superfluid fraction increases, approaching unity in the zero temperature limit: $\lim_{T \to 0} f_s = 1$. However, as predicted by Leggett, in systems that break translational invariance, either explicitly through the Hamiltonian or spontaneously in the ground state, the superfluid fraction remains below unity even at zero temperature [117]. Consequently, a zero-temperature supersolid is expected to exhibit a reduced superfluid fraction, and can be effectively described as a two-component system comprising of both superfluid and normal components.

Using a variational approach, Leggett derived a rigorous upper bound for the superfluid fraction, in terms of the ground state density distribution:

$$f_s^+ = \left[\frac{1}{2\pi} \int_0^{2\pi} \frac{d\theta}{n(\theta)/n_0} \right]^{-1} = \left[\frac{1}{L} \int_0^{L} \frac{dx}{\int dy\, dz\, n(x,y,z)} \right]^{-1} \tag{3.24}$$

Here, $n(\theta)$ is the integrated density, averaged over the cross-section of the annulus, and n_0 its average over θ. The second formula provides the corresponding expression in Cartesian coordinates.

The formula shows that the superfluid fraction is maximized when the density is uniform, giving $f_s^+ = 1$. Any spatial modulation reduces this value below unity. If the linear density vanishes at any point, the upper bound reduces to zero, indicating that a disconnected system cannot sustain superfluid flow.

Leggett also proposed a heuristic lower bound for the superfluid fraction:

$$f_s^- = 2\pi \int dr_\perp \left[\int \frac{d\theta}{n(\theta, r_\perp)} \right]^{-1} \tag{3.25}$$

Although not as rigorous as the upper bound, it provides an additional constraint on possible values of f_s. If the density is separable $n = n(\theta)\, n(r_\perp)$, the two bounds coincide.

Leggett's bounds are expected to provide a very good estimate of the superfluid fraction within the Gross-Pitaevskii theory [102, 120]. In particular, the three formulas ((3.20), (3.24), (3.25)) show a very good agreement in an infinite tube potential. The reduction of the superfluid fraction has recently been measured in an externally modulated BEC via speed of sound measurement [121] and in a dipolar supersolid through the observation of the Josephson effect [122].

3.4. Hydrodynamic theory of supersolids

Hydrodynamic theories describe macroscopic, collective behavior and apply in the long-wavelength, low-energy limit, where individual particle motion becomes less relevant [123]. The system is described by continuous fields, such as density and velocity, neglecting the discrete nature of individual particles, which is valid when the number of particles is large. Rather than resolving microscopic details, hydrodynamics captures large-scale dynamics, both spatial and temporal. Hydrodynamics is based on conservation laws, such as the conservation of mass, momentum and energy, accounting also for broken symmetries. These principles introduce constraints on the hydrodynamic variables, shaping the system's behavior.

Hydrodynamics assumes that the system is in local equilibrium. In classical systems, local equilibrium is ensured through frequent particle collisions, which lead to rapid thermalization and energy redistribution. In contrast, superfluids exist at very low temperatures, where particles collisions are negligible, resulting in zero

viscosity and frictionless flow. Local equilibrium in superfluids is instead ensured through the global coherence of the macroscopic wave function. For this reason, superfluid hydrodynamics is often referred to as *collisionless hydrodynamics*.

The hydrodynamic description applies to a wide range of systems, including normal fluids and solids, as well as superfluids and supersolids. It remains valid in both strongly interacting (e.g., liquid helium) and weakly interacting regimes (e.g., ultracold gases). It is suitable for studying both zero and finite temperature systems. In contrast, the Gross-Pitaevskii theory provides a more fundamental, microscopic description of weakly interacting, zero-temperature superfluids through a wave function formalism. The GPE can be transformed into hydrodynamic equations, thus obtaining its long-wavelength limit [22].

3.4.1. Supersolid hydrodynamic equations

The number of collective hydrodynamic modes of the system is based on the number of conserved quantities and broken symmetries [124]. For a three dimensional supersolid there are conservation of mass, three components of momentum, and energy. Additionally, there are three broken translational symmetries and one broken U(1) symmetry. Therefore, there are a total of nine hydrodynamic modes, which include two pairs of transverse propagating sound modes, one pair of longitudinal first sound modes, a pair of longitudinal second sound modes, and a heat diffusion mode [125, 126]. Propagating modes are counted twice in the hydrodynamic counting because the dispersion relation $\omega = \pm ck$ gives two solutions, corresponding to a forward- and a backward-propagating mode. The existence of the longitudinal second sound mode is one of the key signatures of supersolids[1].

We consider a one-dimensional supersolid configuration at zero temperature. In this case, the energy conservation law, which corresponds to the heat diffusion mode, is disregarded, along with two components of the momentum conservation law and the broken translational symmetry, which correspond to transverse modes. The resulting hydrodynamic description of the supersolid is then given by the following equations (see, e.g., [126–130]):

$$\partial_t \rho + \partial_x j = 0 \tag{3.26}$$

$$\partial_t j + \partial_x (p + \rho_n v_n^2 + \rho_s v_s^2) = 0 \tag{3.27}$$

$$\partial_t v_s + \partial_x (\mu + v_n v_s) = 0 \tag{3.28}$$

$$\partial_t u_x + \partial_x (v_n u_x - v_n) = 0 \tag{3.29}$$

[1] Not to be confused with first and second sound in superfluid helium.

These equations are expected to generate four longitudinal modes, forming two degenerate pairs in the absence of currents.

The first equation is the continuity equation, describing the conservation of mass, or equivalently, particle number. The total density ρ is given by Eq. (3.22), and the total current j by Eq. (3.23). As noted earlier, we assume that a supersolid at zero temperature consists of both superfluid and normal components, since the system breaks translational invariance [117]. The second equation follows from the momentum conservation law. The first two equations are valid for any (non-dissipative) classical fluid at zero temperature, differing only in the specific form of the driving currents.

The third equation is the Josephson equation, which arises from the spontaneous breaking of U(1) symmetry and the onset of superfluidity. It describes the evolution of the superfluid velocity, driven by the chemical potential, and is a general result of superfluid hydrodynamics [131, 132]. The additional term $v_n v_s$ comes from the change of the reference frame. In its original form, the Josephson equation states that the evolution of v_s is governed by $\mu_s + v_s^2/2$, where μ_s is the chemical potential in the superfluid reference frame. It is related to the rest-frame chemical potential μ by the relation $\mu_s - \mu = v_s v_n - v_s^2/2$. In a fully superfluid system where $\rho_n = 0$, the second equation reduces to a linear combination of the first and third. Therefore, the superfluid hydrodynamic description is given by the continuity equation and the Josephson equation.

The fourth equation arises from the spontaneous breaking of translational symmetry and the formation of a periodic lattice and long-range crystalline order. It describes the evolution of $u_x := \partial_x u$, where u is the lattice displacement and x denotes the direction of periodic modulation. The equation follows from Lin's constraint [126]:

$$(\partial_t + v_n \partial_x) R = 0, \tag{3.30}$$

where R is the position of the lattice site. Using the relation $x = R + u$ and differentiating the above equation with respect to x gives Eq. (3.29).

3.4.2. Sound velocities

Hydrodynamic modes are obtained by linearizing Eqs. (3.26) - (3.29). This is achieved by considering small variations of the hydrodynamic variables around their equilibrium values ρ_0 and $v_s^0 = v_n^0 = u_x^0 = 0$, as $\rho(x,t) = \rho_0(x) + \delta\rho(x,t)$,

$v_s(x,t) = \delta v_s(x,t)$, $v_n(x,t) = \delta v_n(x,t)$, $u_x(x,t) = \delta u_x(x,t)$. This results in the following system of equations:

$$\partial_t \delta\rho + \partial_x \delta j = 0 \tag{3.31}$$
$$\partial_t \delta j + \partial_x \delta p = 0 \tag{3.32}$$
$$\partial_t \delta v_s + \partial_x \delta\mu = 0 \tag{3.33}$$
$$\partial_t \delta u_x - \partial_x \delta v_n = 0. \tag{3.34}$$

The thermodynamic forces are then expanded to leading order in the hydrodynamic variables. The chemical potential and pressure have a quadratic dependence on the normal and superfluid velocities relative to their stationary values [133], and can therefore be neglected at linear order. Additionally, we neglect the strain-density coupling $\gamma = \partial\mu/\partial u_x = \partial^2\mathcal{E}/\partial\rho\partial u_x$, where $\mathcal{E}$ is the energy density, which has been shown to be very small in the supersolid phase [134]. The constitutive relations then take the form:

$$\delta j = \rho_n^0 \delta v_n + \rho_s^0 \delta v_s \tag{3.35}$$
$$\delta\mu = \frac{1}{\rho_0\kappa}\delta\rho \tag{3.36}$$
$$\delta p = \frac{1}{\kappa}\delta\rho - \lambda\delta u_x, \tag{3.37}$$

where $\kappa = (\rho\,\partial\mu/\partial\rho)^{-1}$ is the compressibility, and $\lambda = \partial\mathcal{E}/\partial u_x$ is the elastic constant, also called the layer compressibility modulus. In one-dimensional structure, λ is the only elastic constant, corresponding to the energy cost due to the change in the separation between the peaks, i.e. the resistance to compression of the layers. In the following we drop the index 0 for brevity.

By transforming the linearized hydrodynamic equations into Fourier space, the system of partial differential equations reduces to a system of algebraic equations. This is equivalent to looking for solutions of the form $f(x,t) = f_\omega \exp\{i(qx - \omega t)\}$, where $f = \{\delta\rho, \delta v_n, \delta v_s, \delta u_x\}$. The resulting equations can be expressed in matrix form:

$$\begin{bmatrix} -\omega/q & \rho_n & \rho_s & 0 \\ 1/\rho_n\kappa & -\omega/q & -\omega\rho_s/q\rho_n & -\lambda/\rho_n \\ 1/\rho\kappa & 0 & -\omega/q & 0 \\ 0 & -1 & 0 & -\omega/q \end{bmatrix} \begin{bmatrix} \delta\rho \\ \delta v_n \\ \delta v_s \\ \delta u_x \end{bmatrix} = 0, \tag{3.38}$$

where ω is the mode frequency and q is the associated wavevector. This approach identifies phononic excitations following the dispersion relation $\omega = c|q|$, where c is the speed of sound. By setting the determinant of the above matrix to zero and solving the resulting quartic polynomial, the two speeds of sound are obtained:

$$c_\pm^2 = \frac{c_\kappa^2}{2}\left(1 + \beta\kappa \pm \sqrt{(1+\beta\kappa)^2 - 4f_s\beta\kappa}\right), \tag{3.39}$$

where we introduced $c_\kappa = \sqrt{\kappa^{-1}}$, and the renormalized compressibility modulus $\beta = \lambda/\rho_n$.

The obtained result corresponds to four sound modes with double degenerate velocities, meaning forward- and backward-propagating waves travel at the same speed. In the presence of nonzero currents, $v_s \neq 0$ and $v_n \neq 0$, these velocities split into four distinct sound modes due to the Doppler effect. This phenomenon was recently analyzed in a study I coauthored [135].

4

Numerical methods

In this chapter, we present the numerical methods used to study dipolar Bose-Einstein condensates. Due to the nonlinear and nonlocal nature of the extended Gross-Pitaevskii equation, analytical solutions are generally not available, making numerical approaches essential for obtaining solutions.

The ground-state wave function of the system is determined using an imaginary-time evolution of the eGPE (3.6), or, equivalently, by minimizing the energy functional (3.11) through a gradient descent method. Convergence is accelerated using the heavy-ball method. The dynamics of the system is studied by evolving the ground-state wavefunction in real time using the eGPE. The numerical integration is performed using the fourth-order Runge-Kutta method. Elementary excitations are analyzed by solving the Bogoliubov-de Gennes eigenproblem (3.16), employing ARPACK-NG routines. The non-local terms and spatial derivations are calculated in Fourier space, which also naturally imposes periodic boundary conditions.

The numerical implementation requires discretization of the wave function in both space and time. We use a Cartesian grid with a uniform step size in both spatial and temporal dimensions. Additionally, all equations are cast into a dimensionless form to improve numerical stability and efficiency. The details of this process are provided in Appendix A.

The numerical codes used in this work were initially developed within our research group and have been modified and improved based on the needs of the particular system under study. The ground-state computation and time-evolution codes are written in Fortran 2003 and are parallelized for GPU acceleration using the NVIDIA HPC-SDK toolkit. The BdG solver is implemented in C++ [136], relying on the Intel oneAPI Base/HPC Toolkits and OpenMP for CPU paralelization. The simulations are conducted on the Galileo100 cluster of the CINECA supercomputer and the Marzola cluster at the University of Trento. The outputs of these simulations are subsequently analyzed using MATLAB.

4.1. Ground state calculation

4.1.1. Imaginary-time evolution

The ground state of the system is determined using the well-established imaginary-time evolution method applied to the eGPE [137]. In this approach, the real-time variable is transformed into an imaginary quantity. Starting from the eGPE 3.6, which can be rewritten in the form

$$i\frac{\partial}{\partial t}\Psi = \hat{H}\Psi, \tag{4.1}$$

with the extended Gross-Pitaevskii Hamiltonian

$$\hat{H} = -\frac{\hbar^2\nabla^2}{2m} + V_{\text{ext}}(\mathbf{r},t) + g|\Psi(\mathbf{r},t)|^2 + \int d\mathbf{r}' V_{\text{dd}}(\mathbf{r}-\mathbf{r}')|\Psi(\mathbf{r}',t)|^2 + \gamma(\epsilon_{\text{dd}})|\Psi(\mathbf{r},t)|^3, \tag{4.2}$$

substituting $t \to -i\tau$ leads to the corresponding imaginary-time evolution equation

$$\frac{\partial}{\partial \tau}\Psi = -\hat{H}\Psi. \tag{4.3}$$

This transformation results in damping out of high-energy components of the wavefunction, allowing the system to relax toward its ground state or steady-state solution. The wavefunction evolves into the lowest-energy eigenstate of $\hat{H}$ as $\tau \to \infty$.

This equation is discretized and solved iteratively. Starting from an initial guess Ψ_0, a sequence of iterates $\{\Psi_n\}$ is generated using Euler's method [138], the lowest-order explicit scheme for numerical integration of ordinary differential equations[1]:

$$\Psi_{n+1} = \Psi_n - d\tau \hat{H}_n \Psi_n, \tag{4.4}$$

where $\hat{H}_n$ is the Hamiltonian evaluated at Ψ_n.

Since imaginary-time evolution does not inherently preserve the norm of the wavefunction, it must be renormalized at each iteration step to ensure particle number conservation:

$$\Psi_n \to \sqrt{\frac{N}{\int d\mathbf{r}|\Psi_n|^2}}\Psi_n. \tag{4.5}$$

[1] Higher-order numerical integration schemes could be implemented to improve accuracy, but we find that the basic Euler scheme is sufficient for this purpose.

The optimal choice of the imaginary-time step $d\tau$ depends on system parameters, particularly the spatial grid resolution. We select it as the largest value that maintains numerical stability and avoids divergence. The iteration continues until the desired level of convergence is reached, which can be monitored by tracking the chemical potential at each step:

$$\mu_n = \frac{\langle \Psi_n | \hat{H}_n | \Psi_n \rangle}{\langle \Psi_n | \Psi_n \rangle}. \tag{4.6}$$

A more rigorous convergence criterion can be set by evaluating the norm of the residual:

$$||\hat{H}_n \Psi_n - \mu_n \Psi_n||^2, \tag{4.7}$$

and continuing iterations until if falls below a chosen tolerance threshold. In practice, we typically perform a fixed number of 10^4-10^5 iterations, which provides reliable convergence.

Although imaginary-time evolution theoretically converges to the global ground state in the infinite-time limit, in practice, the system can become trapped in a local energy minimum. To avoid this, the choice of the initial wavefunction is crucial. The initial guess should be selected based on physical intuition about the expected ground state configuration. For example, when searching for the ground state in a rotating reference frames, two separate imaginary-time simulations are performed, one initialized with an imprinted vortex phase and one without. The solution with the lower energy is then identified as the true ground state. Typically, we also introduce a small random noise to the initial wavefunction, which can, in some cases, accelerate convergence.

4.1.2. Energy functional minimization

An alternative approach to ground state calculation is the minimization of the energy functional (3.11). This is done using a gradient descent method, which is an iterative optimization algorithm that minimizes a function by moving in the direction of its steepest descent [138]. The gradient of the energy functional is determined as its functional derivative with respect to Ψ^*, leading to the iterative update rule:

$$\Psi_{n+1} = \Psi_n - \alpha \frac{\delta E[\Psi_n]}{\delta \Psi^*}. \tag{4.8}$$

Here, the negative sign is taken to ensure movement in the direction of decreasing $E[\Psi]$. Evaluating the functional derivative explicitly shows that this equation is equivalent to Eq. (4.4), with the parameter αplaying the role of the imaginary

time step $d\tau$. Here as well, the normalization of the wavefunction needs to be performed after each iteration step.

Alternatively, the normalization condition (3.8) can be included directly into the minimization procedure by introducing the chemical potential μ as a Lagrange multiplier, and minimizing the modified functional:

$$E_{\text{norm}}[\Psi] = E[\Psi] - \mu N, \tag{4.9}$$

where μ is given by Eq. (4.6). This formulation ensures that the wavefunction remains properly normalized throughout the iterative process.

4.1.3. Heavy-ball method

The convergence of the minimization procedure can be significantly improved by employing the heavy-ball method [139, 140]. This is an accelerated gradient-descent technique that introduces a "momentum" term that helps the iteration process move more smoothly and avoid getting stuck in small oscillations. The iteration procedure is modified as

$$\Psi_{n+1} = \Psi_n - \alpha \hat{H}_n \Psi_n + \beta \left(\Psi_n - \Psi_{n-1}\right). \tag{4.10}$$

If the updates remain in the same direction, the additional term increases the step size, and if the descent direction changes, the step size is reduced. In this was the convergence is accelerated, and the oscillations along the wall of the function are damped. This significantly enhances the efficiency of the algorithm. The choice of the parameter β is problem-dependent and typically determined empirically. In our calculations, we find that $\beta = 0.9$ provides a good balance between stability and convergence speed.

4.2. Time evolution

The time evolution of the wavefunction is governed by the extended Gross-Pitaevskii equation (3.6). Starting from the ground state obtained via imaginary-time evolution described in the previous section, the equation is integrated using the fourth-order Runge-Kutta (RK4) method, a widely used explicit scheme for solving ordinary differential equations [138, 141]. RK4 offers significantly higher accuracy than the simple Euler method without requiring higher-order derivatives of the function. It provides a good balance between computational efficiency and precision, making it a standard choice for time-dependent simulations.

For a general initial value problem of the form

$$\frac{dy}{dt} = f(t, y), \quad y(t_0) = y_0, \tag{4.11}$$

where $y(t)$ is the unknown function, $f(t, y)$ is a known function describing its rate of change, and y_0 is the initial condition at time t_0, the goal is to approximate $y(t)$ at discrete time steps. The RK4 method improves accuracy by evaluating $f(t, y)$ multiple times within a single step. It samples the derivative at intermediate points and uses a weighted combination to update the solution.

For a given time step h, the solution at $t_{n+1} = t_n + h$ is computed as

$$y_{n+1} = y_n + \frac{h}{6}\left(k_1 + 2k_2 + 2k_3 + k_4\right), \tag{4.12}$$

where the intermediate slopes are

$$k_1 = f\left(t_n, y_n\right), \tag{4.13}$$

$$k_2 = f\left(t_n + \frac{h}{2}, y_n + \frac{h}{2}k_1\right), \tag{4.14}$$

$$k_3 = f\left(t_n + \frac{h}{2}, y_n + \frac{h}{2}k_2\right), \tag{4.15}$$

$$k_4 = f\left(t_n + h, y_n + hk_3\right). \tag{4.16}$$

To apply RK4 method to the eGPE, the equation is rewritten as

$$\frac{\partial \Psi}{\partial t} = -\frac{i}{\hbar}\hat{H}\Psi, \tag{4.17}$$

identifying $f = -i\hat{H}/\hbar$, with the Hamiltonian given by Eq. (4.2). The initial condition is taken as the wavefunction obtained from imaginary-time evolution.

RK4 achieves a global accumulated error of order $O(h^4)$. We typically use the same time step as in imaginary-time evolution or a slightly smaller one, which provides a good balance between accuracy and computational cost. The stability of the simulation is monitored by checking the conservation of the wavefunction norm, and in specific cases, energy or momentum.

4.3. Treatment of non-local and derivative terms

The Hamiltonian of the Gross-Pitaevskii equation (4.2) includes a non-local term that accounts for the long-range dipole-dipole interaction:

$$\Phi_{\mathrm{dd}}(\mathbf{r}) = \int d\mathbf{r}' V_{\mathrm{dd}}(\mathbf{r} - \mathbf{r}')|\Psi(\mathbf{r}', t)|^2. \tag{4.18}$$

Evaluating this term presents two issues. First, the integral extends over the entire space and must be computed at each time step (or four times per step in the RK4 method), which can be very computationally expensive. Second, the dipole-dipole interaction kernel diverges as $|\mathbf{r} - \mathbf{r}'| \to 0$, making the result highly sensitive to the choice of the discretization grid, and difficult to treat numerically.

To avoid these issues, the interaction term is computed in Fourier space [55]. Using fast Fourier transform (FFT) algorithms, which are efficiently implemented for both CPUs [142] and GPUs [143], this approach significantly reduces computational cost. Applying the convolution theorem, we rewrite the dipolar potential as

$$\widetilde{\Phi}_{\mathrm{dd}}(\mathbf{k}, t) = \widetilde{V}_{\mathrm{dd}}(\mathbf{k}) \times \mathcal{F}\big(|\Psi(\mathbf{r}, t)|^2\big), \tag{4.19}$$

where the tilde sign denotes the three-dimensional spatial Fourier transform. The wavevector $\mathbf{k}$ is defined on a discrete reciprocal grid in momentum space. The Fourier transform of the dipole-dipole potential can be calculated analytically and is given by [55]

$$\widetilde{V}_{\mathrm{dd}}(\mathbf{k}) = \frac{4\pi\hbar^2 a_{\mathrm{dd}}}{3m} \left(3\cos^2\theta - 1\right), \tag{4.20}$$

where θ is the angle between the wavevector $\mathbf{k}$ and the polarization axis z, with $\cos\theta = k_z/|\mathbf{k}|$.

While this approach eliminates the real-space singularity, a subtle issue remains at $\mathbf{k} = 0$, where $\cos\theta$ is not well-defined. Depending on the direction from which zero is approached (along k_x, k_y, or k_z), the term $\cos\theta$ can take values $\{0, -1, 1\}$. A common practice in the literature is to set

$$\cos\theta \xrightarrow{\mathbf{k}\to 0} 0, \tag{4.21}$$

which we also adopt. The zero-momentum component of the dipolar potential corresponds to a constant contribution in real space, effectively shifting the overall energy reference. As long as this choice is applied consistently throughout the simulation, it does not affect qualitative system behavior, introducing only a uniform energy offset.

Similarly, the action of a Laplacian on the wavefunction is evaluated in Fourier space, eliminating the need for finite difference approximations of derivatives. The Fourier transform gives

$$\mathcal{F}\big(\nabla^2\Psi(\mathbf{r}, t)\big) = -\mathbf{k}^2\widetilde{\Psi}(\mathbf{k}, t). \tag{4.22}$$

After evaluating the product, applying the inverse Fourier transform then gives the corresponding contribution to $\hat{H}\Psi$.

The action of all other Hamiltonian terms corresponds to straightforward multiplication in real space. The integral Q_5, which enters the beyond mean-field term $\gamma(\epsilon_{\mathrm{dd}})$, is computed numerically by a quadrature rule. If the scattering length remains constant throughout the simulation, this integral is evaluated only once.

4.3.1. Periodic boundary conditions

The use of Fourier transforms in numerical calculations has both advantages and drawbacks. An inherent consequence of applying a Fourier transform to a finite system is that it assumes periodicity, meaning the system is effectively replicated with a period equal to the system size. While this can be beneficial for studying uniform systems in the thermodynamic limit, it introduces artificial periodic boundary conditions along confined directions. Due to the long-range nature of the dipolar interaction, this leads to unphysical interactions between the system and its periodic replicas.

There are two main approaches to address this issue. The first is to modify the dipole-dipole interaction by introducing a cutoff distance, beyond which the potential is set to zero [144]. However, a drawback of this method is that the Fourier transform of the truncated potential can only be computed analytically when the cutoff is imposed symmetrically, which is primarily useful for fully trapped systems. Asymmetrical cutoffs, where different cutoff distances are applied along different directions, generally result in an integral of $\widetilde{V}_{\mathrm{dd}}$ that is not analytically solvable, except in special cases, such as a cylindrical geometries with dipoles aligned along the cylinder axis [145]. In the general case, to the best of my knowledge, the cutoff method is not applicable.

The second approach, which is adopted in this thesis, is to use a sufficiently large simulation grid. By extending the grid size, the distance between macroscopic dipoles is increased, thereby reducing their interaction with the system. The grid size is increased until the change in energy and chemical potential becomes negligible. This method, however, comes with a computational cost, particularly for fixed-step grids as used in our simulations, where many grid points correspond to regions where the wavefunction is essentially zero. This issue is especially pronounced in elongated trap geometries, where the system is very narrow along the transverse direction perpendicular to the dipole orientation (y-direction in our case) due to magnetostriction. In such cases, a large number of grid points are required to accurately resolve the wavefunction while maintaining a sufficiently large grid. Despite the computational overhead, for systems with periodic boundary conditions along an extended tube, this remains the only feasible solution.

4.4. Elementary excitations

The elementary excitations of the system are studied using the Bogoliubov-de Gennes equations described in Sec. 3.2. This requires solving the eigenvalue problem given by Eqs. (3.16)-(3.18). Modern numerical methods provide efficient solvers for such problems, and in this work, we employ ARPACK-NG routines [146]. Specifically, we use recently developed codes by S. M. Roccuzzo, which implement these routines to study trapped ultracold dipolar Bose gases [136]. Given a set of system parameters, the code computes a predefined number of the lowest-energy excitations and their corresponding quasiparticle wavefunctions.

Here, we consider a more specific scenario: a dipolar superfluid confined in a cylindrical trap of length L, with the external potential of the form

$$V_{\text{ext}}(\mathbf{r}) = \frac{m}{2}\left(\omega_y^2 y^2 + \omega_z^2 z^2\right), \tag{4.23}$$

where the condensate remains unconfined along the x-direction, and periodic boundary conditions are assumed. Due to the translational symmetry along x, the wavevector k_x becomes a good quantum number. As a result, the quasiparticle amplitudes can be factorized as

$$u_n(r) = \frac{1}{\sqrt{L}}\, e^{ik_n x}\, u_{n,k}(y,z). \tag{4.24}$$

This formulation allows us to compute the dispersion relation, that is, the excitation energies corresponding to a given wavevector k_n. In principle, one could solve the full three-dimensional BdG equations, assigning wavevectors to the solutions based on the spatial distribution of eigenstates along the x-axis; however, this would be computationally demanding. Instead, we exploit the factorization in Eq. (4.24) to derive a reduced, effectively two-dimensional form of the BdG equations, by substituting this expression into the ansatz (3.12). This derivation relies also on the fact that the ground-state wavefunction is homogeneous along the x-direction[2]:

$$\psi_0(r) = \phi_0(y,z), \tag{4.25}$$

making this method applicable only in the superfluid phase, while not suitable for the supersolid regime.

An important step in this reduction is the proper handling of non-local integral

[2]Note that here $\phi_0(y,z)$ is not normalized.

terms. Using the convolution theorem, we obtain:

$$\begin{aligned}\Phi_{\rm dd} &= \mathcal{F}^{-1}\Big[\widetilde{V}_{\rm dd}(\mathbf{k}) \times \mathcal{F}\big(\psi_0^2(\mathbf{r})\big)\Big] \\ &= \mathcal{F}^{-1}\Big[\widetilde{V}_{\rm dd}(\mathbf{k}) \times \delta(k_x)\, \mathcal{F}_2\big(\phi_0^2(y,z)\big)\Big] \\ &= \mathcal{F}_2^{-1}\Big[\widetilde{V}_{\rm dd}^{(0)}(k_y,k_z) \times \mathcal{F}_2\big(\phi_0^2(y,z)\big)\Big]. \end{aligned} \tag{4.26}$$

Similarly, the interaction term involving quasiparticle excitations is transformed as:

$$\begin{aligned}\int d\mathbf{r}' V_{\rm dd}(\mathbf{r}-\mathbf{r}')\psi_0(\mathbf{r}')u_n(\mathbf{r}') = \\ &= \mathcal{F}^{-1}\Big[\widetilde{V}_{\rm dd}(\mathbf{k}) \times \mathcal{F}\big(\psi_0(\mathbf{r})u_n(\mathbf{r})\big)\Big] \\ &= \mathcal{F}^{-1}\Big[\widetilde{V}_{\rm dd}(\mathbf{k}) \times \frac{1}{\sqrt{L}}\,\delta(k_n-k_x)\, \mathcal{F}_2\big(\phi_0(y,z)u_{n,k}(y,z)\big)\Big] \\ &= \frac{1}{\sqrt{L}}\, e^{ik_n x}\, \mathcal{F}_2^{-1}\Big[\widetilde{V}_{\rm dd}^{(n)}(k_y,k_z) \times \mathcal{F}_2\big(\phi_0(y,z)u_{n,k}(y,z)\big)\Big]. \end{aligned} \tag{4.27}$$

Here, $\mathcal{F}_2$ denotes the Fourier transform over the y- and z-coordinates, and the two-dimensional Fourier transform of the dipolar potential takes the form

$$\widetilde{V}_{\rm dd}^{(n)}(k_y,k_z) = \frac{4\pi\hbar^2}{m}\, a_{\rm dd}\left(\frac{3k_z^2}{k_n^2+k_y^2+k_z^2}-1\right), \tag{4.28}$$

with $k_0 = 0$.

Using these transformations, we arrive at the following two-dimensional BdG equations:

$$\begin{bmatrix} \hat{H}_2 - \mu + \hat{X}_2 & \hat{X}_2 \\ -\hat{X}_2 & -\left(\hat{H}_2 - \mu + \hat{X}_2\right) \end{bmatrix} \begin{bmatrix} u_{n,k} \\ v_{n,k} \end{bmatrix} = \hbar\omega_n \begin{bmatrix} u_{n,k} \\ v_{n,k} \end{bmatrix}. \tag{4.29}$$

The operators $\hat{H}_2$ and $\hat{X}_2$ are given by

$$\hat{H}_2 = -\frac{\hbar^2}{2m}\left(k_n^2 + \nabla_y^2 + \nabla_z^2\right) + V_{\rm ext} + g\phi_0^2 + \gamma\phi_0^3 + \mathcal{F}_2^{-1}\Big[\widetilde{V}_{\rm dd}^{(0)} \times \mathcal{F}_2\big(\phi_0^2\big)\Big], \tag{4.30}$$

$$\hat{X}_2 f = \left[g\phi_0^2 + \frac{3}{2}\gamma\phi_0^3\right] f + \phi_0\, \mathcal{F}_2^{-1}\Big[\widetilde{V}_{\rm dd}^{(n)} \times \mathcal{F}_2\big(\phi_0 f\big)\Big]. \tag{4.31}$$

The numerical routine is adapted to solve this eigenvalue problem for each positive discrete wavevector k_n in the reciprocal space. This results in a set of excitation frequencies ω_n for each wavevector k_n, thereby constructing the dispersion relation for the dipolar superfluid confined in a cylindrical geometry.

5

Quantized vortices in dipolar supersolids

This chapter explores quantized vortices in dipolar supersolids at the transition between the superfluid and supersolid phase. Quantized vortices are a key hallmark of superfluidity; thus, their observation in the supersolid phase constitutes a crucial probe of the superfluid nature of dipolar supersolids.

The presence of quantized vortices in a supersolid was first discussed in Ref. [33] in the context of a hypothetical supersolid phase of helium. Using a mean-field Gross-Pitaevskii formalism with a repulsive soft-core interaction, it was shown that vortices could be nucleated in the supersolid by an obstacle. The study also suggested that vortices could be robust when crossing back and forth between the superfluid and supersolid phases.

A notable feature pointed out in Ref. [147] is that vortices are both energetically and dynamically more favorable in the supersolid phase than in the superfluid one. The low-density regions surrounding the droplets of the supersolid phase reduce the energetic barrier for a vortex to enter the system and facilitate vortex pinning in the interstitial regions. Even a very slow rotation of the trapping potential can trigger the dynamical instability that drives vortex nucleation. However, the direct detection of vortices in the interstitials is largely inhibited because, even in the absence of vortices, these regions are characterized by a very low density.

Following a brief introduction to quantized vortices, this chapter explores the robustness of vortices across the superfluid-supersolid phase transition. The conservation of angular momentum results in a distinct dynamical behavior, as the angular momentum per particle associated with a vortex differs significantly between the two phases. Exploiting these differences, we propose a dynamical protocol in which a slowly rotating dipolar condensate is quenched from the superfluid

into the supersolid phase. A vortex is nucleated in the supersolid due to the strongly reduced critical angular velocity, and a subsequent quench back allows for straightforward vortex imaging in the superfluid phase. This protocol was successfully employed in experiments, leading to the first detection of quantized vortices in dipolar supersolids [148].

This approach resembles the method used in the pioneering work of Ref. [149], where vortices created in a strongly interacting Fermi gas were imaged by quenching from the BCS to the BEC regime, enhancing their visibility after expansion. In the case of dipolar gases, the procedure is more challenging because the supersolid and superfluid phases are separated by a first-order phase transition rather than a continuous crossover.

This chapter is based on the publication [150], co-authored by A. Recati, S. M. Roccuzzo, L. Santos, and S. Stringari. The content has been adapted to fit the context of this thesis.

5.1. Introduction to quantized vortices

Quantized vortices are one of the fundamental features of superfluids, occurring as a response to rotation [22, 23]. The velocity field in a superfluid is inherently irrotational, as it is related to the gradient of the phase. Consequently, rotation is possible only through the formation of singularities in the order parameter, in form of lines along which the density vanishes and velocity field diverges, known as vortex cores. Moreover, given the single-valuedness of the order parameter, the rotation occurs in discrete units. The circulation of the velocity field around a vortex core is quantized, and the phase undergoes an integer multiple of 2π winding.

The formation and dynamics of quantized vortices have been the subject of intense work in liquid helium, providing an important signature of superfluidity [151]. With the experimental realization of Bose-Einstein condensation in dilute atomic gases of alkali atoms, the interest has extended to these systems, and vortex formation was experimentally achieved in 1999 [152–154]. Recently, in 2022, quantized vortices were observed in a superfluid phase of a dipolar gas, using a magnetostirring technique that directly relies on magnetic interactions [155].

There are several techniques for creating vortices in ultracold gases, including optical phase imprinting, stirring the atomic cloud with a laser, and rotating the trapping potential [22, 23, 156], the latter of which is used throughout this chapter. This method resembles a rotating bucket experiment in helium, where the angular

momentum transfer occurs through the friction with the cylindrical container walls. In ultracold gases, however, the trapping potential needs to be slightly deformed from a perfectly circular shape for the gas to be set into rotation. Vortex nucleation is induced by the dynamic instability of the quadrupole mode, and the critical frequency is given by the relation $\Omega_{\mathrm{VN}} = \omega_q/2$, where ω_q is the frequency of the quadrupole mode in the absence of rotation [157, 158].

Vortices are detected after condensate expansion by observing density holes corresponding to the vortex cores [153]. The angular momentum, which takes quantized values in presence of vortices, can be measured through the lifting of degeneracy of the quadrupole mode [159, 160]. This frequency splitting arises from the breaking of time-reversal symmetry induced by the vortex.

5.2. Quantized vortices in dipolar supersolids

Recent theoretical works have investigated quantized vortices in dipolar supersolids [147, 161], highlighting the similarities and differences compared to the superfluid phase of dipolar gases. While the mechanism for vortex nucleation in a rotating harmonic trap remains the same, many of the vortex properties are significantly influenced by the partial superfluidity of the supersolid state, and by the crystal structure of it's quantum droplets.

As previously mentioned, due to the quantization of rotational motion, there is a critical angular velocity at which a vortex enters the system. This is defined as the angular velocity above which the presence of a vortex becomes energetically favorable, making the energy of the system in the rotating reference frame smaller for the state with a vortex compared to without one [22]. However, a significantly higher angular velocity is required to nucleate a vortex by rotating a harmonic trap, due to the presence of an energy barrier. The former value will be referred to as the *static*, and the latter as the *dynamic* critical angular velocity.

As discussed in Ref. [147], both the static and dynamic critical angular velocities are reduced in the supersolid phase compared to the superfluid phase, making vortices both energetically and dynamically more favorable (see also Fig. 5.2). The low-density regions surrounding the droplets reduce the energy barrier for a vortex to enter the system, by reducing the density depletion at the vortex position. Even a very slow rotation of the trapping potential can then trigger the dynamical instability that drives vortex nucleation.

The angular momentum carried by a vortex corresponds to the jump in the angular momentum of the system at the critical angular velocity. In a fully superfluid

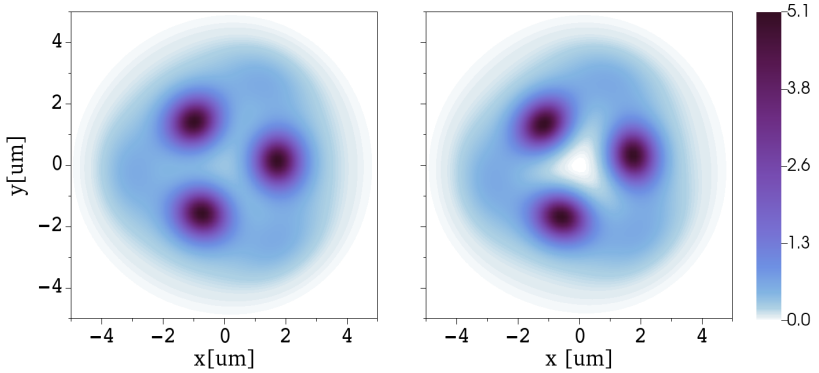

FIG. 5.1.: An illustration of the integrated density distribution for a pancake-shaped dipolar supersolid. The two panels correspond to the same state, rotating with an angular velocity slightly below (left) and slightly above (right) the static critical frequency, showing the ground state without and with a vortex, respectively. In both cases, the central density is significantly lower than the droplet density.

system in an axially symmetric harmonic trap, a single vortex line situated in the center of the trap carries an angular momentum per particle equal to $\hbar$. In a supersolid, this value is reduced due to the reduction in the superfluid fraction of the system.

Instead of forming the well-known Abrikosov lattice[1], vortices are pinned in the low-density regions between droplets, forming a honeycomb lattice that surrounds the triangular lattice of droplets[2]. The supersolid lattice also affect the shape of the vortex core, modifying it from the usual round shape found in superfluids [62]. The size of the vortex core, which is related to the healing length, increases significantly with increasing ϵ_{dd}, becoming several times larger in the supersolid phase compared to the deep superfluid phase (and compared to the non-dipolar case) [147].

Given the outlined factors, the direct detection of quantized vortices is largely inhibited. Even in the absence of vortices, the interstitial region is characterized by a very low density, as shown in Fig. 5.1. The standard method of identifying vortices by associating them with holes in the density distribution after expansion, and even in situ, does not provide a conclusive evidence in this case.

These reasons motivate the present work, where we propose a dynamic protocol for the unambiguous, indirect detection of vortices in the supersolid. Our approach

[1]Multiple quantized vortices typically arrange into an Abrikosov lattice in most superfluid systems. However, recent studies have shown that in a superfluid phase of dipolar gases, quantized vortices instead form a stripe pattern [155].

[2]The honeycomb lattice vanishes at high angular velocities, for which the intervortex distance becomes smaller than the period of the supersolid lattice [147].

involves crossing the phase transition to the superfluid phase, where vortices can be easily detected [155].

5.3. System description

We numerically investigate quantized vortices in dipolar supersolids using the Gross-Pitaevskii formalism outlined in Chapter 3. The system consists of a Bose-Einstein condensate of $N = 4 \times 10^4$ ^{164}Dy atoms, with dipolar length $a_{\mathrm{dd}} = 132a_0$ (a_0 is the Bohr radius), and magnetic moments oriented along the z-axis. Among all isotopes exhibiting supersolidity, ^{164}Dy is particularly advantageous due to its strong dipolar moment, which allows supersolid formation at lower densities. This reduces three-body losses and thereby extends the experimental lifetime of the system.

The gas is confined in an axially symmetric harmonic trap of the form

$$V_{\mathrm{ext}}(\mathbf{r}) = \frac{1}{2} m\omega_{\perp}^2 \left[x^2 + y^2 + \lambda^2 z^2\right], \tag{5.1}$$

with $\omega_{\perp} = 2\pi \times 60\mathrm{Hz}$, and $\lambda = 2$. Stronger confinement along the polarization axis is needed to counteract the effect of magnetostriction. Under these conditions, the superfluid-to-supersolid transition occurs at a scattering length of $a_{\mathrm{crit}} = 94.6\, a_0$, corresponding to $\epsilon_{\mathrm{dd}} = 1.395$.

Ground states of the system are calculated using imaginary time evolution in a rotating reference frame, obtained by adding the angular momentum constraint $-\Omega L_z$ to the eGPE (3.6), where Ω is the angular velocity, and L_z is the z component of the angular momentum operator. Above some critical angular velocity Ω_c, vortical solutions become energetically favorable.

The critical angular velocities for a stable central vortex line across the phase diagram, for the system parameters used in this study, are shown in Fig. 5.2. In the superfluid phase, the critical velocity decreases as the system approaches the phase transition, followed by a discontinuous jump at the transition to the supersolid phase, after which it continues to decrease smoothly. Further increasing ϵ_{dd} would eventually drive the system into the isolated droplet phase, where the critical angular velocity drops to zero [147] (not shown in the figure). It is important to notice that Ω_c is significantly lower than the angular velocity required for dynamical vortex nucleation, which is associated with a quadrupolar instability, as previously discussed [147].

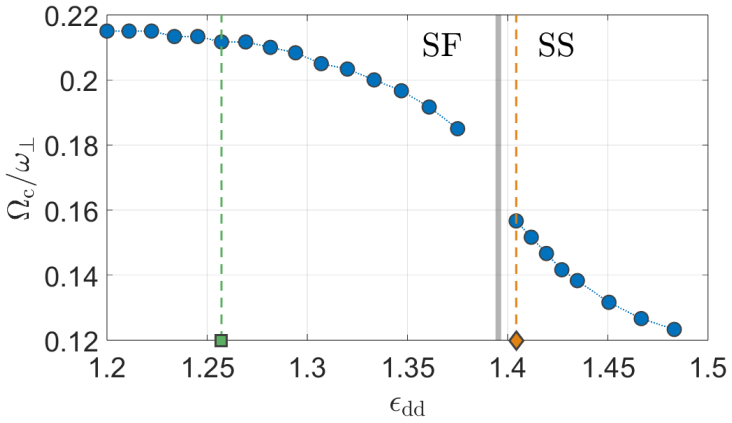

FIG. 5.2.: Critical angular velocities for a stable central vortex as a function of $\epsilon_{\rm dd}$, for a system of 40 000 ^{164}Dy atoms confined in a harmonic trap with $\omega_\perp = 2\pi \times 60$Hz and an aspect ratio $\lambda = 2$. The dotted blue line serves as a guide to the eye, while the thick gray line indicates the phase transition. The critical value $a_{\rm crit}$ increases slightly by increasing Ω; however, this change remains below 0.5% for the angular velocities considered in this study. The green square and orange diamond (with the corresponding dashed lines) mark the superfluid and supersolid states analyzed in this study, respectively.

The obtained ground state is evolved in real time according to the eGPE (3.6). We investigate the behavior of quantized vortices as the system undergoes an adiabatic transition between the superfluid and supersolid phases. The superfluid phase is considered at $a = 105\,a_0 > a_{\rm crit}$, while the supersolid phase is set at $a = 94\,a_0 < a_{\rm crit}$. To ensure an adiabatic transition, the parameter $\epsilon_{\rm dd}$ is varied very slowly in time, by performing a linear ramp of the scattering length in 100ms. Faster quenching protocols would result in the excitation of additional modes and higher final energy.

5.4. Robustness of quantized vortices across the phase transition

Quantized vortices are topological defects of the order parameter and are therefore robust against small perturbations. As long as the system remains in the U(1) broken symmetry phase, quantized vortices cannot be smoothly deformed into a trivial (non-vortex) configuration. This makes them stable features of the system, with small fluctuations only locally modifying the vortex structure or position. Below, we explore the robustness of vortices when crossing the superfluid-supersolid

phase transition in both directions.

5.4.1. Crossing the superfluid-to-supersolid transition

We consider two superfluid ground states, obtained for angular velocities slightly below ($\Omega = 0.21\,\omega_\perp < \Omega_c$) and slightly above ($\Omega = 0.22\,\omega_\perp > \Omega_c$) the critical frequency. They correspond to a vortex-free state, and a state with a vortex in the center, as shown in Figs. 5.3 (a, i) and (b, i), respectively. The associated phase profiles show a uniform phase in the first case, while in the second case, a 0 to 2π phase winding is present around a vortex core. In the superfluid phase, the vortex is characterized by an angular momentum per particle $L_z/N \equiv l_z = \hbar$. The state without a vortex core carries no angular momentum.

Starting from these ground states obtained in the rotating reference frame, the time-dependent simulations are performed in the laboratory reference frame (without trap rotation). The s-wave scattering length is ramped down in 100 ms to a value $a = 94\,a_0$, which corresponds to the supersolid phase at equilibrium. Indeed, once the transition is crossed, a strong density modulation emerges on a very short timescale, leading to the formation of droplets. After a certain waiting time, the system acquires a configuration close to the ground-state shape, with three droplets arranged in a triangular lattice (Fig. 5.3 (iii)).

The vortex-free state remains vortex-free after the phase transition, retaining a mostly flat phase profile and stationary droplets. Although the initial superfluid state was prepared in a reference frame rotating with relatively high angular velocity, there is no angular momentum transfer in the absence of a vortex. Consequently, the resulting supersolid state remains non-rotating, with zero angular momentum. Note that the ramping of the scattering length conserves angular momentum (while it doesn't conserve energy).

The state containing a vortex also retains its vortex after the transition. Despite the occurrence of small oscillations caused by crossing the first-order phase transition, the vortex survives at the trap center, with its characteristic phase pattern. Since the angular momentum per particle carried by the vortex in the supersolid phase is smaller than $\hbar$ due to the reduced global superfluidity, the remaining angular momentum is carried by the droplets, whose centers of mass rotate in the laboratory frame with an angular velocity larger than Ω. It is interesting to notice that in most cases there is a transient regime (see Fig. 5.3 (b, ii)) where the number of density peaks is initially larger (four droplets), before settling into a ground-state-like configuration.

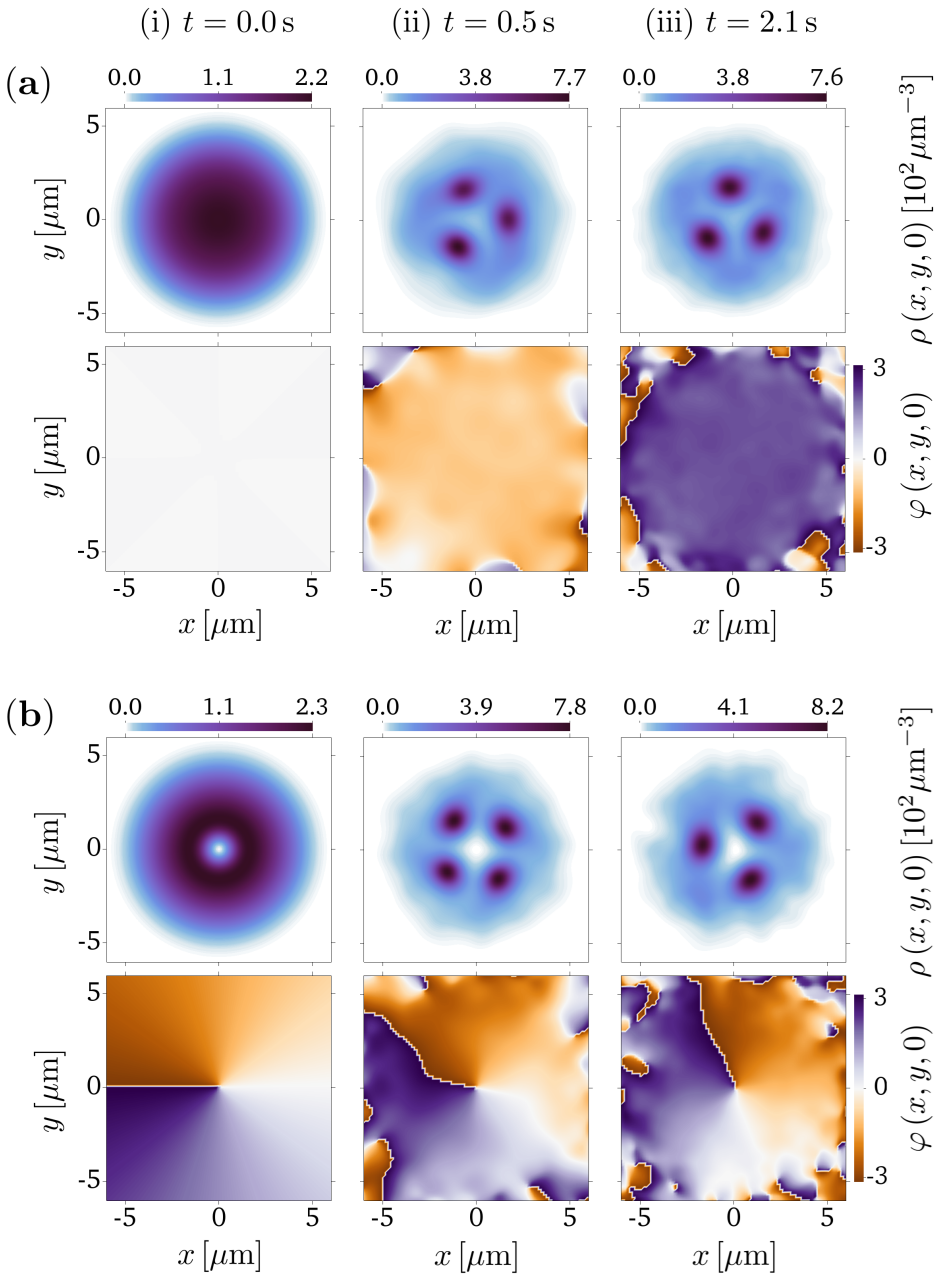

FIG. 5.3.: Density and phase profiles in the $z = 0$ plane through the superfluid-to-supersolid crossing at $t = 0$, 0.5, and 2.1s. The initial ground states are prepared in a superfluid regime ($a = 105\,a_0$) within a rotating reference frame: (a) $\Omega/\omega_\perp = 0.21$, corresponding to a vortex-free state, and (b) $\Omega/\omega_\perp = 0.22$, corresponding to a state with a vortex. The s-wave scattering length a is then linearly ramped in 100ms down to $a = 94\,a_0$, bringing the system into the supersolid phase. The system consists of 40 000 ^{164}Dy atoms confined in a harmonic trap with $\omega_\perp = 2\pi \times 60\mathrm{Hz}$ and $\lambda = 2$.

5.4.2. Crossing the supersolid-to-superfluid transition

The same analysis is performed in the opposite direction in the phase diagram, following the fate of a quantized vortex initially present in the supersolid phase - an especially relevant case for the protocol discussed below. The critical angular velocity Ω_c, for which the vortex becomes energetically favorable, is significantly lower in the supersolid phase than in the superfluid phase. We consider two supersolid ground-state configurations, obtained for $\Omega = 0.15\,\omega_\perp < \Omega_c$ (Fig. 5.4 (a, i)), and for $\Omega = 0.16\,\omega_\perp > \Omega_c$ (Fig. 5.4 (b, i)), corresponding to vortex-free and vortex states. These states are characterized by an angular momentum per particle of (a) $l_z = 0.1\,\hbar$ and (b) $l_z = 0.87\,\hbar$, respectively.

After ramping the scattering length up to $a = 105\,a_0$ over 100ms to reach the superfluid phase, the first state remains vortex-free, while in the second case, the vortex remains clearly visible (Figs. 5.4 (ii) and (iii)). The density profile retains some density modulations, which are the remnants of the original droplets characterizing the supersolid phase.

The conservation of total angular momentum leads to different effects in the two scenarios. In the first case, due to the small initial angular momentum, vortices appear at the surface of the superfluid. In the second case, the vortex in the superfluid phase carries a larger angular momentum ($\hbar$) compared to the initial one, which is compensated by the formation of anti-vortices (with opposite phase winding) near the edge of the atomic cloud. This is also accounted for by the motion of residual density modulations, and, in some cases, by a slight displacement of the vortex core from the center of the trap.

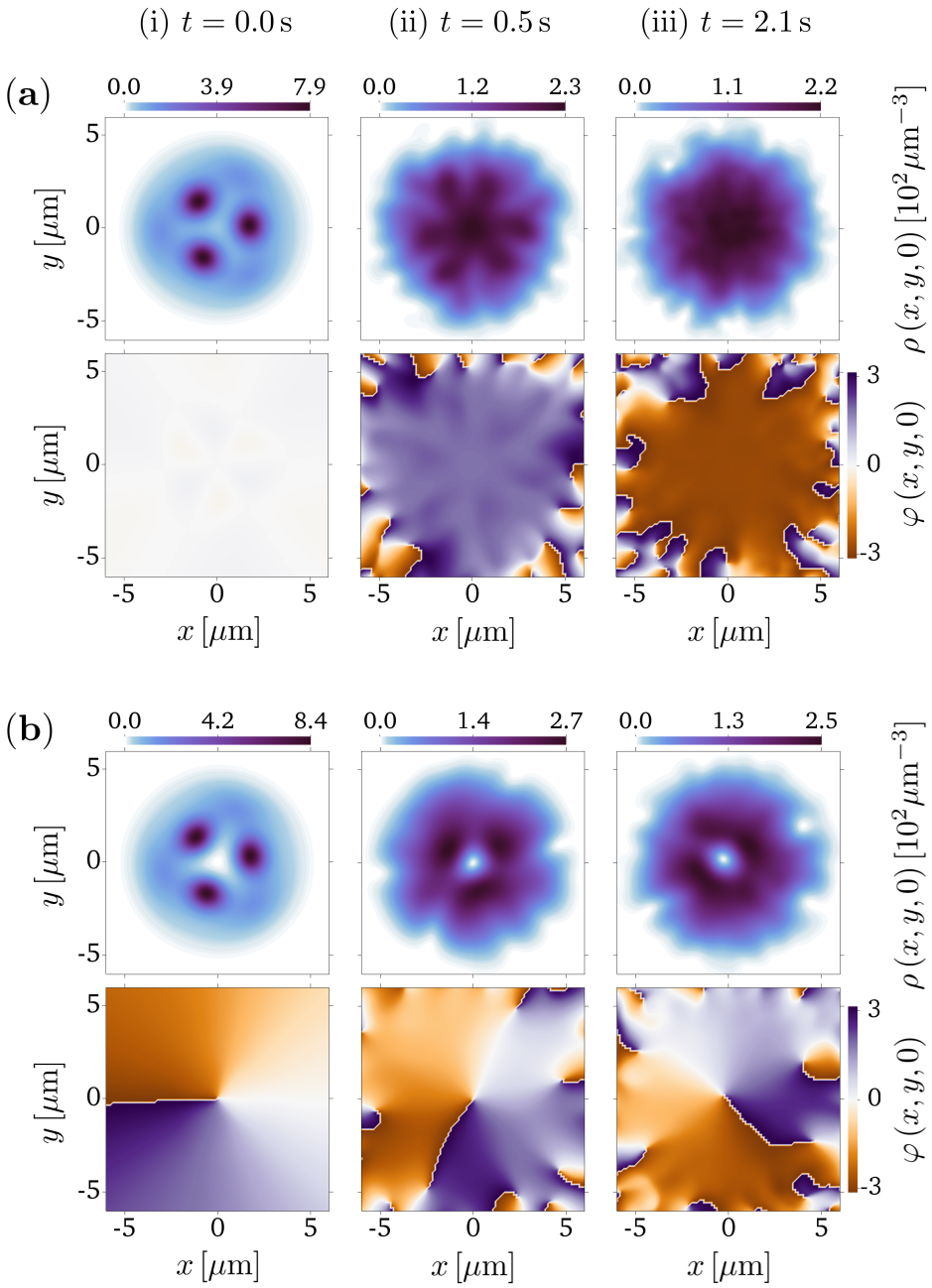

FIG. 5.4.: Density and phase profiles in the $z = 0$ plane through the supersolid-to-superfluid crossing at $t = 0$, 0.5, and 2.1s. The initial ground states are prepared in a supersolid regime ($a = 94\,a_0$) within a rotating reference frame: (a) $\Omega/\omega_\perp = 0.15$, corresponding to a vortex-free state with an angular momentum per particle of $l_z = 0.1\,\hbar$, and (b) $\Omega/\omega_\perp = 0.16$, corresponding to a vortex state with $l_z = 0.87\,\hbar$. The s-wave scattering length a is then linearly ramped in 100ms up to $a = 105\,a_0$, bringing the system into the superfluid phase. The system consists of 40 000 ^{164}Dy atoms confined in a harmonic trap with $\omega_\perp = 2\pi \times 60\mathrm{Hz}$ and an aspect ratio $\lambda = 2$.

5.5. Protocol for vortex nucleation and detection

As demonstrated in the previous section, vortices remain robust when crossing the superfluid-supersolid phase transition in both directions. We exploit this topological robustness to design a protocol that first allows for an alternative mechanism for vortex nucleation in the supersolid phase and, second, for probing their existence by imaging them in the superfluid phase, where they are more easily detectable.

The starting point is a slowly rotating trapped dipolar gas in the superfluid phase ($a = 105\,a_0$). This state is prepared by suddenly introducing rotation to the superfluid ground state in a slightly deformed trap in the xy-plane. This corresponds

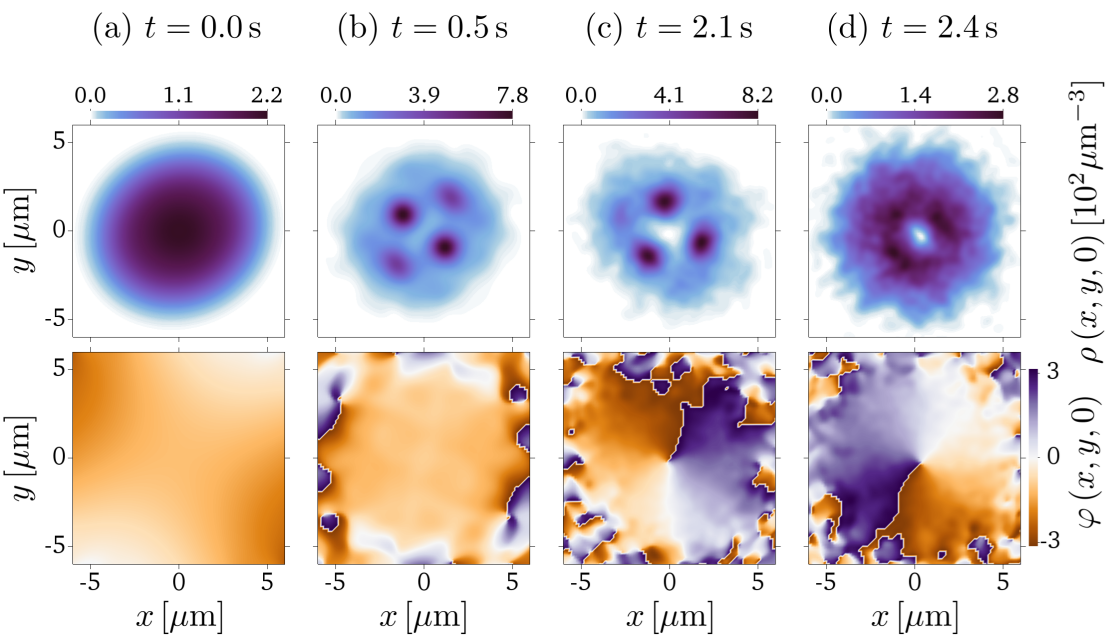

FIG. 5.5.: Density and phase profiles in the $z = 0$ plane, showing vortex nucleation employing the protocol described in the text, for a system of 40 000 ^{164}Dy atoms. (a) Initial vortex-free superfluid state with a scattering length of $a = 105\,a_0$, confined in a slightly deformed harmonic trap (5.2) ($\omega_\perp = 2\pi \times 60\,\mathrm{Hz}$, $\lambda = 2$, $\varepsilon = 6.6\%$), rotating with an angular velocity of $\Omega = 0.3\,\omega_\perp$. (b) The scattering length is linearly ramped in 100ms down to $a_\mathrm{s} = 94\,a_0$, resulting in a transition to the supersolid phase. (c) After some time, a vortex is nucleated at the center of the trap. (d) The isotropy of the trap is restored ($\varepsilon = 0$), and the scattering length is linearly ramped back to its initial value in 100ms, resulting in a superfluid with a readily detectable vortex core.

to a harmonic potential of the form

$$V_{\text{ext}}(t) = \frac{1}{2}m\omega_\perp^2\Big[(1-\varepsilon)\big(x\cos(\Omega t) + y\sin(\Omega t)\big)^2 + (1+\varepsilon)\big(-x\sin(\Omega t) + y\cos(\Omega t)\big)^2 + \lambda^2 z^2\Big], \tag{5.2}$$

where the parameter $\varepsilon = 6.6\%$ is a measure of the trap deformation. The trap rotates with an angular velocity of $\Omega = 0.3\,\omega_\perp$, which is well below the dynamical critical frequency for vortex nucleation, $\Omega_{\text{VN}} = 0.45\,\omega_\perp$[1]. The system is then left to equilibrate for 200ms, obtaining an initial state shown in Fig. 5.5 (a).

This angular velocity is instead large enough for vortex nucleation in the supersolid phase. Therefore, we reduce the value of the scattering length with a linear ramp in 100ms down to $a = 94\,a_0$. Upon entering the supersolid phase, the first droplets are formed (Fig. 5.5 (b)) and after some time, a vortex is nucleated in the center (Fig. 5.5 (c)). It should be noted that the timescale for this process is relatively slow in the present simulation. However, in a real experimental setting, the time scale is expected to be much faster, as a consequence of thermal noise, which is not accounted for in our calculations.

Once the vortex has formed (Fig. 5.5 (c)), the isotropy of the trap is restored ($\varepsilon = 0$), recovering the static external potential 5.1. This step ensures the robustness of the vortex and the conservation of angular momentum. The scattering length is then ramped back to its initial value using the same ramping procedure. After a certain evolution time (Fig. 5.5 (d)), the system reenters the superfluid phase, recovering a configuration very similar to that of Fig. 5.4 (b, iii).

We have verified that if the same procedure is performed with the scattering length reduced only to a value slightly above the phase transition, the system does not nucleate a vortex, as the angular frequency remains insufficient. This confirms that vortex formation is indeed induces by crossing to the supersolid phase.

Recently, the group of Ferlaino experimentally detected quantized vortices in the supersolid phase for the first time, by following the procedure outlined in this section [148]. Their study also demonstrates that a vortex in a supersolid state can be directly observed through time-of-flight interference patterns.

[1] This value remains nearly constant throughout the observed superfluid region.

5.6. Multiple vortex nucleation

The same protocol can be employed to nucleate multiple vortices by increasing the angular velocity Ω of the rotating trap. Figure 5.6 presents the results for different angular velocities in our protocol. The upper panel shows the atomic cloud in the supersolid phase right before inverting the ramping of the scattering length. The lower panel depicts the final density distribution after the scattering length has been restored to its initial value.

The case with $\Omega = 0$ is particularly significant, as it demonstrates that despite the strong density modulation in the supersolid regime, no vortex core emerges upon returning to the superfluid phase. The final density remains smooth and char-

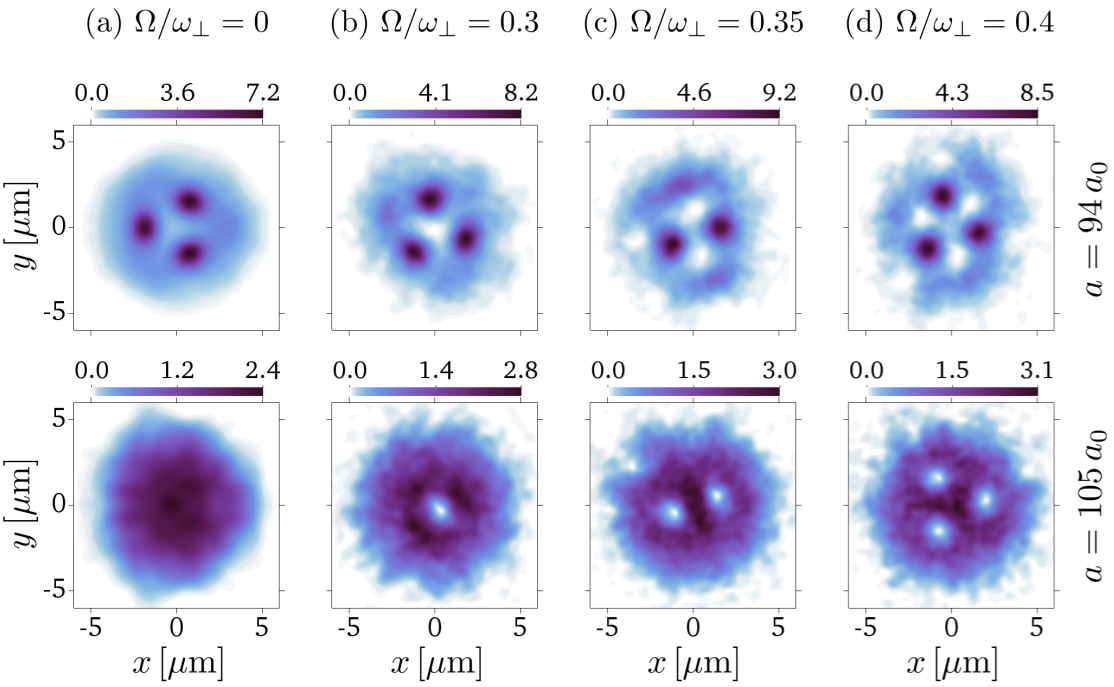

FIG. 5.6.: Density profiles in the $z = 0$ plane, showing the results of the dynamical protocol for different angular velocities: $\Omega/\omega_\perp = 0$ (a), 0.3 (b), 0.35 (c), and 0.4 (d). The parameters and procedure are the same as in Fig. 5.5. The upper row corresponds to the configurations in the supersolid phase at $t = 2.1\,\mathrm{s}$, just before inverting the ramp of the scattering length. The lower row corresponds to final configurations in the superfluid phase at $t = 2.4\,\mathrm{s}$, after ramping the scattering length back to its initial value. Imaging in the superfluid phase should clearly reveal the presence of zero, one, two and three vortices, respectively. The final angular momentum per particle (once the isotropy of the xy trapping is restored) is (a) $l_z = 0$, (b) $l_z = 1.03\,\hbar$, (c) $l_z = 1.85\,\hbar$, and (d) $l_z = 2.42\,\hbar$.

acterized by a maximum in the center, closely resembling the initial equilibrium configuration.

By increasing Ω we eventually observe one vortex nucleated in the center using $\Omega = 0.3\,\omega_\perp$ (same as Figs. 5.5 (c) and (d)), two vortices using $\Omega = 0.35\,\omega_\perp$ and three vortices using $\Omega = 0.4\,\omega_\perp$. Note that in all cases the vortices are nucleated in the supersolid phase, as the angular velocity is not large enough for vortex formation in the superfluid.

6

Sound in ring dipolar supersolids

According to the Goldstone theorem, the spontaneous breaking of a global continuous symmetry gives rise to a gapless excitation mode in the spectrum. These Goldstone modes are of central interest in various fields of physics, including elementary particle physics, magnetism, superfluidity, and superconductivity. Their identification and experimental observation are essential, as they characterize collective excitations associated with broken symmetries.

The recent realization of supersolidity has raised the question of identifying the corresponding Goldstone modes. In three-dimensional supersolids, four gapless modes emerge: one associated with phase symmetry breaking and three corresponding to the breaking of translational invariance along the three spatial directions [125]. They take the form of a phononic dispersion relation in the long-wavelength limit, with characteristic speeds of sound.

The theoretical study of Goldstone modes in supersolids dates back to the pioneering work of Andreev and Lifshitz [4], which, using a hydrodynamic approach, predicted four phononic excitation modes. There are many subsequent works extending this description and exploring additional effects [34, 126–130]. More recently, the studies employing numerical simulations explored Goldstone modes in various supersolid platforms, including atomic Bose gases with soft-core interactions [109, 162, 163], spin orbit coupled gases [164, 165], multimode cavity systems [166], and dipolar gases [15, 56].

Experimentally, the first evidence of Goldstone modes in a supersolid phase was recently reported in dipolar Bose-Einstein condensates confined in harmonic traps [59–61]. These experiments revealed the emergence of novel crystal-like oscillations upon entering the supersolid regime. However, due to the presence of the external trapping potential, the modes take the form of discretized oscillations rather than continuous excitations. Additionally, the trap imposes the inhomogeneous density

distribution of the gas, and restrict the system to a finite, small number of droplets that constitute the supersolid. These constraints limit the direct observation of bulk supersolid dynamics and the full characterization of collective excitations.

To overcome these limitations, it is essential to study supersolids in a homogeneous setting and in the thermodynamic limit. Numerically, the speeds of sound in such configurations have been the object of study for both soft-core [109, 162] and dipolar gases [56, 167], based on the use of proper periodic boundary conditions. Experimentally, however, reaching the thermodynamic limit in a dipolar gas remains challenging. Standard box potentials, which are commonly used to achieve homogeneous ultracold gases, lead to strong dipole accumulation at the boundaries, introducing edge effects [168, 169].

In this study, we employ a tubular potential with periodic boundary conditions, which, for a sufficiently long tube, allows to approach the thermodynamic limit. This effectively corresponds to a ring-shaped potential, which has been explored theoretically in the context of dipolar supersolids with persistent currents [170] and has recently started to be employed experimentally [122]. Additionally, ring geometry provides a simple platform for realizing of matter-wave circuits, with important perspectives in the emerging field of atomtronics [19, 171]. The results obtained in the tubular geometry are compared with those from a ring geometry, and only minor differences are found, which can be contributed to the curvature effects.

To investigate the longitudinal Goldstone modes, we excite them by suddenly removing a periodic perturbation along the longitudinal direction. The resulting values of the sound velocities are analyzed using the hydrodynamic theory of supersolids, which provides valuable new insights into the origin of the two sound modes. In particular, using the sound velocities obtained from our simulations, we determine for the first time the layer compressibility modulus and confirm the prediction for the superfluid fraction of a dipolar supersolid based on the Leggett's estimation [117].

The content of this chapter is based on the publication [172], co-authored by T. Zawiślak, A. Recati, and S. Stringari, and has been adapted to fit the context of this thesis.

6.1. The system and its phases

For simplicity, we consider a one-dimensional supersolid configuration, where two phononic Goldstone modes are expected, each associated with a distinct sound

velocity. The system is confined in a tubular potential, with harmonic confinement in two transverse directions (denoted as y and z), while the third direction (x) remains unconfined and is subject to periodic boundary conditions. The external potential is given by:

$$V_{\text{ext}} = \frac{1}{2} m\omega_{\perp}(y^2 + z^2), \tag{6.1}$$

where the transverse trapping frequency is set to $\omega_{\perp} = 2\pi \times 100\text{Hz}$. The tube has a length of $L = 48\mu\text{m}$ along the x-axis, which corresponds to a ring of radius $R = 7.6\mu\text{m}$. Although this system is not large enough to fully reach the thermodynamic limit, and some finite-size effects are present, the chosen parameters are both experimentally realistic and well-suited for observing the effects of interest.

The system consists of $N = 80.000$ atoms of ^{164}Dy, with a dipolar length of $a_{\text{dd}} = 132a_0$, where the dipoles are oriented along the z-axis. Depending on the value of the scattering length, the system can exist in one of three phases: superfluid, supersolid, or isolated droplet phase, with the corresponding density profiles shown in Fig. 6.1. The superfluid-to-supersolid transition occurs at a scattering length of $a = 95.2\,a_0$ ($\epsilon_{\text{dd}} = 1.987$), while the supersolid-to-droplet phase transition takes place at approximately $a = 84\,a_0$ ($\epsilon_{\text{dd}} = 1.571$).

These states are obtained through imaginary-time evolution of the extended Gross-Pitaevskii equation (3.6). In our simulations, we consider configurations with the same number of density peaks (equal to 13) in both the supersolid and crystal phases. In principle, exact energy minimization would predict a gradual decrease in the number of droplets as the system approaches the transition to the crystal phase, leading to small discontinuities in the resulting values of the observed quantities. However, this constraint does not affect the main conclusions of this study. The pinning of the number (and position) of the droplets can be achieved by introducing a weak additional periodic potential during the initial stage of the supersolid state preparation. Once this potential is removed, the number of droplets remains unchanged throughout the subsequent time evolution.

6.2. The protocol for sound excitation

The system is initially prepared in a stationary state in the presence of a weak static perturbation of the form

$$V_{\text{pert}} = -V_0 \cos(qx), \tag{6.2}$$

where $q = 2\pi/L$ is the smallest characteristic wavevector of the system, inducing stationary density modulations. At $t = 0$, we suddenly set $V_0 = 0$, resulting in

the excitation of longitudinal phonon modes propagating along the x-axis. In a ring geometry, this perturbation takes the form $V_{\text{pert}} = -V_0 \cos(\varphi)$, where φ is the azimuthal angle along the ring. Similar excitation protocols have been previously employed to study the Doppler effect caused by the presence of quantized vortices in a ring [173] and, more recently, to investigate the effect of superfluidity on sound propagation in a dilute Bose gas confined in a box in the presence of an external periodic potential [121].

Within linear response theory, the time evolution of the quantity

$$F(t) = \langle \cos(qx) \rangle(t) \tag{6.3}$$

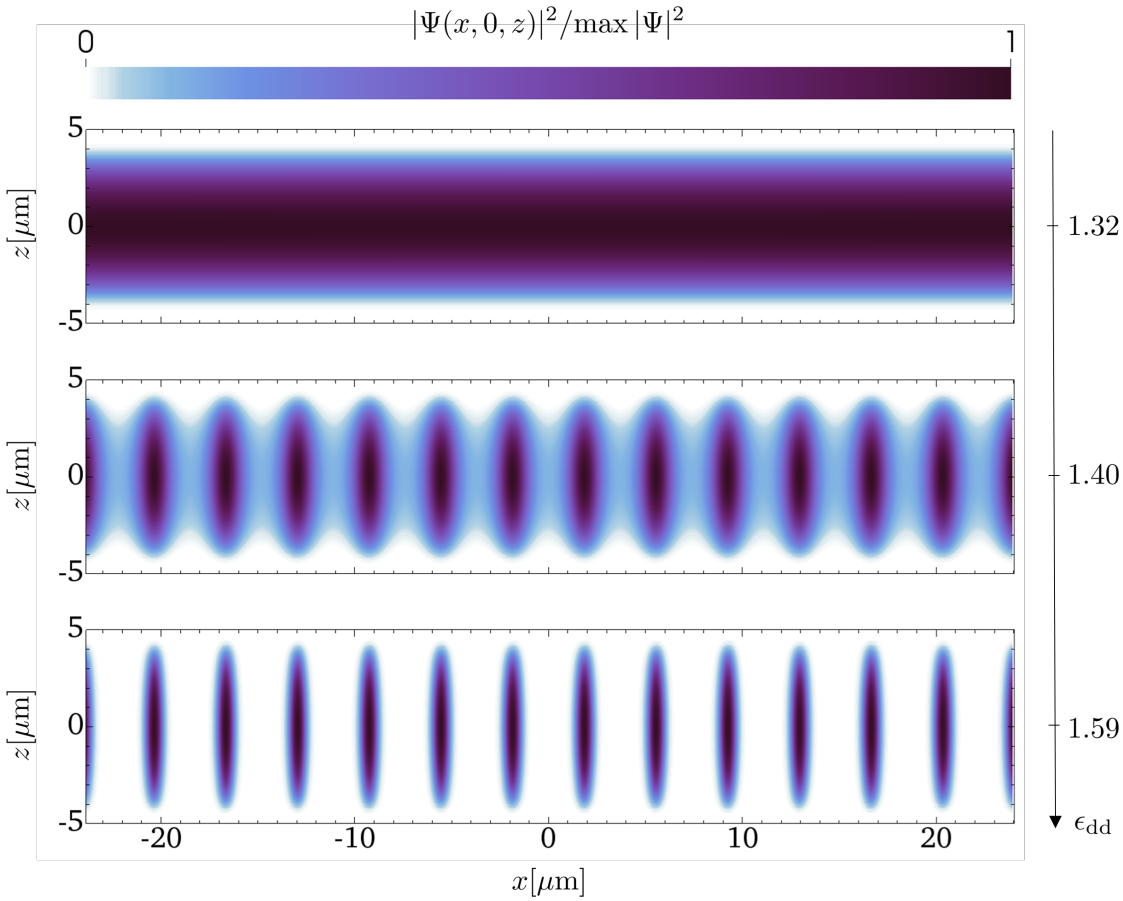

FIG. 6.1.: Density profiles in the $y = 0$ plane for the superfluid (top panel), supersolid (middle panel), and isolated droplet (bottom panel) phases. The system consists of $N = 80.000$ ^{164}Dy atoms confined in a tubular potential, with a transverse trapping frequency of $\omega_\perp = 2\pi \times 100$Hz along the y and z directions, while the x-direction remains unconfined. Periodic boundary conditions are applied at $x = \pm 24\mu$m. The colormap represents the densities relative to their maximum value.

reveals the modes excited by the perturbation. In the superfluid phase, $F(t)$ exhibits a single-frequency oscillation, whereas in the supersolid phase, it shows a characteristic beating pattern due to the presence of two distinct modes, as presented in Fig. 6.2.

In the supersolid phase, the function $F(t)$ can be expressed as

$$F(t) = V_0 \sum_{i=1,2} \chi_i(q) \cos\left(\omega_i(q)t\right), \tag{6.4}$$

while in the superfluid phase, this reduces to a single-mode contribution. For sufficiently small q (and hence large L), the mode frequencies $\omega_i(q)$ approach a linear phonon dispersion relation,

$$\omega_i(q) \simeq c_i q, \tag{6.5}$$

where c_1 and c_2 denote the first and second sound velocities, respectively. The coefficients $\chi_i(q)$ represent the contributions of the two modes to the static response function,

$$\chi(q) = \chi_1(q) + \chi_2(q). \tag{6.6}$$

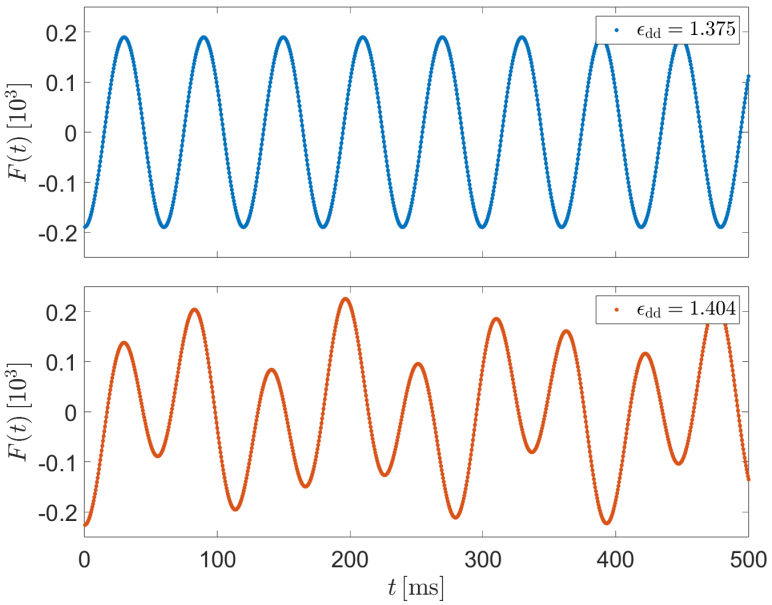

FIG. 6.2.: Time evolution of the parameter $F(t) = \langle \cos(2\pi x/L)\rangle(t)$ for two values of ϵ_{dd} corresponding to the superfluid phase (top panel) and the supersolid phase (bottom panel). The data points are fitted with a single cosine function in the superfluid phase and a superposition of two cosine functions in the supersolid phase, showing excellent agreement.

Thus, from the analysis of the measurable signal $F(t)$, one can extract the sound velocities c_1 and c_2, and the weights of the two modes χ_1 and χ_2.

According to the compressibility sum rule, the static response function approaches the compressibility of the system in the long-wavelength limit $q \to 0$:

$$\chi(q) = \int_0^\infty d\omega \, \frac{S(q,\omega)}{\omega} \underset{q\to 0}{=} \frac{N\kappa}{2}. \tag{6.7}$$

Here, $S(q,\omega)$ is the dynamic structure factor, and the compressibility is given by

$$\kappa = \frac{1}{\bar{\rho}} \left(\frac{\partial \mu}{\partial \bar{\rho}} \right)^{-1}, \tag{6.8}$$

where μ is the chemical potential, and $\bar{\rho} = N/L$ is the linear density. The compressibility is related to the speed of sound in uniform systems as $c_\kappa = \sqrt{\kappa^{-1}}$, where we set $m = 1$ with m the atomic mass.

Due to the finite size of the tube, the smallest accessible value of the wavevector is $q = 2\pi/L$, leading to deviations between the obtained static response function $\chi(q)$ and the compressibility κ. In our system, these finite size effects result in discrepancies of approximately 15% in the superfluid phase and up to 30% near the transition to the crystal phase. For consistency, we use the values of κ given by the "measured" values $\chi(q = 2\pi/L)$.

Another useful quantity to consider is the relative contribution of the second sound mode to the compressibility sum rule, which can be expressed in terms of the sound velocities in the following way:

$$R \equiv \frac{\chi_2}{\chi} = \frac{c_1^2 - c_\kappa^2}{c_1^2 - c_2^2}. \tag{6.9}$$

This follows from the compressibility sum rule 6.7 and the f-sum rule,

$$m_1 = \int_0^\infty d\omega \, S(q,\omega)\, \omega = \frac{Nq^2}{2}. \tag{6.10}$$

This quantity is particularly useful in experiments since it can be determined without precise knowledge of the perturbation strength V_0, which is often difficult to estimate accurately. Instead, it only requires the relative weights of the beating signal. However, the Eq. (6.9) is based on a two-mode approximation, which holds in most of the supersolid regime but becomes less accurate near the transition to the superfluid phase, where additional modes are excited by the perturbation.

Analogously, the contribution of second sound mode to the f-sum rule is given by

$$\frac{m_1^{(2)}}{m_1} = \frac{c_2^2}{c_\kappa^2} \frac{c_1^2 - c_\kappa^2}{c_1^2 - c_2^2}. \tag{6.11}$$

6.3. Hydrodynamic predictions

The central conclusion of this work lies in the combined application of the excitation protocol and the hydrodynamic theory of supersolids. The hydrodynamic model introduced in Section 3.4 predicts the following expression for the two sound velocities, reprinted here for completeness:

$$c_{1,2}^2 = \frac{c_\kappa^2}{2}\left(1+\beta\kappa \pm \sqrt{(1+\beta\kappa)^2 - 4f_s\beta\kappa}\right). \tag{6.12}$$

This expression depends on three fundamental parameters: the velocity c_κ, determined by the compressibility parameter κ; the renormalized layer compressibility modulus $\beta = B/\rho_n$; and the superfluid fraction f_S. Depending on the phase of the dipolar Bose gas, the sound velocities take different forms, as discussed below.

(i) Superfluid phase ($f_S = 1$ and $\beta = 0$).

Only the upper solution (first sound) of Eq. (6.12) is present, and the sound velocity is simply given by

$$c_1 = c_\kappa, \tag{6.13}$$

as expected for a uniform superfluid at zero temperature.

(ii) Supersolid phase ($0 < f_s < 1$ and $\beta \neq 0$).

This is the most interesting regime, where the deviations of the sound speeds from c_κ arise due to the presence of both the superfluid and crystalline components. The sound velocities are influenced by the dimensionless parameter $\beta\kappa$ and the superfluid fraction f_S. Near the transition to the crystal phase, where the superfluid fraction is expected to vanish, the sound velocities approach the limiting values:

$$\begin{aligned} c_1 &\xrightarrow{f_s\to 0} \sqrt{1+\beta\kappa - \frac{f_S\beta\kappa}{1+\beta\kappa}}c_\kappa, \\ c_2 &\xrightarrow{f_s\to 0} \sqrt{f_S\frac{\beta\kappa}{1+\beta\kappa}}c_\kappa, \end{aligned} \tag{6.14}$$

while the ratio R given by Eq. (6.9) approaches the value

$$R \xrightarrow{f_s\to 0} \frac{\beta\kappa}{1+\beta\kappa}. \tag{6.15}$$

Additionally, and interesting limiting case arises when $\beta\kappa \gg 1$, where the lower sound velocity simplifies to

$$c_2 = c_\kappa\sqrt{f_S}. \tag{6.16}$$

In this regime, the second sound mode exhausts the compressibility sum rule, while its relative contribution to the f-sum rule (Eq. (6.11)) exactly matches the superfluid fraction f_S. This behavior is analogous to that of a superfluid in the presence of an optical lattice, where translational invariance is explicitly broken and the upper mode $\omega_1 = c_1 q$ is replaced by a gapped excitation. This case has been recently explored both theoretically and experimentally in [121].

(iii) Crystal phase ($f_s = 0$ and $\beta \neq 0$).

In this regime, only the first sound mode remains, with a velocity given by

$$c_1 = c_\kappa \sqrt{1 + \beta\kappa}. \tag{6.17}$$

This is consistent with the fact that the isolated droplet phase breaks only one continuous (translational) symmetry. However, unlike in the superfluid phase, where a single sound mode exhausts both the compressibility and f-sum rules, in the crystal phase, the first sound mode exhausts only the f-sum rule. It does not exhaust the compressibility sum rule, which reveals the occurrence of a diffusive mode at zero frequency. This diffusive mode is the natural continuation of the second sound mode beyond the transition to the crystal phase [127, 174].

The transformation of second sound from a propagating to a diffusive mode is analogous to the fate of second sound in a uniform superfluid above its critical temperature, where it becomes a thermal diffusive mode (see, e.g., [175, 176]), hence the name analogy.

6.4. Sound velocities from the excitation protocol

From the analysis of the signal $F(t)$ for different values of ϵ_{dd}, we obtain the first and second sound velocities across the phase diagram, as shown on Fig. 6.3 (blue diamonds and green squares). Both sound velocities exhibit a discontinuity at the supersolid-superfluid phase transition, with the second sound showing a more pronounced jump. As the system approaches the isolated droplet phase, the second sound velocity c_2, which can be associated with oscillations of the superfluid component, gradually decreases and eventually vanishes, coinciding with the loss of global superfluidity. In contrast, the first sound velocity c_1, which can be associated with the crystalline oscillations, increases before saturating, and remains the only mode in the droplet phase.

The saturation of c_1 is a consequence of the number of droplets in the system being fixed. Otherwise, as the droplets move farther apart (i.e. their number decreases

in the case of a finite system), the first sound mode would also gradually decrease toward the droplet phase (while remaining finite). It is important to note that the two sound modes cannot be strictly classified as superfluid or crystal sound, as they result from a hybridized contribution of both components, particularly near the supersolid-superfluid phase transition.

Figure 6.3 also shows the value of c_κ throughout the phase diagram, obtained from the static response function χ (orange dots). In the superfluid phase, c_κ coincides with the single sound velocity, while in the supersolid phase, it does not match either of the two sounds. Near the transition to the superfluid phase, c_κ matches the value of c_1, also resulting in $R \to 0$.

These trends are consistent with the results reported in [167] obtained for an infinite tube, confirming that our mesoscopic system correctly captures the behavior

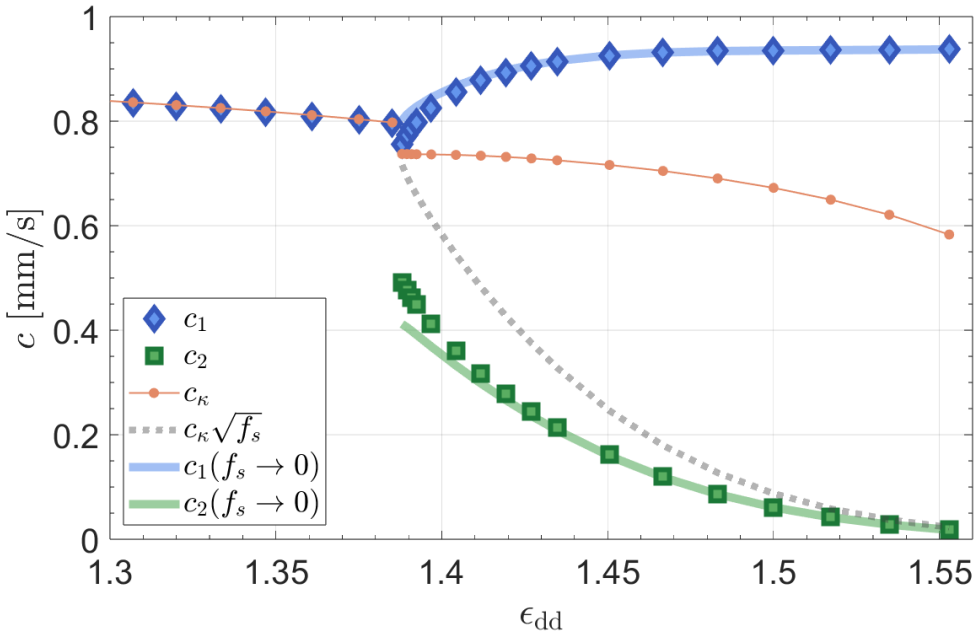

FIG. 6.3.: Sound velocities c_1 and c_2, extracted from the excitation protocol described in Sec. 6.2 (blue diamonds and green squares, respectively), across the superfluid and supersolid phases for the system described in Sec. 6.1. The orange dots represent the velocity c_κ fixed by the compressibility κ, which is obtained from the static response function $\chi(2\pi/L)$. The limiting expressions for the sound velocities, given in Eq. (6.14) (blue and green thick solid lines), accurately capture the behavior of c_1 and c_2 even far from the crystal phase. For comparison, the prediction $c_\kappa\sqrt{fs}$ (gray dotted line), which is valid for a Bose gas in an optical lattice, $c_\kappa\sqrt{fs}$, shows poor agreement.

expected in the thermodynamic limit.

We include also the lowest-order expressions for the two sound speeds in the limit $f_s \to 0$, given by Eq. (6.14) (blue and green continuous lines). These approximations show good agreement with the calculated values over a broad range of ϵ_{dd}, even when the superfluid fraction is not negligible.

For comparison, we also show the prediction $c_2 = c_\kappa \sqrt{f_S}$ (gray dotted line), which would hold in the presence of an optical lattice ($B \to \infty$). This expression significantly overestimates the the actual values of c_2 in the supersolid phase. While this relation has been successfully used to extract the value of f_S in a BEC gas in an optical lattice [121, 177], it does not apply to the supersolid phase.

6.5. Superfluid fraction and layer compressibility

From Eq. (6.12), the superfluid fraction f_s can be directly related to the first and second sound velocities through

$$f_s = \frac{c_1^2 c_2^2}{c_\kappa^2 (c_1^2 + c_2^2 - c_\kappa^2)}. \tag{6.18}$$

The resulting values, shown as purple dots in Fig. 6.4, show a smooth transition from the value close to 1 in the superfluid phase, to vanishing values approaching the droplet phase.

Both the superfluid fraction and the layer compressibility modulus can, in principle, be calculated from the Gross-Pitaevskii theory (see, e.g., [34]). Several numerical studies have investigated the superfluid fraction in dipolar gases with one-dimensional periodic structures using the extended Gross-Pitaevskii equation (e.g., [56, 102, 167]). In our narrow tube geometry, the superfluid fraction essentially coincides with the non-classical fraction of the moment of inertia, which was found to be in strong agreement with the Leggett upper bound in an infinite tube [102]. For comparison with the values extracted from our protocol, the Leggett upper bound is shown as a gray line in Fig. 6.4. The close agreement between these two predictions demonstrates the consistency of the extended Gross-Pitaevskii theory with the hydrodynamic model of supersolidity.

To assess the applicability of our approach in experiments, we tested the sensitivity of the superfluid fraction to finite-size effects by using a larger value of the phonon wave vector for perturbation, $q = 4\pi/L$ instead of $2\pi/L$. The superfluid fraction was found to be very weakly affected, with only a few percent change. Additionally, since this modification nearly doubles the oscillation frequency, it also enables

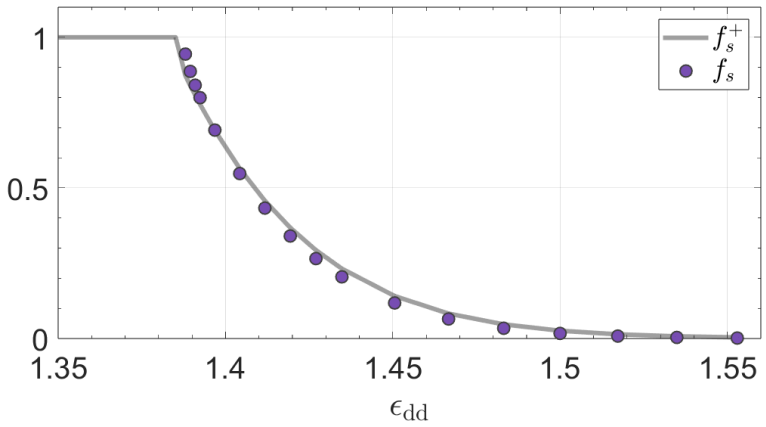

FIG. 6.4.: Superfluid fraction, obtained by applying the hydrodynamic model to the results of the extended Gross-Pitaevskii simulation employing our protocol (Eq. (6.18)), is shown as purple dots. The theoretical prediction for the Leggett upper bound (Eq. (3.24)), calculated from the ground-state density distributions, is represented by gray solid line. The two predictions show close agreement.

shorter observation timescales, thereby reducing the impact of the finite lifetime of the system.

Notably, the superfluid fraction has only recently been assessed experimentally, using a different approach based on the Josephson effect [122].

Similarly, the dimensionless parameter $\beta\kappa$ can be expressed in terms of the extracted sound velocities as follows:

$$\beta\kappa = \frac{c_1^2 + c_2^2}{c_\kappa^2} - 1. \tag{6.19}$$

from this calculation are presented in Fig. 6.5 (a), together with the ratio R, obtained from the analysis of the signal $F(t)$. An interesting observation from our analysis is that while the sound velocities, compressibility, and the parameter $\beta\kappa$ exhibit a jump at the superfluid-supersolid transition, the contribution of the second sound mode to the compressibility sum rule, R, smoothly approaches zero. A similar continuous vanishing is observed for the layer compressibility modulus B, as shown in Fig 6.5 (b). This behavior of B was confirmed in subsequent Gross-Pitaevskii calculations in the ground state of a dipolar gas [134].

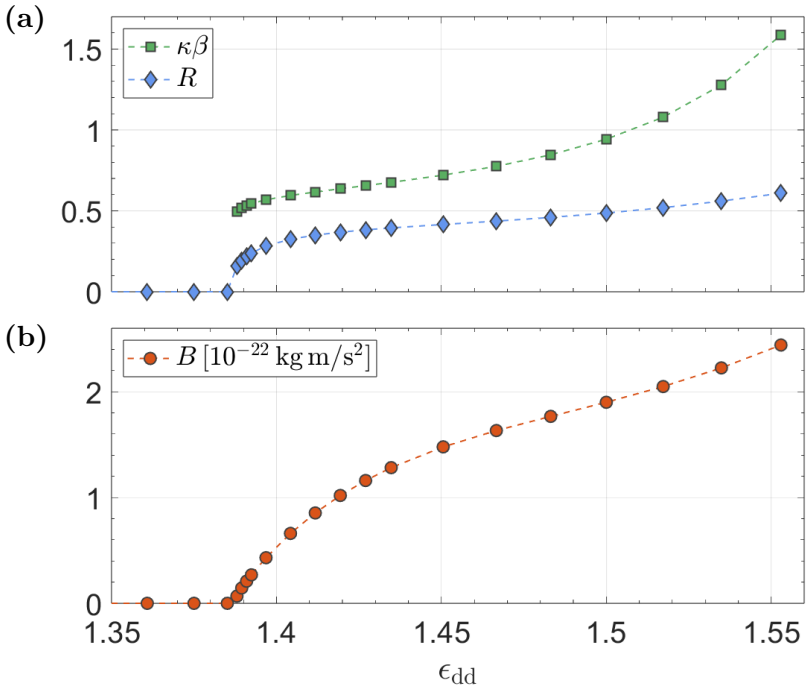

FIG. 6.5.: (a) The dimensionless parameter $\beta\kappa$ (green squares), derived from the extracted sound velocities (Eq. (6.19)), and the ratio $R = \chi_2/\chi$ (blue diamonds), obtained from the analysis of the signal $F(t)$ (Eq. (6.4)). (b) Layer compressibility modulus $B = \beta\rho_n$, calculated from the parameter $\beta\kappa$.

6.6. Excitation spectrum

An additional advantage of the proposed protocol is the possibility to excite modes with larger wavevectors q, beyond the long-wavelength phononic mode. This is achieved by applying a perturbation of the form

$$V_{\mathrm{pert}} = -V_0 \cos(nqx), \tag{6.20}$$

with $q = 2\pi/L$ and $n = 1, 2, 3, \ldots$. In this way, the entire phonon-maxon-roton dispersion relation can be obtained, as shown in Fig. 6.6. The results correctly show that the roton minimum becomes more pronounced as the system approaches the transition to the supersolid phase.

The dispersion relation obtained using our protocol is compared with the predictions of the Bogoliubov–de Gennes theory introduced in Sec. 3.2), showing excellent agreement across all values of ϵ_{dd} considered. This demonstrates that the proposed protocol provides a feasible alternative for measuring the excitation

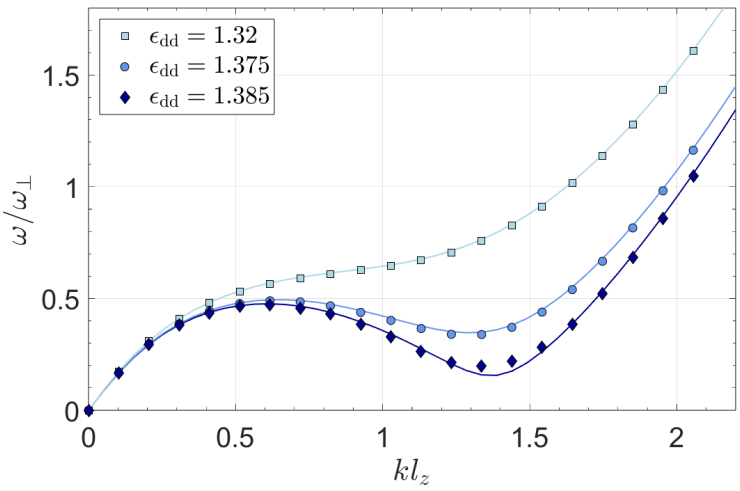

FIG. 6.6.: Excitation spectrum obtained using the proposed protocol for three values of ϵ_{dd} approaching the superfluid-supersolid transition (points), revealing the phonon-maxon-roton dispersion. The roton mode softens near $k = \sqrt{2}/l_z$, where $l_z = \sqrt{\hbar}/m\omega_\perp$ is the characteristic transverse harmonic oscillator length, consistent with [84]. These results are compared with the predictions of the Bogoliubov–de Gennes calculations (solid lines), showing excellent agreement.

spectrum in elongated configurations of superfluid dipolar gases, complementing standard Bragg spectroscopy experiments [91].

7

Conclusions

This thesis has investigated the fundamental properties of dipolar supersolids, with a particular focus on two key aspects: quantized vortices (Chapter 5) and the propagation of sound modes (Chapter 6). These two studies contribute to a deeper understanding of the unique quantum properties of dipolar supersolids.

In Chapter 5, we studied quantized vortices in dipolar condensates and their stability across the superfluid-to-supersolid phase transition. As a key signature of superfluidity, the existence of quantized vortices provides crucial insight into the superfluid nature of dipolar supersolids. Through numerical simulations, we demonstrated that vortices remain robust through the transition in both directions, with angular momentum conservation leading to either droplet rotation or antivortex formation, compensating for the reduced vortex angular momentum in the supersolid phase.

We further proposed an experimentally feasible protocol for controlled vortex nucleation and detection. This method relies on ramping the scattering length across the superfluid-to-supersolid transition, exploiting the intrinsic properties of the supersolid phase to induce vortex nucleation. Starting from a slowly rotating, vortex-free superfluid, entering the supersolid phase induces vortex nucleation, while ramping back into the superfluid allows for direct vortex imaging. The larger vortex size in dipolar condensates further enhances their visibility. This method also enables the controlled creation of multiple vortex configurations. Our approach was recently employed in experiments for the first detection of quantized vortices in dipolar supersolids, reinforcing its feasibility.

In Chapter 6, we investigated sound propagation in a dipolar supersolid confined in a tube geometry with periodic boundary conditions, which is equivalent to a ring geometry. A key feature of supersolids in this one-dimensional configuration is the emergence of two gapless Goldstone modes: one associated with the breaking of phase invariance, leading to superfluidity, and the other with the breaking of

translational symmetry, giving rise to crystalline order. By combining numerical simulations based on the extended Gross-Pitaevskii theory with the hydrodynamic theory of supersolids, we analyzed these excitation branches.

We proposed an experimentally feasible protocol to determine these Goldstone modes by applying a weak periodic perturbation and observing the resulting response of the system in time. Using the results of our simulations alongside supersolid hydrodynamics, we outlined a method to extract key hydrodynamic parameters. In particular, we demonstrated how sound velocity measurements can provide direct access to the superfluid fraction and layer compressibility modulus. Our mesoscopic setup accurately captures the essential features of the thermodynamic limit. Alternatively, our findings can be used to determine supersolid hydrodynamic parameters in the thermodynamic limit by using existing estimations of sound speeds in infinite systems [56, 167].

It is worth noticing that our protocol is not limited to dipolar supersolids. It can be equally applied to dipolar mixtures, which are expected to have longer lifetimes than single-component dipolar gases [178–181] and whose excitation spectrum has been recently investigated [182]. Another interesting system for the application of our protocol are semiconductor dipolar excitons, where ring configurations naturally occur (see, e.g., [183, 184] and references therein), and where cluster crystallization has been observed [185, 186].

A

Appendix

A.1. Scaling and dimensionless formulation of the equations

The first step in numerical implementation is to rescale the equation, to avoid excessively large or small numbers that could lead to numerical inaccuracies due to finite floating-point precision. This is done by selecting appropriate reference parameters and expressing all variables in terms of them.

To introduce a natural scaling for the system, we define the reference frequency as the geometric mean of the trapping frequencies along the three directions:

$$\omega_{\mathrm{ref}} = \sqrt[3]{\omega_x \omega_y \omega_z}. \tag{A.1}$$

If the system is unconfined in one (two) directions, the reference frequency can be adapted by considering only the remaining two (one) trapping frequencies. This choice sets the characteristic timescale, allowing to express the harmonic frequencies in dimensionless form:

$$\tilde{\omega}_x = \frac{\omega_x}{\omega_{\mathrm{ref}}}, \quad \tilde{\omega}_y = \frac{\omega_y}{\omega_{\mathrm{ref}}}, \quad \tilde{\omega}_z = \frac{\omega_z}{\omega_{\mathrm{ref}}}. \tag{A.2}$$

Accordingly, time and its derivative transform as

$$\tilde{t} = \omega_{\mathrm{ref}}\, t, \quad \frac{\partial}{\partial \tilde{t}} = \frac{1}{\omega_{\mathrm{ref}}} \frac{\partial}{\partial t}. \tag{A.3}$$

To establish a natural length scale, we use the corresponding harmonic oscillator length:

$$a_{\mathrm{ref}} = \sqrt{\frac{\hbar}{m\omega_{\mathrm{ref}}}}. \tag{A.4}$$

All spatial coordinates are then rescaled as

$$\tilde{x} = \frac{x}{a_{\text{ref}}}, \quad \tilde{y} = \frac{y}{a_{\text{ref}}}, \quad \tilde{z} = \frac{z}{a_{\text{ref}}}. \tag{A.5}$$

Similarly, the s-wave scattering length and dipolar length are expressed in terms of a_{ref}:

$$\tilde{a} = \frac{a}{a_{\text{ref}}}, \quad \tilde{a}_{\text{dd}} = \frac{a_{\text{dd}}}{a_{\text{ref}}}. \tag{A.6}$$

The Laplace operator transforms accordingly:

$$\Delta = \frac{1}{a_{\text{ref}}^2}\left(\frac{\partial^2}{\partial\tilde{x}^2} + \frac{\partial^2}{\partial\tilde{y}^2} + \frac{\partial^2}{\partial\tilde{z}^2}\right) = \frac{1}{a_{\text{ref}}^2}\tilde{\Delta}. \tag{A.7}$$

To maintain the normalization of the wavefunction, we introduce the rescaling

$$\tilde{\Psi} = a_{\text{ref}}^{3/2}\,\Psi. \tag{A.8}$$

With these transformations, the extended Gross-Pitaevskii equation (3.6) takes on its dimensionless form:

$$\begin{aligned} i\frac{\partial}{\partial\tilde{t}}\tilde{\Psi} &= \hat{\tilde{H}}\tilde{\Psi} = \\ &\left[-\frac{1}{2}\tilde{\Delta} + \tilde{V}_{\text{ext}} + \tilde{g}|\tilde{\Psi}|^2 + \int d\tilde{\mathbf{r}}'\tilde{V}_{\text{dd}}(\tilde{\mathbf{r}} - \tilde{\mathbf{r}}')|\tilde{\Psi}(\tilde{\mathbf{r}}')|^2 + \tilde{\gamma}|\tilde{\Psi}|^3\right]\tilde{\Psi}. \end{aligned} \tag{A.9}$$

Here, the interaction strengths are rescaled as

$$g = \frac{\hbar^2}{m}a_{\text{ref}}\,\tilde{g}, \quad \gamma = \frac{\hbar^2}{m}a_{\text{ref}}^{5/2}\,\tilde{\gamma}. \tag{A.10}$$

The external potential in dimensionless form becomes

$$\tilde{V}_{\text{ext}} = \frac{1}{2}\left(\tilde{\omega}_x^2\tilde{x}^2 + \tilde{\omega}_y^2\tilde{y}^2 + \tilde{\omega}_z^2\tilde{z}^2\right), \tag{A.11}$$

and the rescaled dipole-dipole interaction potential is given by

$$\tilde{V}_{\text{dd}}(\tilde{\mathbf{r}} - \tilde{\mathbf{r}}') = 3\tilde{a}_{\text{dd}}\frac{1 - 3\cos^2\theta}{|\tilde{\mathbf{r}} - \tilde{\mathbf{r}}'|^3}. \tag{A.12}$$

Similarly, the stationary eGPE (3.10) can be expressed in a dimensionless form as

$$\tilde{\mu}\tilde{\psi}_0 = \hat{\tilde{H}}\tilde{\psi}_0, \tag{A.13}$$

where the chemical potential is rescaled as

$$\tilde{\mu} = \frac{\mu}{\hbar\omega_{\text{ref}}}. \tag{A.14}$$

List of publications

The results presented in this thesis are documented in the following publications:

[1] *Creation and robustness of quantized vortices in a dipolar supersolid when crossing the superfluid-to-supersolid transition.* Marija Šindik, Alessio Recati, Santo Maria Roccuzzo, Luis Santos, and Sandro Stringari.
Phys. Rev. A **106**, L061303 (2022).

[2] *Sound, Superfluidity, and Layer Compressibility in a Ring Dipolar Supersolid.* Marija Šindik, Tomasz Zawiślak, Alessio Recati, and Sandro Stringari.
Phys. Rev. Lett. **132**, 146001 (2024).

Other related publications not included in this thesis:

[3] *Anomalous Doppler effect in superfluid and supersolid atomic gases.* Tomasz Zawiślak, Marija Šindik, Sandro Stringari, and Alessio Recati.
arXiv: 2408.16489 (2024)

Bibliography

[1] Eugene P. Gross. *Unified Theory of Interacting Bosons*. Phys. Rev. **106**, 161 (1957).

[2] E. P. Gross. *Classical theory of boson wave fields*. Annals of Physics **4**, 57 (1958).

[3] C. N. Yang. *Concept of Off-Diagonal Long-Range Order and the Quantum Phases of Liquid He and of Superconductors*. Rev. Mod. Phys. **34**, 694 (1962).

[4] A. F. Andreev and I. M. Lifshitz. *Quantum Theory of Defects in Crystals*. Sov. Phys. JETP **29**, 1107 (1969).

[5] D. J. Thouless. *The flow of a dense superfluid*. Annals of Physics **52**, 403 (1969).

[6] G. V. Chester. *Speculations on Bose-Einstein Condensation and Quantum Crystals*. Phys. Rev. A **2**, 256 (1970).

[7] A. J. Leggett. *Can a Solid Be "Superfluid"?* Phys. Rev. Lett. **25**, 1543 (1970).

[8] Oliver Penrose and Lars Onsager. *Bose-Einstein Condensation and Liquid Helium*. Phys. Rev. **104**, 576 (1956).

[9] Massimo Boninsegni and Nikolay V. Prokof'ev. *Colloquium: Supersolids: What and where are they?* Rev. Mod. Phys. **84**, 759 (2012).

[10] Jun-Ru Li, Jeongwon Lee, Wujie Huang, Sean Burchesky, Boris Shteynas, Furkan Çağrı Top, Alan O. Jamison, and Wolfgang Ketterle. *A stripe phase with supersolid properties in spin–orbit-coupled Bose–Einstein condensates*. Nature **543**, 91 (2017).

[11] Julian Léonard, Andrea Morales, Philip Zupancic, Tilman Esslinger, and Tobias Donner. *Supersolid formation in a quantum gas breaking a continuous translational symmetry*. Nature **543**, 87 (2017).

[12] L. Tanzi, E. Lucioni, F. Famà, J. Catani, A. Fioretti, C. Gabbanini, R. N. Bisset, L. Santos, and G. Modugno. *Observation of a Dipolar Quantum Gas with Metastable Supersolid Properties*. Phys. Rev. Lett. **122**, 130405 (2019).

[13] Fabian Böttcher, Jan-Niklas Schmidt, Matthias Wenzel, Jens Hertkorn, Mingyang Guo, Tim Langen, and Tilman Pfau. *Transient Supersolid Properties in an Array of Dipolar Quantum Droplets*. Phys. Rev. X **9**, 011051 (2019).

[14] L. Chomaz, D. Petter, P. Ilzhöfer, G. Natale, A. Trautmann, C. Politi, G. Durastante, R. M. W. van Bijnen, A. Patscheider, M. Sohmen, M. J. Mark, and F. Ferlaino. *Long-Lived and Transient Supersolid Behaviors in Dipolar Quantum Gases*. Phys. Rev. X **9**, 021012 (2019).

[15] Alessio Recati and Sandro Stringari. *Supersolidity in ultracold dipolar gases*. Nature Reviews Physics **5**, 735 (2023).

[16] Gentaro Watanabe and C. J. Pethick. *Superfluid Density of Neutrons in the Inner Crust of Neutron Stars: New Life for Pulsar Glitch Models*. Phys. Rev. Lett. **119**, 062701 (2017).

[17] Thomas Bland, Francesca Ferlaino, Massimo Mannarelli, Elena Poli, and Silvia Trabucco. *Exploring Pulsar Glitches with Dipolar Supersolids*. Few-Body Systems **65**, 81 (2024).

[18] Luca Pezzè, Klejdja Xhani, Cyprien Daix, Nicola Grani, Beatrice Donelli, Francesco Scazza, Diego Hernandez-Rajkov, Woo Jin Kwon, Giulia Del Pace, and Giacomo Roati. *Stabilizing persistent currents in an atomtronic Josephson junction necklace*. Nature Communications **15**, 4831 (2024).

[19] L. Amico et al. *Roadmap on Atomtronics: State of the art and perspective*. AVS Quantum Science **3**, 039201 (2021).

[20] J. F. Allen and A. D. Misener. *Flow of Liquid Helium II*. Nature **141**, 75 (1938).

[21] P. Kapitza. *Viscosity of Liquid Helium below the λ-Point*. Nature **141**, 74 (1938).

[22] Lev Pitaevskii and Sandro Stringari. *Bose-Einstein Condensation and Superfluidity*. Oxford University Press (2016).

[23] C. J. Pethick and H. Smith. *Bose–Einstein Condensation in Dilute Gases*. Cambridge University Press (2008).

[24] Sebastien Balibar. *The enigma of supersolidity*. Nature **464**, 176 (2010).

[25] E. Kim and M. H. W. Chan. *Probable observation of a supersolid helium phase*. Nature **427**, 225 (2004).

[26] E. Kim and M. H. W. Chan. *Observation of Superflow in Solid Helium*. Science **305**, 1941 (2004).

[27] Duk Y. Kim and Moses H. W. Chan. *Absence of Supersolidity in Solid Helium in Porous Vycor Glass*. Phys. Rev. Lett. **109**, 155301 (2012).

[28] M. H. Anderson, J. R. Ensher, M. R. Matthews, C. E. Wieman, and E. A. Cornell. *Observation of Bose-Einstein Condensation in a Dilute Atomic Vapor*. Science **269**, 198 (1995).

[29] K. B. Davis, M. -O. Mewes, M. R. Andrews, N. J. van Druten, D. S. Durfee, D. M. Kurn, and W. Ketterle. *Bose-Einstein Condensation in a Gas of Sodium Atoms*. Phys. Rev. Lett. **75**, 3969 (1995).

[30] Christian Gross and Immanuel Bloch. *Quantum simulations with ultracold atoms in optical lattices*. Science **357**, 995 (2017).

[31] Immanuel Bloch, Jean Dalibard, and Wilhelm Zwerger. *Many-body physics with ultracold gases*. Rev. Mod. Phys. **80**, 885 (2008).

[32] Cheng Chin, Rudolf Grimm, Paul Julienne, and Eite Tiesinga. *Feshbach resonances in ultracold gases*. Rev. Mod. Phys. **82**, 1225 (2010).

[33] Yves Pomeau and Sergio Rica. *Dynamics of a model of supersolid*. Phys. Rev. Lett. **72**, 2426 (1994).

[34] Christophe Josserand, Yves Pomeau, and Sergio Rica. *Coexistence of Ordinary Elasticity and Superfluidity in a Model of a Defect-Free Supersolid*. Phys. Rev. Lett. **98**, 195301 (2007).

[35] F. Cinti, P. Jain, M. Boninsegni, A. Micheli, P. Zoller, and G. Pupillo. *Supersolid Droplet Crystal in a Dipole-Blockaded Gas*. Phys. Rev. Lett. **105**, 135301 (2010).

[36] N. Henkel, R. Nath, and T. Pohl. *Three-Dimensional Roton Excitations and Supersolid Formation in Rydberg-Excited Bose-Einstein Condensates*. Phys. Rev. Lett. **104**, 195302 (2010).

[37] Y.-J. Lin, K. Jiménez-García, and I. B. Spielman. *Spin–orbit-coupled Bose–Einstein condensates*. Nature **471**, 83 (2011).

[38] Tin-Lun Ho and Shizhong Zhang. *Bose-Einstein Condensates with Spin-Orbit Interaction*. Phys. Rev. Lett. **107**, 150403 (2011).

[39] Yun Li, Lev P. Pitaevskii, and Sandro Stringari. *Quantum Tricriticality and Phase Transitions in Spin-Orbit Coupled Bose-Einstein Condensates*. Phys. Rev. Lett. **108**, 225301 (2012).

[40] C. S. Chisholm, S. Hirthe, V. B. Makhalov, R. Ramos, R. Vatré, J. Cabedo, A. Celi, and L. Tarruell. *Probing supersolidity through excitations in a spin-orbit-coupled Bose-Einstein condensate* arXiv: 2412.13861 (2024).

[41] Andika Putra, F. Salces-Cárcoba, Yuchen Yue, Seiji Sugawa, and I. B. Spielman. *Spatial Coherence of Spin-Orbit-Coupled Bose Gases*. Phys. Rev. Lett. **124**, 053605 (2020).

[42] Yun Li, Giovanni I. Martone, Lev P. Pitaevskii, and Sandro Stringari. *Superstripes and the Excitation Spectrum of a Spin-Orbit-Coupled Bose-Einstein Condensate*. Phys. Rev. Lett. **110**, 235302 (2013).

[43] Kevin T. Geier, Giovanni I. Martone, Philipp Hauke, and Sandro Stringari. *Exciting the Goldstone Modes of a Supersolid Spin-Orbit-Coupled Bose Gas*. Phys. Rev. Lett. **127**, 115301 (2021).

[44] Li Chen, Han Pu, Zeng-Qiang Yu, and Yunbo Zhang. *Collective excitation of a trapped Bose-Einstein condensate with spin-orbit coupling*. Phys. Rev. A **95**, 033616 (2017).

[45] Giovanni Italo Martone and Sandro Stringari. *Supersolid phase of a spin-orbit-coupled Bose-Einstein condensate: A perturbation approach*. SciPost Phys. **11**, 092 (2021).

[46] Kevin T. Geier, Giovanni I. Martone, Philipp Hauke, Wolfgang Ketterle, and Sandro Stringari. *Dynamics of Stripe Patterns in Supersolid Spin-Orbit-Coupled Bose Gases*. Phys. Rev. Lett. **130**, 156001 (2023).

[47] Kristian Baumann, Christine Guerlin, Ferdinand Brennecke, and Tilman Esslinger. *Dicke quantum phase transition with a superfluid gas in an optical cavity*. Nature **464**, 1301 (2010).

[48] R. Mottl, F. Brennecke, K. Baumann, R. Landig, T. Donner, and T. Esslinger. *Roton-Type Mode Softening in a Quantum Gas with Cavity-Mediated Long-Range Interactions*. Science **336**, 1570 (2012).

[49] Julian Léonard, Andrea Morales, Philip Zupancic, Tobias Donner, and Tilman Esslinger. *Monitoring and manipulating Higgs and Goldstone modes in a supersolid quantum gas*. Science **358**, 1415 (2017).

[50] Yudan Guo, Ronen M. Kroeze, Brendan P. Marsh, Sarang Gopalakrishnan, Jonathan Keeling, and Benjamin L. Lev. *An optical lattice with sound*. Nature **599**, 211 (2021).

[51] S. C. Schuster, P. Wolf, S. Ostermann, S. Slama, and C. Zimmermann. *Supersolid Properties of a Bose-Einstein Condensate in a Ring Resonator*. Phys. Rev. Lett. **124**, 143602 (2020).

[52] Tobias Donner Farokh Mivehvar Francesco Piazza and Helmut Ritsch. *Cavity QED with quantum gases: new paradigms in many-body physics*. Advances in Physics **70**, 1 (2021).

[53] Lauriane Chomaz, Igor Ferrier-Barbut, Francesca Ferlaino, Bruno Laburthe-Tolra, Benjamin L Lev, and Tilman Pfau. *Dipolar physics: a review of experiments with magnetic quantum gases*. Reports on Progress in Physics **86**, 026401 (2022).

[54] Fabian Böttcher, Jan-Niklas Schmidt, Jens Hertkorn, Kevin S H Ng, Sean D Graham, Mingyang Guo, Tim Langen, and Tilman Pfau. *New states of matter with fine-tuned interactions: quantum droplets and dipolar supersolids*. Reports on Progress in Physics **84**, 012403 (2020).

[55] T Lahaye, C Menotti, L Santos, M Lewenstein, and T Pfau. *The physics of dipolar bosonic quantum gases*. Reports on Progress in Physics **72**, 126401 (2009).

[56] Santo Maria Roccuzzo and Francesco Ancilotto. *Supersolid behavior of a dipolar Bose-Einstein condensate confined in a tube*. Phys. Rev. A **99**, 041601 (2019).

[57] P. Ilzhöfer, M. Sohmen, G. Durastante, C. Politi, A. Trautmann, G. Natale, G. Morpurgo, T. Giamarchi, L. Chomaz, M. J. Mark, and F. Ferlaino. *Phase coherence in out-of-equilibrium supersolid states of ultracold dipolar atoms*. Nature Physics **17**, 356 (2021).

[58] T. Bland, E. Poli, C. Politi, L. Klaus, M. A. Norcia, F. Ferlaino, L. Santos, and R. N. Bisset. *Two-Dimensional Supersolid Formation in Dipolar Condensates*. Phys. Rev. Lett. **128**, 195302 (2022).

[59] L. Tanzi, S. M. Roccuzzo, E. Lucioni, F. Famà, A. Fioretti, C. Gabbanini, G. Modugno, A. Recati, and S. Stringari. *Supersolid symmetry breaking from compressional oscillations in a dipolar quantum gas*. Nature **574**, 382 (2019).

[60] Mingyang Guo, Fabian Böttcher, Jens Hertkorn, Jan-Niklas Schmidt, Matthias Wenzel, Hans Peter Büchler, Tim Langen, and Tilman Pfau. *The low-energy Goldstone mode in a trapped dipolar supersolid*. Nature **574**, 386 (2019).

[61] G. Natale, R. M. W. van Bijnen, A. Patscheider, D. Petter, M. J. Mark, L. Chomaz, and F. Ferlaino. *Excitation Spectrum of a Trapped Dipolar Supersolid and Its Experimental Evidence*. Phys. Rev. Lett. **123**, 050402 (2019).

[62] S. M. Roccuzzo, A. Gallemí, A. Recati, and S. Stringari. *Rotating a Supersolid Dipolar Gas*. Phys. Rev. Lett. **124**, 045702 (2020).

[63] D. Guéry-Odelin and S. Stringari. *Scissors Mode and Superfluidity of a Trapped Bose-Einstein Condensed Gas*. Phys. Rev. Lett. **83**, 4452 (1999).

[64] O. M. Maragò, S. A. Hopkins, J. Arlt, E. Hodby, G. Hechenblaikner, and C. J. Foot. *Observation of the Scissors Mode and Evidence for Superfluidity of a Trapped Bose-Einstein Condensed Gas*. Phys. Rev. Lett. **84**, 2056 (2000).

[65] L. Tanzi, J. G. Maloberti, G. Biagioni, A. Fioretti, C. Gabbanini, and G. Modugno. *Evidence of superfluidity in a dipolar supersolid from nonclassical rotational inertia*. Science **371**, 1162 (2021).

[66] S. M. Roccuzzo, A. Recati, and S. Stringari. *Moment of inertia and dynamical rotational response of a supersolid dipolar gas*. Phys. Rev. A **105**, 023316 (2022).

[67] Matthew A. Norcia, Elena Poli, Claudia Politi, Lauritz Klaus, Thomas Bland, Manfred J. Mark, Luis Santos, Russell N. Bisset, and Francesca Ferlaino. *Can Angular Oscillations Probe Superfluidity in Dipolar Supersolids?* Phys. Rev. Lett. **129**, 040403 (2022).

[68] Matthew A. Norcia, Claudia Politi, Lauritz Klaus, Elena Poli, Maximilian Sohmen, Manfred J. Mark, Russell N. Bisset, Luis Santos, and Francesca Ferlaino. *Two-dimensional supersolidity in a dipolar quantum gas*. Nature **596**, 357 (2021).

[69] Axel Griesmaier, Jörg Werner, Sven Hensler, Jürgen Stuhler, and Tilman Pfau. *Bose-Einstein Condensation of Chromium*. Phys. Rev. Lett. **94**, 160401 (2005).

[70] Mingwu Lu, Nathaniel Q. Burdick, Seo Ho Youn, and Benjamin L. Lev. *Strongly Dipolar Bose-Einstein Condensate of Dysprosium*. Phys. Rev. Lett. **107**, 190401 (2011).

[71] K. Aikawa, A. Frisch, M. Mark, S. Baier, A. Rietzler, R. Grimm, and F. Ferlaino. *Bose-Einstein Condensation of Erbium*. Phys. Rev. Lett. **108**, 210401 (2012).

[72] Claude Cohen-Tannoudji and David Guéry-Odelin. *Advances in Atomic Phy-sics*. World Scientific (2011).

[73] Steven A. Moses, Jacob P. Covey, Matthew T. Miecnikowski, Deborah S. Jin, and Jun Ye. *New frontiers for quantum gases of polar molecules*. Nature Physics **13**, 13 (2017).

[74] Robert Löw, Hendrik Weimer, Johannes Nipper, Jonathan B Balewski, Björn Butscher, Hans Peter Büchler, and Tilman Pfau. *An experimental and theoretical guide to strongly interacting Rydberg gases*. Journal of Physics B: Atomic, Molecular and Optical Physics **45**, 113001 (2012).

[75] Luigi De Marco, Giacomo Valtolina, Kyle Matsuda, William G. Tobias, Jacob P. Covey, and Jun Ye. *A degenerate Fermi gas of polar molecules*. Science **363**, 853 (2019).

[76] Giacomo Valtolina, Kyle Matsuda, William G. Tobias, Jun-Ru Li, Luigi De Marco, and Jun Ye. *Dipolar evaporation of reactive molecules to below the Fermi temperature*. Nature **588**, 239 (2020).

[77] Yu. Kagan, A. E. Muryshev, and G. V. Shlyapnikov. *Collapse and Bose-Einstein Condensation in a Trapped Bose Gas with Negative Scattering Length*. Phys. Rev. Lett. **81**, 933 (1998).

[78] J. L. Roberts, N. R. Claussen, S. L. Cornish, E. A. Donley, E. A. Cornell, and C. E. Wieman. *Controlled Collapse of a Bose-Einstein Condensate*. Phys. Rev. Lett. **86**, 4211 (2001).

[79] Stefano Giovanazzi, Axel Görlitz, and Tilman Pfau. *Tuning the Dipolar Interaction in Quantum Gases*. Phys. Rev. Lett. **89**, 130401 (2002).

[80] Yijun Tang, Wil Kao, Kuan-Yu Li, and Benjamin L. Lev. *Tuning the Dipole-Dipole Interaction in a Quantum Gas with a Rotating Magnetic Field*. Phys. Rev. Lett. **120**, 230401 (2018).

[81] T. Koch, T. Lahaye, J. Metz, B. Fröhlich, A. Griesmaier, and T. Pfau. *Stabilization of a purely dipolar quantum gas against collapse*. Nature Physics **4**, 218 (2008).

[82] Lev Davidovich Landau. *On the Theory of Superfluidity of Helium II*. J. Phys. (USSR) **11** (1947).

[83] R. P. Feynman. *Atomic Theory of the Two-Fluid Model of Liquid Helium*. Phys. Rev. **94**, 262 (1954).

[84] L. Santos, G. V. Shlyapnikov, and M. Lewenstein. *Roton-Maxon Spectrum and Stability of Trapped Dipolar Bose-Einstein Condensates*. Phys. Rev. Lett. **90**, 250403 (2003).

[85] Yu. A. Nepomnyashchii D.A. Kirzhnits. *Coherent Crystallization of Quantum Liquid*. Sov. Phys. JETP **32**, 1191 (1970).

[86] T. Schneider and C. P. Enz. *Theory of the Superfluid-Solid Transition of* ^{4}He. Phys. Rev. Lett. **27**, 1186 (1971).

[87] P. Nozières. *Is the Roton in Superfluid 4He the Ghost of a Bragg Spot?* Journal of Low Temperature Physics **137**, 45 (2004).

[88] J. Hertkorn, J.-N. Schmidt, F. Böttcher, M. Guo, M. Schmidt, K. S. H. Ng, S. D. Graham, H. P. Büchler, T. Langen, M. Zwierlein, and T. Pfau. *Density Fluctuations across the Superfluid-Supersolid Phase Transition in a Dipolar Quantum Gas*. Phys. Rev. X **11**, 011037 (2021).

[89] Santo Maria Roccuzzo. "Supersolidity in a dipolar quantum gas". PhD thesis. University of Trento (2021).

[90] L. Chomaz, R. M. W. van Bijnen, D. Petter, G. Faraoni, S. Baier, J. H. Becher, M. J. Mark, F. Wächtler, L. Santos, and F. Ferlaino. *Observation of roton mode population in a dipolar quantum gas*. Nature Physics **14**, 442 (2018).

[91] D. Petter, G. Natale, R. M. W. van Bijnen, A. Patscheider, M. J. Mark, L. Chomaz, and F. Ferlaino. *Probing the Roton Excitation Spectrum of a Stable Dipolar Bose Gas*. Phys. Rev. Lett. **122**, 183401 (2019).

[92] J.-N. Schmidt, J. Hertkorn, M. Guo, F. Böttcher, M. Schmidt, K. S. H. Ng, S. D. Graham, T. Langen, M. Zwierlein, and T. Pfau. *Roton Excitations in an Oblate Dipolar Quantum Gas*. Phys. Rev. Lett. **126**, 193002 (2021).

[93] T. Lahaye, J. Metz, B. Fröhlich, T. Koch, M. Meister, A. Griesmaier, T. Pfau, H. Saito, Y. Kawaguchi, and M. Ueda. *d-Wave Collapse and Explosion of a Dipolar Bose-Einstein Condensate*. Phys. Rev. Lett. **101**, 080401 (2008).

[94] T. D. Lee, Kerson Huang, and C. N. Yang. *Eigenvalues and Eigenfunctions of a Bose System of Hard Spheres and Its Low-Temperature Properties*. Phys. Rev. **106**, 1135 (1957).

[95] T. D. Lee and C. N. Yang. *Many-Body Problem in Quantum Mechanics and Quantum Statistical Mechanics*. Phys. Rev. **105**, 1119 (1957).

[96] Aristeu R. P. Lima and Axel Pelster. *Quantum fluctuations in dipolar Bose gases*. Phys. Rev. A **84**, 041604 (2011).

[97] A. R. P. Lima and A. Pelster. *Beyond mean-field low-lying excitations of dipolar Bose gases*. Phys. Rev. A **86**, 063609 (2012).

[98] Ralf Schützhold, Michael Uhlmann, Yan Xu, and Uwe R. Fischer. *Mean-field expansion in Bose–Einstein condensates with finite-range interactions*. International Journal of Modern Physics B **20**, 3555 (2006).

[99] F. Wächtler and L. Santos. *Quantum filaments in dipolar Bose-Einstein condensates*. Phys. Rev. A **93**, 061603 (2016).

[100] D. S. Petrov. *Quantum Mechanical Stabilization of a Collapsing Bose-Bose Mixture*. Phys. Rev. Lett. **115**, 155302 (2015).

[101] P. B. Blakie, D. Baillie, L. Chomaz, and F. Ferlaino. *Supersolidity in an elongated dipolar condensate*. Phys. Rev. Res. **2**, 043318 (2020).

[102] Joseph C. Smith, D. Baillie, and P. B. Blakie. *Supersolidity and crystallization of a dipolar Bose gas in an infinite tube*. Phys. Rev. A **107**, 033301 (2023).

[103] Holger Kadau, Matthias Schmitt, Matthias Wenzel, Clarissa Wink, Thomas Maier, Igor Ferrier-Barbut, and Tilman Pfau. *Observing the Rosensweig instability of a quantum ferrofluid*. Nature **530**, 194 (2016).

[104] Igor Ferrier-Barbut, Holger Kadau, Matthias Schmitt, Matthias Wenzel, and Tilman Pfau. *Observation of Quantum Droplets in a Strongly Dipolar Bose Gas*. Phys. Rev. Lett. **116**, 215301 (2016).

[105] Igor Ferrier-Barbut, Matthias Schmitt, Matthias Wenzel, Holger Kadau, and Tilman Pfau. *Liquid quantum droplets of ultracold magnetic atoms*. Journal of Physics B: Atomic, Molecular and Optical Physics **49**, 214004 (2016).

[106] F. Wächtler and L. Santos. *Ground-state properties and elementary excitations of quantum droplets in dipolar Bose-Einstein condensates*. Phys. Rev. A **94**, 043618 (2016).

[107] D. Baillie, R. M. Wilson, R. N. Bisset, and P. B. Blakie. *Self-bound dipolar droplet: A localized matter wave in free space*. Phys. Rev. A **94**, 021602 (2016).

[108] Matthias Schmitt, Matthias Wenzel, Fabian Böttcher, Igor Ferrier-Barbut, and Tilman Pfau. *Self-bound droplets of a dilute magnetic quantum liquid*. Nature **539**, 259 (2016).

[109] S. Saccani, S. Moroni, and M. Boninsegni. *Excitation Spectrum of a Supersolid*. Phys. Rev. Lett. **108**, 175301 (2012).

[110] Yong-Chang Zhang, Thomas Pohl, and Fabian Maucher. *Phases of supersolids in confined dipolar Bose-Einstein condensates*. Phys. Rev. A **104**, 013310 (2021).

[111] J. Hertkorn, J.-N. Schmidt, M. Guo, F. Böttcher, K. S. H. Ng, S. D. Graham, P. Uerlings, T. Langen, M. Zwierlein, and T. Pfau. *Pattern formation in quantum ferrofluids: From supersolids to superglasses*. Phys. Rev. Res. **3**, 033125 (2021).

[112] E. P. Gross. *Structure of a quantized vortex in boson systems*. Il Nuovo Cimento (1955-1965) **20**, 454 (1961).

[113] L. P. Pitaevskii. *Vortex Lines in an Imperfect Bose Gas*. JETP **13**, 451 (1961).

[114] Franco Dalfovo, Stefano Giorgini, Lev P. Pitaevskii, and Sandro Stringari. *Theory of Bose-Einstein condensation in trapped gases*. Rev. Mod. Phys. **71**, 463 (1999).

[115] Anthony J. Leggett. *Bose-Einstein condensation in the alkali gases: Some fundamental concepts*. Rev. Mod. Phys. **73**, 307 (2001).

[116] N. N. Bogolyubov. *On the theory of superfluidity*. J. Phys. (USSR) **11**, 23 (1947).

[117] A. J. Leggett. *On the Superfluid Fraction of an Arbitrary Many-Body System at T=0*. Journal of Statistical Physics **93**, 927 (1998).

[118] L. Tisza. *Transport Phenomena in Helium II*. Nature **141**, 913 (1938).

[119] L. Landau. *Theory of the Superfluidity of Helium II*. Phys. Rev. **60**, 356 (1941).

[120] Daniel Pérez-Cruz, Grigori E. Astrakharchik, and Pietro Massignan. *Superfluid fraction of interacting bosonic gases*. Phys. Rev. A **111**, L011302 (2025).

[121] G. Chauveau, C. Maury, F. Rabec, C. Heintze, G. Brochier, S. Nascimbene, J. Dalibard, J. Beugnon, S. M. Roccuzzo, and S. Stringari. *Superfluid Fraction in an Interacting Spatially Modulated Bose-Einstein Condensate*. Phys. Rev. Lett. **130**, 226003 (2023).

[122] G. Biagioni, N. Antolini, B. Donelli, L. Pezzè, A. Smerzi, M. Fattori, A. Fioretti, C. Gabbanini, M. Inguscio, L. Tanzi, and G. Modugno. *Measurement of the superfluid fraction of a supersolid by Josephson effect*. Nature **629**, 773 (2024).

[123] D. Forster. *Hydrodynamic Fluctuations, Broken Symmetry, And Correlation Functions*. CRC Press, Taylor&Francis Group (1990).

[124] P. C. Martin, O. Parodi, and P. S. Pershan. *Unified Hydrodynamic Theory for Crystals, Liquid Crystals, and Normal Fluids*. Phys. Rev. A **6**, 2401 (1972).

[125] Haruki Watanabe and Tomá š Brauner. *Spontaneous breaking of continuous translational invariance*. Phys. Rev. D **85**, 085010 (2012).

[126] C.-D. Yoo and Alan T. Dorsey. *Hydrodynamic theory of supersolids: Variational principle, effective Lagrangian, and density-density correlation function*. Phys. Rev. B **81**, 134518 (2010).

[127] Johannes Hofmann and Wilhelm Zwerger. *Hydrodynamics of a superfluid smectic*. Journal of Statistical Mechanics: Theory and Experiment **2021**, 033104 (2021).

[128] D. T. Son. *Effective Lagrangian and Topological Interactions in Supersolids*. Phys. Rev. Lett. **94**, 175301 (2005).

[129] Mario Liu. *Two possible types of superfluidity in crystals*. Phys. Rev. B **18**, 1165 (1978).

[130] W. M. Saslow. *Microscopic and hydrodynamic theory of superfluidity in periodic solids*. Phys. Rev. B **15**, 173 (1977).

[131] I. M . Khalatnikov. *An Introduction To The Theory Of Superfluidity*. CRC Press (2000).

[132] S. J. Putterman. *Superfluid Hydrodynamics*. North-Holland Publishing Company, Amsterdam (1974).

[133] Mario Liu. *Superfluid dynamics, equilibrium conditions, and centripetal forces*. Journal of Statistical Mechanics: Theory and Experiment **2023**, 033104 (2023).

[134] L. M. Platt, D. Baillie, and P. B. Blakie. *Sound waves and fluctuations in one-dimensional supersolids*. Phys. Rev. A **110**, 023320 (2024).

[135] Tomasz Zawiślak, Marija Šindik, Sandro Stringari, and Alessio Recati. *Anomalous Doppler effect in superfluid and supersolid atomic gases* arXiv: 2408.16489 (2024).

[136] S. M. Roccuzzo. *UltraCold*. https://github.com/smroccuzzo/UltraCold (2022).

[137] L. Lehtovaara, J. Toivanen, and J. Eloranta. *Solution of time-independent Schrödinger equation by the imaginary time propagation method*. Journal of Computational Physics **221**, 148 (2007).

[138] M.E.J. Newman. *Computational Physics*. University Of Michigan (2013).

[139] B.T. Polyak. *Some methods of speeding up the convergence of iteration methods*. USSR Computational Mathematics and Mathematical Physics **4**, 1 (1964).

[140] Hedy Attouch, Xavier Goudou, and P.redont. *The heavy ball with friction method, I. The continuous dynamical system: Global exploration of the local minima of a real-valued function by asymptotic analysis of a dissipative dynamical system*. Communications in Contemporary Mathematics **02** (2011).

[141] W. H. Press, S. A. Teukolsky, W. T. Vetterling, and B. P. Flannery. *Numerical Recipes: The Art of Scientific Computing*. Cambridge University Press (2007).

[142] Matteo Frigo and Steven G. Johnson. *The Design and Implementation of FFTW3*. Proceedings of the IEEE **93**, 216 (2005).

[143] cuFFT: https://docs.nvidia.com/cuda/cufft/.

[144] Shai Ronen, Daniele C. E. Bortolotti, and John L. Bohn. *Bogoliubov modes of a dipolar condensate in a cylindrical trap*. Phys. Rev. A **74**, 013623 (2006).

[145] H.-Y. Lu, H. Lu, J.-N. Zhang, R.-Z. Qiu, H. Pu, and S. Yi. *Spatial density oscillations in trapped dipolar condensates*. Phys. Rev. A **82**, 023622 (2010).

[146] ARPACK-NG: `https://github.com/opencollab/arpack-ng`.

[147] A. Gallemí, S. M. Roccuzzo, S. Stringari, and A. Recati. *Quantized vortices in dipolar supersolid Bose-Einstein-condensed gases*. Phys. Rev. A **102**, 023322 (2020).

[148] Eva Casotti, Elena Poli, Lauritz Klaus, Andrea Litvinov, Clemens Ulm, Claudia Politi, Manfred J. Mark, Thomas Bland, and Francesca Ferlaino. *Observation of vortices in a dipolar supersolid*. Nature **635**, 327 (2024).

[149] M. W. Zwierlein, J. R. Abo-Shaeer, A. Schirotzek, C. H. Schunck, and W. Ketterle. *Vortices and superfluidity in a strongly interacting Fermi gas*. Nature **435**, 1047 (2005).

[150] Marija Šindik, Alessio Recati, Santo Maria Roccuzzo, Luis Santos, and Sandro Stringari. *Creation and robustness of quantized vortices in a dipolar supersolid when crossing the superfluid-to-supersolid transition*. Phys. Rev. A **106**, L061303 (2022).

[151] Russell J. Donnelly. *Quntized vortices in helium II*. Cambridge University Press (1991).

[152] M. R. Matthews, B. P. Anderson, P. C. Haljan, D. S. Hall, C. E. Wieman, and E. A. Cornell. *Vortices in a Bose-Einstein Condensate*. Phys. Rev. Lett. **83**, 2498 (1999).

[153] K. W. Madison, F. Chevy, W. Wohlleben, and J. Dalibard. *Vortex Formation in a Stirred Bose-Einstein Condensate*. Phys. Rev. Lett. **84**, 806 (2000).

[154] J. R. Abo-Shaeer, C. Raman, J. M. Vogels, and W. Ketterle. *Observation of Vortex Lattices in Bose-Einstein Condensates*. Science **292**, 476 (2001).

[155] Lauritz Klaus, Thomas Bland, Elena Poli, Claudia Politi, Giacomo Lamporesi, Eva Casotti, Russell N. Bisset, Manfred J. Mark, and Francesca Ferlaino. *Observation of vortices and vortex stripes in a dipolar condensate*. Nature Physics **18**, 1453 (2022).

[156] Thomas Bland, Giacomo Lamporesi, Manfred J. Mark, and Francesca Ferlaino. *Vortices in dipolar Bose–Einstein condensates*. en. Proceedings. Physics **24**, 133 (2023).

[157] A. Recati, F. Zambelli, and S. Stringari. *Overcritical Rotation of a Trapped Bose-Einstein Condensate*. Phys. Rev. Lett. **86**, 377 (2001).

[158] Subhasis Sinha and Yvan Castin. *Dynamic Instability of a Rotating Bose-Einstein Condensate*. Phys. Rev. Lett. **87**, 190402 (2001).

[159] Francesca Zambelli and Sandro Stringari. *Quantized Vortices and Collective Oscillations of a Trapped Bose-Einstein Condensate*. Phys. Rev. Lett. **81**, 1754 (1998).

[160] F. Chevy, K. W. Madison, and J. Dalibard. *Measurement of the Angular Momentum of a Rotating Bose-Einstein Condensate*. Phys. Rev. Lett. **85**, 2223 (2000).

[161] Francesco Ancilotto, Manuel Barranco, Martí Pi, and Luciano Reatto. *Vortex properties in the extended supersolid phase of dipolar Bose-Einstein condensates*. Phys. Rev. A **103**, 033314 (2021).

[162] T. Macri, F. Maucher, F. Cinti, and T. Pohl. *Elementary excitations of ultracold soft-core bosons across the superfluid-supersolid phase transition*. Phys. Rev. A **87**, 061602 (2013).

[163] Francesco Ancilotto, Maurizio Rossi, and Flavio Toigo. *Supersolid structure and excitation spectrum of soft-core bosons in three dimensions*. Phys. Rev. A **88**, 033618 (2013).

[164] Alessio Recati and Sandro Stringari. *Coherently Coupled Mixtures of Ultracold Atomic Gases*. Annual Review of Condensed Matter Physics **13**, 407 (2022).

[165] Giovanni Italo Martone. *Bose-Einstein condensates with Raman-induced spin-orbit coupling: An overview*. Europhysics Letters **143**, 25001 (2023).

[166] Natalia Masalaeva, Helmut Ritsch, and Farokh Mivehvar. *Tuning Photon-Mediated Interactions in a Multimode Cavity: From Supersolid to Insulating Droplets Hosting Phononic Excitations*. Phys. Rev. Lett. **131**, 173401 (2023).

[167] P. B. Blakie, L. Chomaz, D. Baillie, and F. Ferlaino. *Compressibility and speeds of sound across the superfluid-to-supersolid phase transition of an elongated dipolar gas*. Phys. Rev. Res. **5**, 033161 (2023).

[168] H.-Y. Lu, H. Lu, J.-N. Zhang, R.-Z. Qiu, H. Pu, and S. Yi. *Spatial density oscillations in trapped dipolar condensates*. Phys. Rev. A **82**, 023622 (2010).

[169] S. M. Roccuzzo, S. Stringari, and A. Recati. *Supersolid edge and bulk phases of a dipolar quantum gas in a box*. Phys. Rev. Res. **4**, 013086 (2022).

[170] M. Nilsson Tengstrand, D. Boholm, R. Sachdeva, J. Bengtsson, and S. M. Reimann. *Persistent currents in toroidal dipolar supersolids*. Phys. Rev. A **103**, 013313 (2021).

[171] Luigi Amico, Dana Anderson, Malcolm Boshier, Jean-Philippe Brantut, Leong-Chuan Kwek, Anna Minguzzi, and Wolf von Klitzing. *Colloquium: Atomtronic circuits: From many-body physics to quantum technologies*. Rev. Mod. Phys. **94**, 041001 (2022).

[172] Marija Šindik, Tomasz Zawiślak, Alessio Recati, and Sandro Stringari. *Sound, Superfluidity, and Layer Compressibility in a Ring Dipolar Supersolid*. Phys. Rev. Lett. **132**, 146001 (2024).

[173] A Kumar, N Anderson, W D Phillips, S Eckel, G K Campbell, and S Stringari. *Minimally destructive, Doppler measurement of a quantized flow in a ring-shaped Bose–Einstein condensate*. New Journal of Physics **18**, 025001 (2016).

[174] P. C. Martin, O. Parodi, and P. S. Pershan. *Unified Hydrodynamic Theory for Crystals, Liquid Crystals, and Normal Fluids*. Phys. Rev. A **6**, 2401 (1972).

[175] W. F. Vinen. *Physics of Quantum Fluids*. Tokyo summer lectures in theoretical and experimental physics. Edited by R. Kubo, and F. Takano. Syokabo Publishing Company, Tokyo (1971).

[176] H Hu, E Taylor, X-J Liu, S Stringari, and A Griffin. *Second sound and the density response function in uniform superfluid atomic gases*. New Journal of Physics **12**, 043040 (2010).

[177] J. Tao, M. Zhao, and I. B. Spielman. *Observation of Anisotropic Superfluid Density in an Artificial Crystal*. Phys. Rev. Lett. **131**, 163401 (2023).

[178] Hiroki Saito, Yuki Kawaguchi, and Masahito Ueda. *Ferrofluidity in a Two-Component Dipolar Bose-Einstein Condensate*. Phys. Rev. Lett. **102**, 230403 (2009).

[179] T. Bland, E. Poli, L. A. Peña Ardila, L. Santos, F. Ferlaino, and R. N. Bisset. *Alternating-domain supersolids in binary dipolar condensates*. Phys. Rev. A **106**, 053322 (2022).

[180] Shaoxiong Li, Uyen Ngoc Le, and Hiroki Saito. *Long-lifetime supersolid in a two-component dipolar Bose-Einstein condensate*. Phys. Rev. A **105**, L061302 (2022).

[181] D. Scheiermann, L. A. Peña Ardila, T. Bland, R. N. Bisset, and L. Santos. *Catalyzation of supersolidity in binary dipolar condensates*. Phys. Rev. A **107**, L021302 (2023).

[182] W. Kirkby, Au-Chen Lee, D. Baillie, T. Bland, F. Ferlaino, P. B. Blakie, and R. N. Bisset. *Excitations of a Binary Dipolar Supersolid*. Phys. Rev. Lett. **133**, 103401 (2024).

[183] Ronen Rapaport and Gang Chen. *Experimental methods and analysis of cold and dense dipolar exciton fluids*. Journal of Physics: Condensed Matter **19**, 295207 (2007).

[184] Monique Combescot, Roland Combescot, and François Dubin. *Bose–Einstein condensation and indirect excitons: a review*. Reports on Progress in Physics **80**, 066501 (2017).

[185] L. V. Butov, A. C. Gossard, and D. S. Chemla. *Macroscopically ordered state in an exciton system*. Nature **418**, 751 (2002).

[186] S. V. Andreev. *Fragmented-condensate solid of dipolar excitons*. Phys. Rev. B **95**, 184519 (2017).